Defence Research and Development Canada
Recherche et développement pour la défense Canada

DEFENCE R&D DÉFENSE

Bistatic Synthetic Aperture Radar

TIF – Report (Phase I)

Christoph H. Gierull

Defence R&D Canada – Ottawa
TECHNICAL REPORT
DRDC Ottawa TR 2004-190
November 2004

Canada

Bistatic Synthetic Aperture Radar

TIF – Report (Phase I)

Christoph H. Gierull

Defence R&D Canada – Ottawa

Technical Report

DRDC Ottawa TR 2004-190

November 2004

Abstract

This technical report presents theoretical and experimental results of phase I of the Technology Investment Fund (TIF) project on low probability of intercept, that is bistatic SAR. In bistatic SAR, the transmitter and receiver are spatially separated and hence, the risks of detection and localization are significantly reduced, i.e., its vulnerability to jamming is reduced and its survivability significantly increased. Bistatic SAR images include information that is complementary to monostatic images due to the different scattering mechanisms involved. Such information could lead to the development of new techniques for automatic target recognition and classification.

The project investigates the feasibility of bistatic SAR and identifies performance limits through a trade-off analysis between radar parameters/geometry and achievable resolution. As the main result, conclusions are drawn regarding the bistatic observation time and the subsequent imaging performance under different bistatic configurations, as well as the performance degradation due to severe oscillator phase noise or jitter. The report also includes a description of a bistatic SAR simulator, an implemented version of a time domain bistatic SAR processor, and the analysis of existing experimental bistatic clutter data sets.

Résumé

Le présent rapport technique donne les résultats théoriques et expérimentaux de la phase I d'un projet mené dans le cadre du Fonds d'investissement technologique (FIT) sur la faible probabilité d'interception (FPI), c'est-à-dire le radar à synthèse d'ouverture (RSO) bistatique. Dans le RSO bistatique, l'émetteur et le récepteur sont séparés spatialement, ce qui réduit significativement les risques de détection et de localisation, c'est-à-dire que la vulnérabilité du radar au brouillage est réduite et sa surviabilité, fortement accrue. Les images de RSO bistatique comportent de l'information qui vient compléter les images de radar monostatique en raison des différents mécanismes de diffusion en jeu. Cette information pourrait mener à la mise au point de nouvelles techniques de reconnaissance et de classification automatiques des cibles.

Le projet comporte une étude de faisabilité du RSO bistatique et en définit les limites de rendement par une analyse comparative entre les paramètres et la géométrie du radar, d'une part, et la résolution réalisable. Comme grand résultat, des conclusions sont tirées au sujet du temps d'observation du radar bistatique et l'obtention

subséquente d’images en fonction de différentes configurations de radar bistatique, ainsi qu’au sujet de la dégradation du rendement à cause de grave bruit de phase d’oscillateur ou gigue. Le rapport comprend aussi une description d’un simulateur de RSO bistatique, une version mise en æuvre d’un processeur de RSO bistatique temporel et l’analyse des séries de données disponibles de clutter de radar bistatique expérimental.

Executive summary

In military environments, imaging based on monostatic synthetic aperture radar (SAR) is, due to its active illumination of the scene, easily detected and thus highly vulnerable to electronic counter measures or even destruction. Use of a bistatic (or multi-static) system, with its transmitter spatially separated from the 'silent' receiving systems significantly reduces the risk of receiver detection and increases survivability. In addition to low probability of intercept (LPI), such a bistatic SAR configuration offers additional surveillance capabilities, such as complementary imagery due to forward-scattering measurements. The proposed concept opens a wide field of future, related research and will even lead to different applications, like bistatic SAR in combination with ground moving target indication or topographic mapping. Even forward looking SAR becomes possible with bistatic configurations (impossible with monostatic systems) which might be exploited in landing aids for aircraft or obstruction warning devices in helicopters. This work could also serve as foundation of R&D in the field of covert radar detection and passive imaging, which also exploits bistatic geometry but uses a non-cooperative illuminator of opportunity.

The purpose of this Technology Investment Fund (TIF) project is to investigate the feasibility and the limitations of a bistatic SAR system. This includes theoretical study and simulation of optimum bistatic SAR configurations, the development of robust processing algorithms for imaging, and an experimental demonstration with the upgraded airborne SpotSAR system and a specially constructed stationary receiver.

This report presents a theoretical framework for performance analysis prediction for any bistatic geometry with respect to the geometric and radiometric ground resolution. It introduces analysis of the most promising configurations, including their performance limits and relevant problems, as well as the development and implementation of a bistatic SAR simulator, which will be used to confirm the analysis and to test bistatic SAR processors. Finally, the report describes the successful coherent processing of two existing bistatic clutter data sets (space-borne and airborne data) measured at the Air Force Research Laboratories (AFRL) in Rome, NY in 2002.

This research provides a deep level of understanding of the capabilities and difficulties associated with bi- and multistatic SAR concepts. This knowledge will, for instance, be essential to perform system design studies and accurate cost/performance trade-off analyses of SBR designs in combination with airborne systems for future military SAR applications. The application of such concepts could significantly enhance Canada's surveillance capabilities in times of conflict by reducing vulnerability to receiver jamming and to direct attack of the surveillance asset.

Presently, Canada is in the favourable situation of being able to collect data from national assets including both space-borne sensors, RADARSAT-1 and soon RADARSAT-2, and experimental airborne SAR systems, such as DRDC's SpotSAR or Environment Canada's C-band SAR. This rather unique position offers the opportunity to test sophisticated new radar concepts using measured data gathered under realistic military conditions.

Christoph H. Gierull; 2004; Bistatic Synthetic Aperture Radar; DRDC Ottawa TR 2004-190; Defence R&D Canada – Ottawa.

Sommaire

Dans les milieux militaires, l'imagerie fondée sur le radar à synthèse d'ouverture (RSO) monostatique est, en raison de l'illumination active de la scène, facilement détectée et, par conséquent, hautement vulnérable aux contre-mesures électroniques ou même à la destruction. L'utilisation d'un système bistatique (ou multistatique), dont l'émetteur est spatialement séparé des systèmes de réception 'silencieux', réduit significativement le risque de détection du récepteur et accroît la surviabilité. Outre la faible probabilité d'interception (FPI), une telle configuration de RSO bistatique offre des capacités additionnelles de surveillance, comme l'imagerie complémentaire grâce à des mesures de prodiffusion. Le concept proposé ouvre un vaste domaine de recherches connexes et mènera même à différentes applications, comme l'utilisation du RSO bistatique en conjonction avec la cartographie topographique ou l'indication de cibles mobiles au sol. Même le RSO à visualisation vers l'avant devient possible avec les configurations de radar bistatique (impossible avec les systèmes monostatiques), et il pourrait être exploité comme aide à l'atterrissage pour les dispositifs de détection d'obstacle ou d'aéronef à bord d'hélicoptères. Ce travail pourrait aussi servir de fondement à la recherche et développement dans le domaine de la détection radar discrète et de l'imagerie passive, qui exploite aussi la géométrie bistatique, mais qui utilise un illuminateur de choix non coopératif.

Le but du présent projet mené dans le cadre du Fonds d'investissement technologique (FIT) est l'étude de la faisabilité et des limites d'un système RSO bistatique, y compris la simulation et l'étude théorique de configurations optimales de RSO bistatique, la mise au point de solides algorithmes de traitement d'imagerie et une démonstration expérimentale au moyen du système SpotSAR aéroporté amélioré et d'un récepteur stationnaire particulier.

Le présent rapport donne un cadre théorique de prédication d'analyse du rendement de n'importe quelle géométrie bistatique en ce qui concerne la résolution au sol géométrique et radiométrique. Il introduit l'analyse des configurations les plus prometteuses, y compris leurs limites de rendement et les problèmes pertinents, ainsi que le développement et la mise en place d'un simulateur de RSO bistatique, qui servira à confirmer l'analyse et à mettre à l'essai les processeurs de RSO bistatique. Enfin, le rapport décrit le traitement cohérent réussi de deux séries disponibles de données de clutter bistatique (données spatiales et de vol) prises à l'Air Force Research Laboratory (AFRL) à Rome (N.Y.) en 2002.

Cette recherche permet d'obtenir une compréhension en profondeur des capacités et des difficultés associées aux concepts du ROS bistatique et multistatique. Ces connaissances sont, par exemple, essentielles à la conduite d'études de conception de systèmes et d'analyses comparatives cots/rendement précises des conceptions

du radar satellisé (RS) en conjonction avec les systèmes aéroportés en vue d'applications militaires futures du RSO. L'application de ces concepts pourrait améliorer significativement les capacités de surveillance du Canada en périodes de conflit, en réduisant la vulnérabilité au brouillage des récepteurs et aux attaques directes des dispositifs de surveillance.

Le Canada se trouve actuellement dans une situation favorable, étant en mesure de recueillir des données à partir de dispositifs nationaux, y compris les deux capteurs spatiaux (RADARSAT-1 et bientt RADARSAT-2) et des systèmes spatiaux expérimentaux (comme SporSAR de RDDC ou le RSO en bande C d'Environnement Canada). Cette position plutt unique offre la possibilité de mettre à l'essai de nouveaux concepts perfectionnés dans le domaine du radar à l'aide de données mesurées recueillies dans des conditions militaires réalistes.

Christoph H. Gierull; 2004; Radar à synthèse d'ouverture bistatique; DRDC Ottawa TR 2004-190; R & D pour la défense Canada – Ottawa.

Table of contents

List of figures

List of tables

Acknowledgements

The author would like to cordially thank Turkish naval Lieutenant Nilüfen Çotuk, who was working at DRDC Ottawa for an extended period under the Canadian Defence Research Fellowship program, for his assistance in programming the bistatic space-based SAR simulator and developing the time domain SAR processor. I am also very thankful for his support during flight trials and the stripping of the experimental data.

Further, I would like to express my gratitude to Canadian liaison officer Capt. Mark Aubrey and our American colleagues at AFRL in Rome, NY for their excellent work during the numerous TTRDP trials and their support in providing the bistatic clutter data sets.

1 Introduction

In military environments, monostatic synthetic aperture radar (SAR) is, due to its active illumination of the scene, easily detected and thus highly vulnerable to electronic counter measures or even destruction. Use of a bistatic/multi-static system, with its transmitter spatially separated from the 'silent' receiving systems significantly reduces the risk of receiver detection and increases survivability. Potentially qualified candidates for the transmitter are space based radars (SBR) or aircrafts flying at high altitudes. The receivers can be mounted on highly maneuverable aircraft or UAVs that may image the scene at different times and from different angles. In addition to low probability of detection, such a bistatic/multistatic SAR configuration offers additional surveillance capabilities, such as complementary imagery due to forward-scattering measurements. This may lead to the development of new techniques for automatic target recognition and classification and could enhance the visibility of stealthy targets. Furthermore, improved ground moving target indication (GMTI) and topographical surveying and mapping of the scene become possible.

Recently, there has been a growing interest in the use of space-based radars (SBR) to support the future military requirements of Canada and its allies. These requirements include 24/7 wide-area surveillance of land targets under all weather conditions. Consequently, future military SBR systems will be equipped with synthetic aperture radar. Wide area coverage from space by SAR requires resolution to be traded off with swath coverage. It is further limited by the antenna power handling capacity, limited down-link capacity, lower SNR (due to larger distances between sensor and targets) and a less flexible imaging geometry compared to airborne SAR systems. On the other hand, airborne SAR is highly vulnerable because, as an active system, its transmitted energy can be detected and hence intercepted, particularly when operating in a hostile environment. Interception includes active receiver jamming as well as the actual destruction of the radar platform.

This vulnerability may be overcome during a conflict by using a bistatic 'low probability of intercept' SAR concept, where the radar transmitter may be located on a satellite, while the receiver is located on an airborne platform, such as a UAV. Since the receiving radar system operates in a passive ('silent') mode, the risk of receiver detection and localization is significantly reduced, i.e., its vulnerability to jamming is reduced and its survivability significantly increased. Compared to monostatic space-based SAR, a higher SNR of the scattered echoes can also be achieved because of the smaller distances between the targets and the receiver. Furthermore, complementary information in the SAR images can be expected due to the forward-scattering measurements of bistatic systems. For instance, the roofs of buildings might be the major source of scattering in bistatic SAR imagery com-

pared to the walls in conventional, monostatic SAR images. Combined with the advantages of a more flexible imaging geometry, it can be seen how such a bistatic SAR concept can enhance surveillance capabilities such as ground moving target indication (GMTI) and topographical surveying and mapping.

In contrast to conventional, monostatic SAR, the required bistatic configuration has a far more complex geometry that leads to certain unique problems that must be dealt with during image formation. Examples of such problems include greater variation of Doppler frequency with range, non-linear Doppler frequency modulation in the along-track direction, reception of transmitter antenna mainlobe energy through receiver antenna sidelobes, and fold-over effects resulting from range ambiguities. In order to generate high-resolution SAR images, the bistatic imaging geometry must be known very accurately. This makes great demands on both the motion measurement system/equipment, such as INS and GPS, and the SAR signal processing/autofocus algorithms. Furthermore, the echo pulses must be coherently measured, i.e., the phase information of the transmitted pulse has to be preserved. Hence, the problem of time synchronization between the two systems must be resolved because the transmitter and receiver are spatially separated.

Although the investigation and application of bistatic radar is by no means new [1, 2, 3, 4], there appears to be a resurgence caused by technological progress and military exigency, particularly for imaging radars. Based on a growing confidence of technological feasibility, economical affordability, and due to palpable advantages of bistatic SAR for military applications worldwide, scientific activities have intensified recently. Until two years ago only a handful of papers were published in the open literature. At the international conference on Geoscience and Remote SenSing (IGARSS'03), several papers about bistatic SAR appeared. One year later, at the European SAR Conference EUSAR'04, there were two full sessions dedicated to phenomenology and processing of bistatic and multistatic SAR data. While the interest in bistatic SAR was in the past mostly stamped by military advantages, even civil applications are starting to be discussed [5, 6]. Furthermore, highly sophisticated bi- and multistatic space-borne system concepts are being investigated for enhanced applications such as interferometry [7, 8, 9] and SAR/MTI [10, 11, 12]. A step even further ahead is the possibility of passive (or parasitic) SAR imaging, which also exploits a bistatic geometry but using a non-cooperative illuminator of opportunity [13, 14, 15].

However, a thorough and complete theoretical performance analysis with regard to the maximal geometric resolution determined by the three-dimensional flight geometry and the maximum observation time is noticeably absent from the bistatic SAR literature. Further, due to lack of necessity in monostatic SAR (with only one local oscillator (LO) for up- and down conversion of the signals) the radiometric deterioration caused by the severe phase noise of two separate LOs has not been

extensively investigated in the past.

This TIF-project is divided into two phases. In Phase I, the theoretical background of bistatic SAR has been derived via stepwise mathematical modeling of the received echo signals. Simultaneously, a simulation tool and bistatic SAR processing algorithms are developed to evaluate and demonstrate the performance of the new SAR processing concepts. A detailed investigation of bistatic SAR performance, like achievable geometric and radiometric resolution, has been performed over a wide range of bistatic geometries and radar operating parameters. In Phase II of the project, deeper insight into the functionality of a bistatic SAR system and the physical properties of its SAR imagery will be gained with experimental measurements conducted by DRDC Ottawa's airborne SpotSAR radar system.

2 Bistatic SAR signal model

In this Section a bistatic SAR signal model is derived as well as the predicted SAR processing degradation due to oscillator frequency mismatch between the two separated transmit and receive local oscillators. The output signal from two ideally non-drifting oscillators would be a pure sine wave of exactly identical frequency, but any real device, even the most stable, is disturbed by unavoidable processes such as random noise and drifts due to aging and/or environmental effects.

The starting point for the analysis of bistatic SAR is the three-dimensional geometry depicted in Fig. 1. While it was sufficient for investigation of bistatic radar in the past to only consider two-dimensional geometries, analysis of bistatic SAR requires a three-dimensional geometry, e.g., [16, 17]. As a convention in the remainder of this document, vector quantities are underlined and matrices are written in bold. The transpose operator is denoted as superscript ’, complex conjugate as * and complex conjugate transpose as the Hermitian operator †.

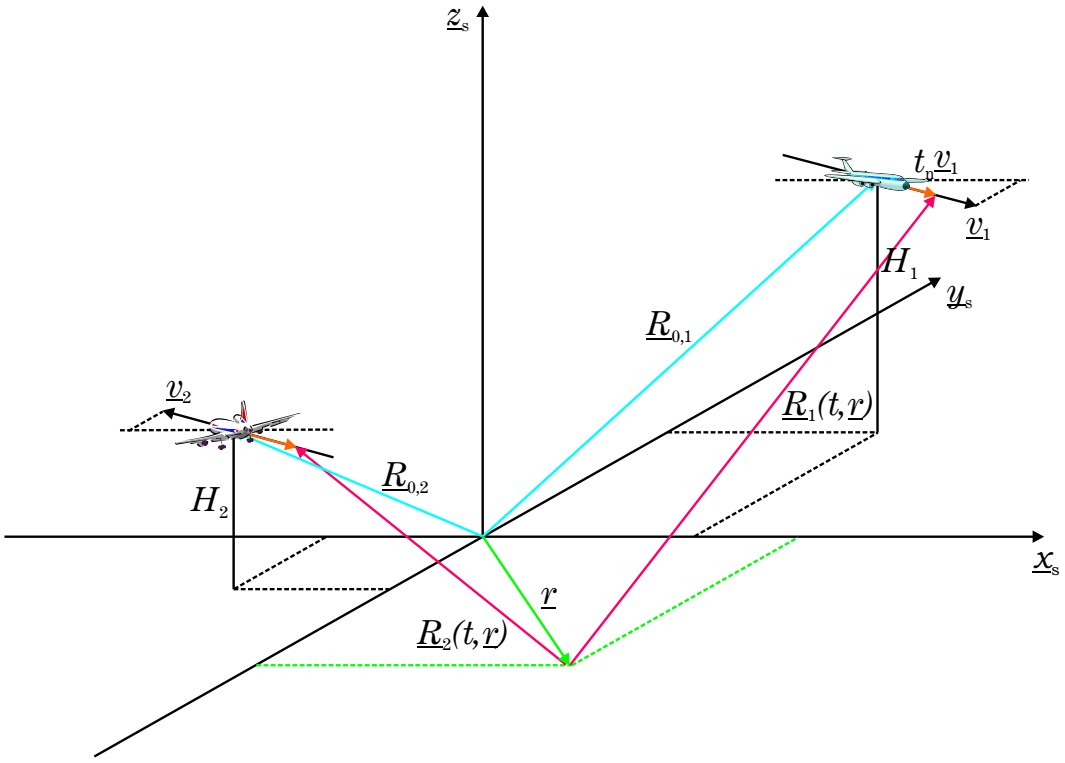

Figure 1 : *Bistatic SAR geometry with constant velocity of each platform.*

Consider two independent, spatially separated, radar platforms moving along straight

paths in the three-dimensional Cartesian scene co-ordinate system, which is denoted by subscript s, appendix D.1. The two platforms are not necessarily required to be aircrafts. For example, using a satellite as illuminator is a particularly interesting configuration, as will be shown later.

A detailed definition and description of all involved co-ordinate systems is given in appendix D. The center (origin) of the scene is defined as the intersection of the transmitter and receiver pointing vectors with the ground plane at time $t = 0$. We are assuming that both platforms are flying in a plane parallel to the ground plane, i.e., with constant altitudes H_i and with constant velocities $\underline{v}_i$ for $i = 1, 2$. These assumptions are not restrictive and are only made to clarify the following derivations.

The range vector from the transmitter (henceforth denotes by subscript 1) to a point $\underline{r}$ on the ground at time t is given as

$$\underline{R}_1(t, \underline{r}) = \left(\underline{R}_{0,1} - \underline{r}\right) + \underline{v}_1 t, \tag{1}$$

where $\underline{R}_{0,1} = \underline{R}_1(0, \underline{0})$ is the vector from the scene center to the transmitter at time zero, see appendix F. This vector is commonly determined by the depression angle in elevation and the squint angle in azimuth at the time origin, see appendix A. Analogously, the range vector for the receiver is denoted by subscript 2. Note that the subscripts 1,2 are used rather than, e.g., 't,r' to indicate the complete interchangeability of receiver and transmitter, from a physical model point-of-view.

2.1 Constant oscillator frequency offset

2.1.1 Time history

At subsequent instances in time, denoted by $t_n = n\Delta T$ for $n = 0, 1, 2, \ldots$, the transmitter coherently radiates a linear frequency modulated (LFM) pulse with carrier frequency ω_1 of form $\mathrm{Re}\{s_{\mathrm{trans}}(t)\}$ with

$$s_{\mathrm{trans}}(t) = \sum_{n=0}^{\infty} e^{j\pi\frac{B}{T}(t-t_n)^2} e^{j(\omega_1 t + \phi_1(0) + \xi_1(t))} \,\mathrm{rect}\left(\frac{t-t_n}{T}\right) + n_1(t), \tag{2}$$

where B is the chirp bandwidth, T is the pulse duration, and ΔT is the pulse repetition interval (PRI). The term $n_1(t)$ represents unavoidable additive noise, e.g., the thermal sensor noise in the transmitter hardware. It is usually modeled as a stationary complex normal distributed stochastic process, i.e., a Gaussian process with expectation zero and auto-covariance function $c_{n_1 n_1}(t)$. However, since we are at this point interested in phase noise effects, the additive noise term is omitted in the following for didactical clarity. The stochastic process $\xi_1(t)$ denotes the 'multiplicative' phase noise, i.e., describes oscillator phase instabilities such as jitter. The

constant initial phase $\phi_1(0)$, at time origin, does not effect the SAR performance and can be set to zero.

It is sufficient for the range processing to concentrate on one particular pulse so that the summation in (2) will be abandoned henceforth for notational simplicity. The signal is reflected from a scatterer at ground location $\underline{r}$ and impinges on the receiver with a corresponding time delay τ:

$$s_{\text{ref}}(t) = e^{j\pi\frac{B}{T}(t-t_n-\tau)^2} e^{j\omega_1(t-\tau)} \,\text{rect}\left(\frac{t-t_n-\tau}{T}\right), \tag{3}$$

where the phase noise is ignored at the moment. It is important to note that, although the time delay τ is strictly speaking itself time dependent, it can be treated as constant over the duration of a pulse T (i.e., $\tau \equiv \tau(t_n)$) but, of course, will vary slowly from pulse-to-pulse[1].

The down-conversion of this RF signal to baseband with receiver oscillator frequency ω_2 can be expressed by multiplication with $\exp(-j\omega_2 t)$ and yields the received signal

$$s_{\text{rec}}(t) = e^{-j\omega_1\tau}\, e^{j\pi\frac{B}{T}(t-t_n-\tau)^2}\, e^{j\Delta\omega t} \,\text{rect}\left(\frac{t-t_n-\tau}{T}\right), \tag{4}$$

where $\Delta\omega = \omega_1 - \omega_2$ denotes the constant frequency offset between the two independent oscillators. Note that a constant frequency offset means a linear phase drift. The time history of the time-shifted and phase-rotated received pulses is depicted in Fig. 2.

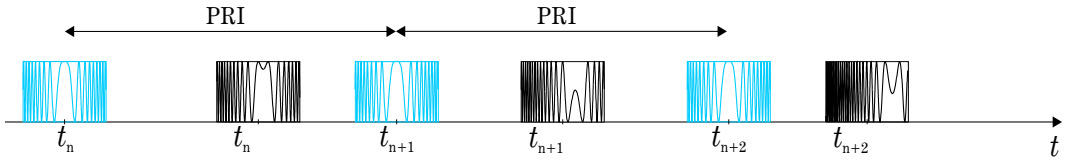

Figure 2 : *Illustration of the phase and time shifts of the received pulses.*

2.1.2 Fast-time (range) processing

The range-compression is performed by convolution with filter function $h(t)$, which, when chosen to be the time-inverted conjugate of the demodulated transmit signal

$$h(t) = \exp\left(-j\pi\frac{B}{T}t^2\right) \,\text{rect}\left(\frac{t}{T}\right), \tag{5}$$

[1]This may be exploited to achieve high resolution in the along-track or Doppler direction.

maximizes the signal-to-noise ratio (SNR). The matched filter output or impulse response function is given as

$$\begin{aligned} p(t) &= (s_{\rm rec} \star h)(t) = \int_{-\infty}^{\infty} s_{\rm rec}(t')h(t-t')dt' = \int_{-\infty}^{\infty} s_{\rm rec}(t-t')h(t')dt' \\ &= e^{-j\omega_1\tau} \int_{-\infty}^{\infty} e^{j\pi\frac{B}{T}(t-t'-t_n-\tau)^2} e^{j\Delta\omega(t-t')} \\ &\qquad \cdot e^{-j\pi\frac{B}{T}t'^2} \,\mathrm{rect}\left(\frac{t-t'-t_n-\tau}{T}\right) \mathrm{rect}\left(\frac{t'}{T}\right) dt'. \end{aligned} \tag{6}$$

The two rectangular functions within the integrand of (6) restrict the integration interval to the time-dependent values $a(t)$ and $b(t)$ (to be specified), that is:

$$\begin{aligned} p(t) &= e^{-j\omega_1\tau} e^{j\Delta\omega t} \int_{a(t)}^{b(t)} e^{j\pi\frac{B}{T}\left((t-t_n-\tau)^2-2(t-t_n-\tau)t'\right)} e^{-j\Delta\omega t'} dt' \\ &= e^{-j\omega_1\tau} e^{j\Delta\omega t} e^{j\pi\frac{B}{T}(t-t_n-\tau)^2} \int_{a(t)}^{b(t)} e^{-j\left(2\pi\frac{B}{T}(t-t_n-\tau)+\Delta\omega\right)t'} dt' \\ &= e^{-j\omega_1\tau} e^{j\Delta\omega t} e^{j\pi\frac{B}{T}(t-t_n-\tau)^2} e^{-j\left(2\pi\frac{B}{T}(t-t_n-\tau)+\Delta\omega\right)\frac{b(t)+a(t)}{2}} \\ &\qquad \cdot 2\big(b(t)-a(t)\big) \,\mathrm{sinc}\left(\big(2\pi\frac{B}{T}(t-t_n-\tau)+\Delta\omega\big)\frac{b(t)-a(t)}{2}\right). \end{aligned} \tag{7}$$

The definition of the integration interval is illustrated in Fig. 3.

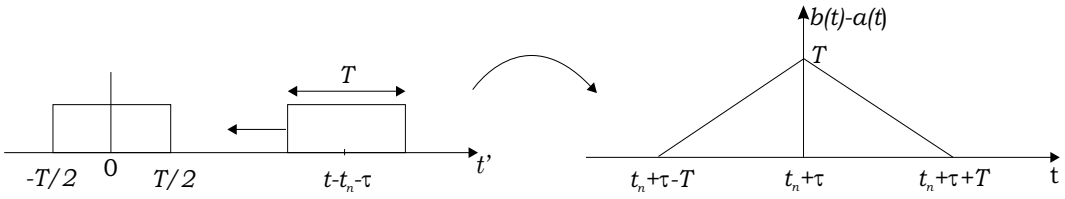

Figure 3 : *Illustration of integration interval for range-compression.*

The integration interval $b(t) - a(t)$ is non-zero when the right rectangle starts to touch the left one at time $t = t_n + \tau + T$, is maximum when they are completely overlap at $t = t_n + \tau$, and linearly decreases until $t = t_n + \tau - T$. The triangular time history can be expressed analytically as

$$b(t) - a(t) = \big(T - |t - t_n - \tau|\big) \,\mathrm{rect}\left(\frac{t-t_n-\tau}{2T}\right). \tag{8}$$

The sum of the two limits can be expressed as

$$b(t) + a(t) = (t - t_n - \tau)\,\mathrm{rect}\left(\frac{t - t_n - \tau}{2T}\right). \tag{9}$$

From (8) it is clear that within the vicinity of the reflected pulses $t = t_n + \tau$ the integration region can be approximated by the constant pulse length T, as commonly done in the literature:

$$p(t) \cong 2Te^{-j\omega_1\tau}e^{j\Delta\omega t}e^{j\pi\frac{B}{T}(t-t_n-\tau)^2}\,\mathrm{sinc}\left(\big(2\pi\frac{B}{T}(t - t_n - \tau) + \Delta\omega\big)\frac{T}{2}\right). \tag{10}$$

The effect of an oscillator frequency mismatch becomes apparent, namely the position of the peak is displaced from the correct location. Setting the argument of the sinc-function in (10) to zero yields

$$t_0 = t_n + \tau - \frac{T\Delta f}{B} \quad \text{or} \quad B(t_0 - t_n - \tau) = T\Delta f, \tag{11}$$

where $\Delta f = \Delta\omega/2\pi = f_1 - f_2$. As the range resolution is determined by the inverse of the pulse bandwidth ($\tau_0 = 1/B$), the value of $B(t_0 - t_n - \tau) = B\Delta\tau$ represents the range displacement in multiples of the resolution cell size.

2.1.3 Slow-time (Doppler) processing

For the subsequent Doppler processing of a target at ground location $\underline{r}$, the pulse-to-pulse time history is analysed along the corresponding time instances $t_n + \tau(t_n, \underline{r})$. Selecting the values of the impulse response function (10) at these times yields the phase signal

$$\begin{aligned} s_D(t_n, \underline{r}) &= \exp\big(-j\omega_1\tau(t_n, \underline{r})\big)\exp\big(j\Delta\omega(t_n + \tau(t_n, \underline{r}))\big) \\ &= \exp\big(-j(\omega_1 - \Delta\omega)\tau(t_n, \underline{r})\big)\exp\big(j\Delta\omega t_n\big), \end{aligned} \tag{12}$$

where the magnitude has been omitted for simplicity. The first exponential term shows an effective carrier frequency shift for the transmitter. However, this shift is negligible because reasonable offsets will only be a small fraction of the center frequency $|\Delta\omega/\omega_1| \ll 1$. In contrast, the second phase term cannot be neglected and will affect the Doppler processing.

By omitting the offset, i.e. $\Delta\omega = 0$, the first exponential term in (12) represents the common phase (Doppler) history caused by the changing distance (time delay) between transmitter, target and receiver over many pulses

$$\exp\big(-j\omega_1\tau(t_n, \underline{r})\big) = \exp\big(-jk_1(||\underline{R}_1(t_n, \underline{r})|| + ||\underline{R}_2(t_n, \underline{r})||)\big), \tag{13}$$

where $k_1 = 2\pi f_1/c$ denotes the transmitted wavenumber. To get deeper insight, it is sufficient now to consider a quasi-monostatic geometry with an approximate quadratic range-time history. It will be shown later that such scenarios comprise bistatic flight geometries with parallel paths of both platforms as well as either a stationary transmitter or receiver. For a conventional monostatic SAR with identical distances, equation (13) yields the classic Doppler phase history (second order Taylor series):

$$\phi(t,\underline{r}) = 2k_1||\underline{R}(t,\underline{r})|| \cong 2k_1\left(R_b(\underline{r}) + \frac{v_a^2}{2R_b(\underline{r})}(t-t_b)^2\right), \tag{14}$$

where, for notational simplicity, the slow-time t_n has been replaced by t and k_1 by k. This convention will be used henceforth when possible without confusion. The time where the platform is broadside to the scatterer located at $\underline{r}$ is denoted by t_b and the distance between them (at this instant in time) by R_b. For non-squinted SAR geometries and stationary reflectors, the time t_b coincides with the point of closest approach [18].

Inserting (14) into (12) yields the slow-time or Doppler signal that can be written as

$$\begin{aligned} s_{\mathrm{D}}(t,\underline{r}) &= \exp\left(-j2k\left(R_b(\underline{r}) - \frac{\Delta\omega}{2k}t_b\right)\right) \\ &\quad \cdot \exp\left(j2k\left(\frac{\Delta\omega}{2k}(t-t_b) - \frac{v_a^2}{2R_b(\underline{r})}(t-t_b)^2\right)\right), \end{aligned} \tag{15}$$

where constant terms will be omitted from here onwards. The linear coefficient is tantamount to a quasi radial velocity $v_r = \Delta\omega/(2k)$. Analogously to the range-compression, the Doppler signal is convolved with the expected signal of a reflector at location $t_b = 0$ (reference function):

$$p_{\mathrm{D}}(t,\underline{r}) = (s_{\mathrm{D}} \star s_{\mathrm{ref}})(t) = \int_{-\infty}^{\infty} s_{\mathrm{D}}(t-t')s_{\mathrm{ref}}(t')\,dt', \tag{16}$$

where

$$s_{\mathrm{ref}}(t,\underline{r}) = \exp\left(j2k\frac{v_a^2}{2R_b(\underline{r})}t^2\right)\ \mathrm{rect}\left(\frac{t}{T_s}\right), \tag{17}$$

where T_s denotes the synthetic aperture time over which the particular reflector is observed by the radar. The maximum duration that the reflector is in the antenna beamwidth is usually expressed by the antenna beamwidth $\theta_{3\mathrm{dB}}$ and the slant range distance $T_s = \theta_{3\mathrm{dB}}R_b(\underline{r})/v_a$. Using this value, the point spread function reads

$$p_{\mathrm{D}}(t,\underline{r}) = e^{j2k\left(\frac{\Delta\omega}{2k}t - \frac{v_a^2}{2R_b(\underline{r})}(t-t_b)^2\right)} \int_{-T_s/2}^{T_s/2} e^{-j2k\left(\frac{\Delta\omega}{2k} - \frac{v_a^2}{R_b(\underline{r})}(t-t_b)\right)t'}\,dt'$$

$$= \quad 2T_s e^{j2k\left(\frac{\Delta\omega}{2k}t - \frac{v_a^2}{2R_b(\underline{r})}(t-t_b)^2\right)} \operatorname{sinc}\left(k\left(\frac{\Delta\omega}{2k} - \frac{v_a^2}{R_b(\underline{r})}(t-t_b)\right)T_s\right). \tag{18}$$

Again, the peak is displaced by $\Delta t_b = (t_b' - t_b)$, where t_b' is computed by setting the argument of the sinc-function to zero

$$t_b' = t_b + \frac{\Delta\omega R_b(\underline{r})}{k v_a^2} \quad \text{or} \quad \Delta t_b = (t_b' - t_b) = \frac{\lambda R_b(\underline{r})}{v_a^2}\Delta f. \tag{19}$$

The displacement in meters is given by $v_a \Delta t_b$. Normalizing this value to the well known optimum azimuth or Doppler resolution $A/2$, where $A \cong \lambda/\theta_{3\text{dB}}$ denotes the real aperture of the radar, yields the displacement in resolution cells

$$\frac{v_a(t_b' - t_b)}{\lambda/(2\theta_{3\text{dB}})} = \frac{2\theta_{3\text{dB}} R_b(\underline{r})\Delta f}{v_a} = 2T_s\Delta f. \tag{20}$$

Bearing in mind that the synthetic aperture time is much larger than the pulse duration T, the displacement is seen to be much more severe in the Doppler-direction (cf. (11)).

Fig. 4 illustrates the different displacements for range and Doppler-direction as well as for typical airborne and spaceborne parameters. The pulse duration for either case was assumed to be $T = 50$ μs. From the solid curve in Fig. 4, a target becomes shifted by exactly one range cell for a frequency mismatch of $\Delta f = 20$ KHz. Therefore the range displacement will only be significant for a rather large discrepancy of the two local oscillator frequencies. In contrast, the corresponding displacement in Doppler direction will be on the order of $10,000$ to one million pixels for this frequency offset.

If, for instance, a maximum shift of only one pixel is required, the disagreement between the oscillator frequencies must be smaller than 0.1 Hz, which is highly unrealistic. However, it is important to note that no de-focussing in either direction occurs due to a constant frequency offset, see also [19].

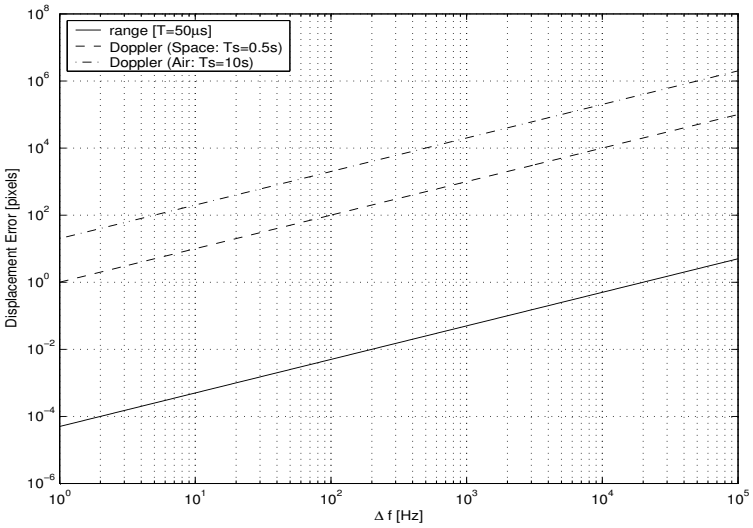

Figure 4 : *Expected displacement after range and Doppler compression along oscillator frequency offset, range displacement in pixels for $T = 50\ \mu$s (solid), Doppler displacement for $T_s = 0.5$ s (dashed) and Doppler displacement for $T_s = 10$ s (dash-dotted).*

2.2 Linear oscillator frequency drift

In addition to a constant frequency offset, in practise real oscillators drift slowly away from their nominal center frequency, for instance, caused by environmental changes, such as temperature, pressure or magnetic fields. Modern oscillators commonly compensate for such drifts by temperature compensation. A Temperature Compensated Crystal Oscillator (TCXO) typically contains a temperature compensation network to sense the ambient temperature and pull the crystal frequency to prevent frequency drift over the temperature range. An Oven Controlled Crystal Oscillator (OCXO) usually contains an oven block (with temperature sensor, heating element, oven circuitry, and insulation) to maintain a stable temperature. OCXOs offer a great improvement in frequency stability compared to simple TCXOs. Although, these techniques usually greatly improve the performance, residual drifts can still cause errors, particularly in radar applications. In space-based across-track interferometry, for instance, very long orbital segments are usually analysed in order to generate digital elevation models of entire continents. Even the smallest clock drifts lead to measurable and compromising phase artifacts [9, 20].

The aim of this section is to investigate how frequency drift influences the performance of a bistatic SAR, particularly since the two oscillators are spatially separated. The carrier frequencies are assumed to drift linearly away from their nominal value by

$$\omega_1(t) = \omega_1 + a_1 t \quad \text{and} \quad \omega_2(t) = \omega_2 + a_2 t, \tag{21}$$

where the a_i denote the change of rate of frequency or drift rates; the physical unit is rad/s. A linear frequency drift corresponds to a quadratic phase deviation.

The quality of oscillators is commonly specified by a dimensionless relative stability quantity $\epsilon = \Delta f/f$, e.g., $\epsilon = 1 \cdot 10^{-8}$ means a frequency deviation of 100 Hz for a 10 GHz X-band oscillator. Typical drift rates are 10 to 100 Hz/s for TCXOs, 0.1 to 1 Hz/s for higher quality OCXOs, and smaller than 0.1 Hz/s for the highest quality oscillators [21].

2.2.1 Fast-time (range) processing

In order to study the influence of drift individually, the constant oscillator frequency offset is set to $\Delta\omega = 0$, which means that the two oscillators may be perfectly synchronized at one point in time, and then are 'free-running' afterwards.

Generalizing the received (and into baseband down-converted) signal in (4) to time-dependent oscillator frequency:

$$s_{\mathrm{rec}}(t) = e^{-j\omega_2(t)\cdot t}\, e^{j\pi\frac{B}{T}(t-t_n-\tau)^2}\, e^{j\omega_1(t-\tau)\cdot(t-\tau)}\, \mathrm{rect}\left(\frac{t-t_n-\tau}{T}\right), \qquad (22)$$

inserting (21) into (22) and applying the filter function (5), leads to a matched filter response (analogous to (6))

$$p(t) = e^{-j\omega_1\tau} \int_{-T/2}^{T/2} e^{j\pi\frac{B}{T}(t-t'-t_n-\tau)^2} e^{ja_1(t-t'-\tau)^2} e^{-ja_2(t-t')^2} e^{-j\pi\frac{B}{T}t'^2}\, dt', \qquad (23)$$

where the integration limits are restricted to one-half of the pulse duration, as in (10). Re-writing (23) yields

$$\begin{aligned} p(t) &= e^{-j\omega_1\tau} e^{j\pi\frac{B}{T}(t-t_n-\tau)^2} e^{ja_1(t-\tau)^2} e^{-ja_2t^2} \\ &\quad \cdot \int_{-T/2}^{T/2} e^{-2j\left(\pi\frac{B}{T}(t-t_n-\tau)+\Delta at-a_1\tau\right)t'} e^{j\Delta at'^2}\, dt'. \end{aligned} \qquad (24)$$

Since the second order phase deviation is virtually always smaller than $\pi/2$ over the pulse duration, i.e., $(a_1 - a_2)T^2 = \Delta aT^2 \ll \pi/2$, the term $\exp(j\Delta at'^2)$ can be omitted in (24) and we get

$$\begin{aligned} p(t) &= e^{-j\omega_1\tau} e^{j\pi\frac{B}{T}(t-t_n-\tau)^2} e^{ja_1(t-\tau)^2} e^{-ja_2t^2} \\ &\quad \cdot \mathrm{sinc}\left(\left(\pi\frac{B}{T}(t-t_n-\tau)+\Delta at-a_1\tau\right)T\right). \end{aligned} \qquad (25)$$

Assuming no range-ambiguities, the round trip delay τ is restricted to lie within the pulse repetition interval $\tau < \mathrm{PRI} = 1/\mathrm{PRF}$ and the third summand in the argument of the sinc-function can be omitted. The peak of the sinc-function occurs at time

$$t_0' = \frac{\pi B(t_n + \tau)}{\pi B + \Delta a T}, \tag{26}$$

which is different from the error-free value $t_0 = t_n + \tau$ by

$$\Delta t_0 = t_0' - t_0 = -\frac{\Delta a T(t_n + \tau)}{\pi B + \Delta a T} \cong -\frac{\Delta a T}{\pi B} t_n \tag{27}$$

for large n. In other words, the peak position of the matched filter response in the range direction drifts very slowly away from the correct location over time. However, this effect will only become significant for unreasonably long time periods. For instance, it would take more than one hour to drift one range cell ($B\Delta t_0 = 1$) when using TCXOs, and about 100 hours when using OCXOs.

2.2.2 Slow-time (Doppler) processing

By omitting the drift ($\Delta t_0 = 0$) in (27), i.e., by sampling the signal (25) at slow-times $t_n + \tau$ yields the Doppler history

$$s_{\mathrm{D}}(t_n) = e^{-j\omega_1\tau} e^{ja_1 t_n^2} e^{-ja_2(t_n+\tau)^2} \cong e^{-j\omega_1\tau} e^{j\Delta a t_n^2} e^{-j2a_2 t_n \tau}, \tag{28}$$

where $a_2\tau^2$ is negligibly small. Re-writing the time delay τ in (13) and (14) to

$$\tau = \frac{2}{c}\left(R_b + \frac{v_a^2}{2R_b} t_b^2\right) - \frac{2v_a^2}{cR_b} t_b t + \frac{v_a^2}{cR_b} t^2 \equiv s_0 + s_1 t + s_2 t^2, \tag{29}$$

the Doppler signal in (28) becomes

$$s_{\mathrm{D}}(t) = e^{-j(\omega_1 s_1 + 2a_2 s_0)t} e^{-j(\omega_1 s_2 + 2a_2 s_1 - \Delta a)t^2} e^{-j2a_2 s_2 t^3}, \tag{30}$$

where for notational simplicity t_n was replaced by t and the constant term omitted. After application of the reference function $s_{\mathrm{ref}}(t) = \exp(j\omega_1 s_2 t^2)\,\mathrm{rect}(t/T_s)$, the point spread function, cf. (18), yields

$$\begin{aligned} p_{\mathrm{D}}(t) &= \int_{-T_s/2}^{T_s/2} e^{-j(\omega_1 s_1 + 2a_2 s_0)(t-t')} e^{-j(\omega_1 s_2 + 2a_2 s_1 - \Delta a)(t-t'^2)} e^{-j2a_2 s_2 (t-t')^3} e^{j\omega_1 s_2 t'^2} dt' \\ &= e^{-j(\omega_1 s_1 + 2a_2 s_0)t} e^{-j(\omega_1 s_2 + 2a_2 s_1 - \Delta a)t^2} e^{-j2a_2 s_2 t^3} \\ &\quad \cdot \int_{-T_s/2}^{T_s/2} e^{j(\omega_1 s_1 + 2a_2 s_0 + 2(\omega_1 s_2 + 2a_2 s_1 - \Delta a)t + 6a_2 s_2 t^2)t'} \\ &\qquad \cdot e^{j(2a_2 s_1 - \Delta a + 6a_2 s_2 t)t'^2} e^{-j2a_2 s_2 t'^3}\, dt'. \end{aligned} \tag{31}$$

Two conditions must be fulfilled to obtain a sharply focussed point spread function:

Table 1: *Second order term $T_s^2 \Delta a$ for oscillator drifts*

	TCXO $\Delta a = 10$ Hz/s	OCXO $\Delta a = 0.1$ Hz/s	OOCXO $\Delta a = 0.01$ Hz/s
Airborne: $T_s = 10$ s	1000	10	1
Space-borne: $T_s = 1$ s	10	0.1	0.01

1. $|2a_2 s_2| \, T_s^3 \leq \pi/2 \quad \Rightarrow \quad |a_2| \leq \frac{\pi}{4 s_2 T_s^3} = \frac{\pi R_b c}{4 v_a^2 T_s^3}$

2. $|\Delta a - 2a_2 s_1 - 6a_2 s_2 t| \, T_s^2 \leq \pi/2 \quad \Rightarrow \quad |\Delta a| \leq \frac{\pi}{2T_s^2}.$

While the first inequality is always fulfilled because $s_1, s_2 \cong 0$, the second one depends on the maximum synthetic aperture time T_s. From Table 1 it is evident that even small oscillator frequency drifts may cause a degradation and widening of the point spread function in the Doppler direction. This loss of Doppler resolution will be significant, particularly for airborne systems with larger synthetic aperture times compared to their space-borne counterparts. It is clear that special SAR modes with higher dwell times, such as spotlight mode, will increase this problem to the point that the focussing behavior may be completely lost.

2.3 Random oscillator phase noise

A further error source for bistatic imaging is the unavoidable physical phenomenon of phase noise or jitter of the oscillators. Jitter describes the frequency instabilities due to random noise processes in any real electronic components [22]. The effect of multiplicative phase noise on bistatic radar performance has been, for instance, investigated in [23].

In contrast to deterministic oscillator (low-frequency) noise types, such as frequency offset or drift, which result in geometric distortions (e.g., loss of resolution and increase of peak sidelobes), wideband phase errors spread out energy widely across the impulse response or point spread function. Rather than causing a smearing of the mainlobe or increasing of the first sidelobes, the phase jitter contributes to an increased sidelobe level over the entire sidelobe range, which results in contrast degradation and noise in the image. A measure of such an error is the integrated sidelobe ratio (ISLR). The ISLR is the ratio of all energy in the sidelobes to the energy in the mainlobe of the impulse response. In its common definition, the division between mainlobe and sidelobe is the location of the first zero crossing of the noise-free impulse response. The significance of the integrated sidelobe energy depends not only on the nature of the sidelobes, but equally important on the distribution of scatterers throughout the scene. If the scene contains mainly a few sparsely distributed bright scatterers, then the ISLR is less important than the peak sidelobe ratio (PSLR), which describes the amount of energy in the highest sidelobe

compared to the mainlobe. High peak sidelobes appear as false targets and hinder detection of closely located weaker targets. In contrast, a low ISLR is important for homogeneous scenes with evenly distributed weaker scatterers, where a high ISLR will degrade contrast by filling in low returns and shadow areas [24].

2.3.1 Wideband (white) phase noise

In order to quantify the resulting ISLR for bistatic SAR, we start with the compressed pulse (23), where the drift terms are replaced by the corresponding phase noise components $\xi_1(t)$ and $\xi_2(t)$ (cf. also (2))

$$P(t) = e^{-j\omega_1\tau}\frac{1}{T}\int_{-T/2}^{T/2} e^{j\pi\frac{B}{T}(t-t'-t_n-\tau)^2} e^{j\Xi_1(t-t'-\tau)} e^{-j\Xi_2(t-t')} e^{-j\pi\frac{B}{T}t'^2}\, dt'. \qquad (32)$$

The capital letters in (32) are used to distinguish stochastic processes from their corresponding realisations. The phase noise terms are modeled as stationary stochastic Gaussian processes $\Xi(t)$ with expectation zero and auto-covariance function

$$c_{\Xi_i\Xi_i}(t) = \frac{1}{2\pi}\int_{-\infty}^{\infty} C_{\Xi_i\Xi_i}(\omega)\, \exp(j\omega t)\, d\omega \qquad \text{with} \qquad c_{\Xi_i\Xi_i}(0) = \sigma_i^2, \qquad (33)$$

where $C_{\Xi_i\Xi_i}(\omega)$ denotes the spectral density function or the power spectrum. The spectral density function is an important performance measure which is usually supplied by the manufacturer of oscillators. For a conventional monostatic SAR where the same oscillator is used for up- and down-conversion, Ξ_2 equals Ξ_1 (cf. section 2.3.3), whereas in the bistatic case, two independent oscillators are used. Hence, Ξ_2 and Ξ_1 are statistically independent. More details and background information about the statistical frequency characteristics of precision clocks and oscillators can, for instance, be found in [22, 25, 26].

As a function of two random processes, the impulse response function (32) is again a stochastic process. For statistically white phase noise, its statistical properties have been determined in terms of the expectation function

$$\mathrm{E}\, P(t) = e^{-\frac{\sigma_1^2+\sigma_2^2}{2}} e^{-j\omega_1\tau} e^{j\pi\frac{B}{T}(t-t_n-\tau)} \operatorname{sinc}(\pi B(t-t_n-\tau)) \qquad (34)$$

and the second moment function

$$\mathrm{E}\,|P(t)|^2 = \sqrt{2}\frac{\left(1-e^{-(\sigma_1^2+\sigma_2^2)}\right)}{T} + e^{-(\sigma_1^2+\sigma_2^2)} \operatorname{sinc}^2(\pi B(t-t_n-\tau)) \qquad (35)$$

Table 2: *Degradation of ISLR due to phase noise.*

IISLR [dB]	σ [rad]
-5	0.56
-10	0.32
-15	0.18
-20	0.10
-25	0.056
-30	0.032

in appendix A. Therefore, the variance of $P(t)$ can be computed as

$$\sigma_p^2(t) = \mathrm{E}\,|P(t)|^2 - |\mathrm{E}\,P(t)|^2 = \frac{\sqrt{2}}{T}\left(1 - e^{-(\sigma_1^2+\sigma_2^2)}\right), \tag{36}$$

which denotes the power of the random part of the stochastic impulse response, and therewith can be used to determine the sidelobe power levels caused by the phase jitter.

Integrating (36) over the entire pulse width T, and using $\exp(-\sigma^2) \approx 1 - \sigma^2$ for small phase noise terms, it becomes evident that the power level is raised over the entire compressed pulse length by the sum of the two phase noise variances. Hence, the increase (i.e., degradation) of the ISLR (IISLR) compared to the undisturbed or phase noise-free case is

$$\mathrm{IISLR} = \sqrt{2}(\sigma_1^2 + \sigma_2^2) = \sqrt{2}\int_{-\infty}^{\infty} C_{\Xi_1\Xi_1}(f) + C_{\Xi_2\Xi_2}(f)\,df = 4\sqrt{2}\int_{0}^{\infty} C_{\Xi\Xi}(f)\,df, \tag{37}$$

where it was assumed that identical oscillator types with $\sigma_1^2 = \sigma_2^2$ are used. The above analysis is analogously applicable to the Doppler direction, where the pulse parameters in (32) are replaced by the Doppler rate in (17), and the pulse duration T is replaced by the synthetic aperture time T_s.

Table 2 lists the allowable phase noise, more specifically the constraint on the standard deviation or root means square (rms) value σ, in order not to exceed a certain degradation in ISLR compared to the noise-free case. A maximum ISLR degradation due to phase noise of IISLR $= -20$ dB is a typical requirement for imaging applications [24].

To illustrate the impact of phase noise graphically, the red curve in Fig. 5 shows the effect of a $\sigma = 0.16$ rms phase jitter (IISLR = -16 dB) on the impulse response function in a bistatic scenario. In contrast, the case of $\sigma = 0.04$ is plotted in blue (IISLR = -28 dB), which is virtually indistinguishable from the error-free case.

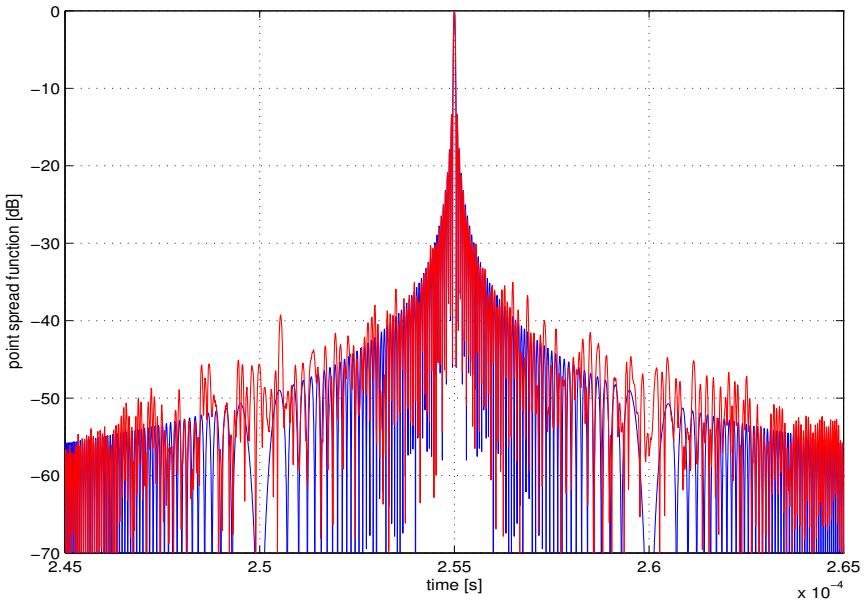

Figure 5 : *Impulse response function in the presence of white phase noise with $\sigma = 0.04$ (blue) and $\sigma = 0.16$ (red).*

2.3.2 Realistic (colored) oscillator phase noise

In practical circumstances, the aforementioned low-frequency and high-frequency components of the phase noise will always occur simultaneously. In order to predict the performance degradation due to phase noise, e.g., the maximum achievable coherent processing time, the single sideband (SSB) power density spectrum $\mathcal{L}(f)$ measured around the particular oscillator output frequency f_0 can be used. This figure is commonly provided by the device manufacturers. The SSB and the spectral density in (33) are related by the multiplication factor M, which is needed to up-convert f_0 to the transmit frequency f_c:

$$C_{\Xi\Xi}(f) = 2M^2\mathcal{L}(f) = 2\left(\frac{f_c}{f_0}\right)^2 \mathcal{L}(f). \tag{38}$$

As examples, Table 3 shows the provided SSBs for three commercially available oscillators, the 58503 from Symmetricom Inc., the high quality oscillator 405681 from Wenzel Inc., and the ultra low phase noise oscillator from Oscilloquarz Inc. Inserting these values into the white noise formula (38) and integrating the result over the entire stated frequency range according to (37) yields rough estimates for the phase noise rms expected from these three oscillators. The calculated variance for the highest quality OSC is, for instance, about 3π and for the others even larger. Evidently, these values are much greater than one radian. Since the white noise assumption is not valid, the small noise approximation in (37) cannot be applied,

Table 3: *Measured SSBs for three commercial oscillators.*

Type	Symmetricom 58503B	Wenzel 405681	Oscilloquarz (OSC)
f_0 [MHz]	10	10	5
f [Hz]	$\mathcal{L}(f)$ [dB]		
0.001	5	-15	-40
0.01	-25	-45	-70
0.1	-55	-75	-100
1	-85	-105	-130
10	-125	-135	-145
100	-135	-160	-152
1000	-140	-176	-155
10000	-145	-176	-157

i.e., the IISLR cannot be specified by this formula. Nevertheless, is it obvious that all oscillator types exceed substantially the requirement.

In addition, these estimated values represent the phase jitter variance or standard deviation based on a very large time base. In the considered case, it is the phase rms over $T = 1/f_{\min} = 1000$ s. In practice, however, the time interval over which any decorrelation, i.e., random phase variation, will effect the impulse response function is much smaller. For bistatic SAR, this time is identical to the synthetic aperture time T_s, which typically ranges from about one second in space-based SAR, to a few seconds in airborne stripmap SAR, and up to hundreds of seconds in wide-range spotlight mode SAR applications [27]. For finite T_s, the rms phase value σ has been calculated in appendix B; it can be determined via the integral

$$\sigma^2 = 2 \int_{-\infty}^{\infty} C_{\Xi\Xi}(f) \left(1 - \operatorname{sinc}^2\left(\frac{\omega T_s}{2}\right)\right) df \cong 4 \int_{0.443/T_s}^{\infty} C_{\Xi\Xi}(f)\, df. \qquad (39)$$

Reducing the lower integration bound to about $1/(2T_s)$ was found to give more accurate results than the limit $1/T_s$ stated in some publications, e.g., [23]. The black curve in Fig. 6 shows the IISLR ($10\log(\sigma^2)$) in (39) for the OSC oscillator over increasing synthetic aperture time T_s, which was varied from 0.1 s to 50 s. The point of intersection with the -20 dB limit for the IISLR indicates a maximum T_s of about 10 seconds.

However, even the rms phase in (39) does not reveal the full impact of jitter on the point spread function. This is illustrated in Fig. 7, where the undisturbed point spread function is shown along with several realisations that include phase noise, which are simulated via OSC's spectral density in Table 3. Although Fig. 6 would

indicate a relatively large IISLR of -10 dB for the chosen time $T_s = 30$ s, almost no random raise in the sidelobes further away from the mainlobe are recognisable in Fig. 7 (a). In contrast, Fig. 5 shows a significant increase in the sidelobes for an evidently smaller IISLR of -16 dB.

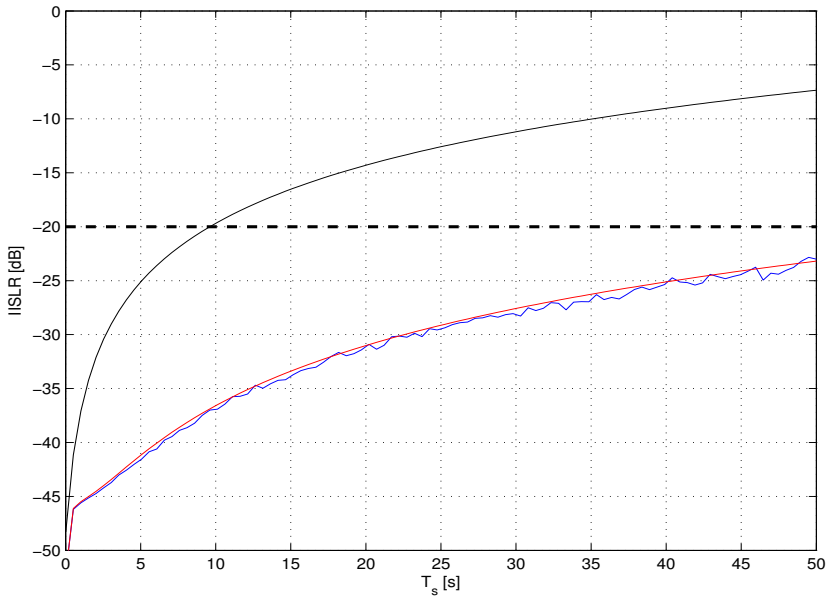

Figure 6 : *IISLR of OSC's oscillator for increasing synthetic aperture time, upper curve based on eq. (39), lower curve based on eq. (42).*

This seeming contradiction can be explained with the fact that (39) does not distinguish between the different effects of low-frequency and high-frequency components of the phase noise. Low-frequency phase noise components will lead to geometric distortions (cf. Section 2.2) but no increase in sidelobe power, which in fact is exclusively caused by the high-frequency components, see Section 2.3. Fig. 7 (b) confirms the randomly increased peak sidelobes due to the low-frequency components.

Therefore, a much more meaningful metric to describe the overall phase noise impact must remove the low-frequency (slowly-time varying) components before determining the IISLR. For instance, we can model these low-frequency components as a low-order polynomial function in time. In most cases, an order of three for the phase function (corresponding to quadratic frequency terms) is sufficient:

$$\Xi(t) = b_0 + b_1 t + b_2 t^2 + b_3 t^3 + \Upsilon(t), \tag{40}$$

where $\Upsilon(t)$ represents the remaining high-frequency phase noise. A similar approach has been used to predict the baseline accuracy between platforms in bistatic

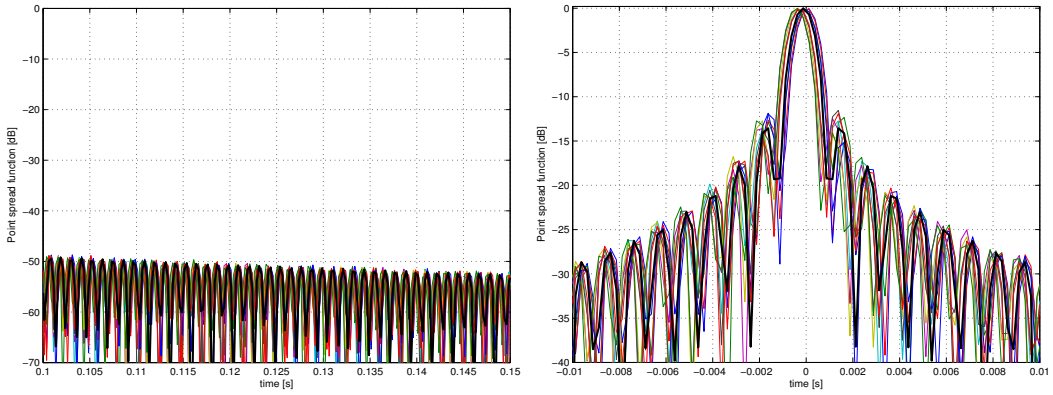

(a) Sidelobe region around -50 dB.

(b) Mainlobe region.

Figure 7: *Ideal point spread function (black) along with ten realisations including phase noise with spectral density in the right-hand column of table 3.*

interferometry [28], in which a direct link between the two radars with a maximum decorrelation time in the order of the PRI was proposed. On the other hand, we are interested in indirect synchronisation over significantly longer integration times.

As mentioned before, estimates of the coefficients $\underline{b} = [b_0, \ldots, b_3]'$ will give insight into the geometric distortions of the point spread function, and the variance of Υ will describe the radiometric distortions, i.e., the increase in ISLR. Taking both effects into account simultaneously will then yield the maximum allowable coherent processing or synthetic aperture time. Since the phase noise process $\Phi(t)$ is assumed to be normally distributed, all estimated coefficients $\hat{b}_i$ are shown (annex C) to be Gaussian random variables with zero mean and variance

$$\sigma^2_{\hat{b}_i} = 4 \int_0^\infty C_{\Xi\Xi}(f)\ |V_i(f)|^2\, df \qquad\qquad i = 0, \ldots, 3, \tag{41}$$

where $V_i(f)$ is the Fourier-transform of $v_i(t)$ defined in (C.13).

Similarly, the variance of the remaining high-frequency phase noise components are calculated in annex C as

$$\sigma^2_{\Upsilon} = 4 \int_0^\infty C_{\Xi\Xi}(f)\ |\tilde{A}(f)|^2\, df, \tag{42}$$

where it can be shown that $V_i(f)$ and $\tilde{A}(f)$ have high-pass character with increasing

cut-off frequencies as larger polynomial orders in (40) are chosen. Therefore, the larger the order the lower the integrated power under the spectral density function (cf. (39)) and the smaller the variance of the remaining high-frequency phase noise.

In summary, the derived statistics of the polynomial coefficients and the variance of the remaining high-frequency phase noise can be used to predict the geometric and radiometric distortions of the point spread function. The constant parameter b_0 is unimportant and the linear term b_1 is circumstantial because it introduces only a shift of the function, which can also be seen in Fig. 7. Reduced resolution and increased peak sidelobes are due to b_2 and b_3 only. As a rule of thumb, these parameters must not exceed the following thresholds (compare (31))

$$|b_2| \leq \frac{\pi}{4T_s^2} \qquad \text{and} \qquad |b_3| \leq \frac{\pi}{6T_s^3}. \tag{43}$$

The magnitude of the normally distributed estimates $\hat{b}_2$ and $\hat{b}_3$ are governed by the probability density function (pdf) $f_{|\hat{b}_i|}(\hat{b}_i) = 2f_{\hat{b}_i}(\hat{b}_i)u(\hat{b}_i)$ where $u(\hat{b}_i)$ denotes the unity step function [29, 30]. The mean value of each estimator is give as

$$\mathrm{E}\,|\hat{b}_i| = \sqrt{\frac{2}{\pi}}\,\sigma_{\hat{b}_i} \qquad \text{for} \quad i = 0, \ldots, 3, \tag{44}$$

and hence depends only on the variance in (41). Figure 8 compares these mean values of the polynomial coefficients with the thresholds in (43) for increasing synthetic aperture times T_s. The two curves intersect with the thresholds at roughly 11 s for b_3 and 32 s for b_2, respectively, where the smaller value obviously sets the upper bound for the maximum T_s. For confirmation of the theoretical results, the mean value of ten simulated coefficients for each T_s are superimposed showing almost perfect agreement with the theoretical results.

The corresponding remaining IISLR after subtraction of these estimates is plotted in Fig. 6 (red curve), where it it is evident that the sidelobe levels are now always below the requirement of -20 dB for $T_s < 50$ s.

Figure 8 does not shed light on how often we expect that geometric distortions will occur. In fact, by comparing only the mean value, we know that about 50 % of the time the values will be larger than the threshold, and the other 50 % will be smaller. Therefore, we may calculate the probability that $|\hat{b}_i|$ is larger then the corresponding threshold,

$$\begin{aligned} \mathrm{P}\left\{|\hat{b}_i| > \frac{\pi}{2iT_s^i}\right\} &= 1 - \mathrm{P}\left\{|\hat{b}_i| < \frac{\pi}{2iT_s^i}\right\} = 2\left(1 - \mathrm{P}\left\{\hat{b}_i < \frac{\pi}{2iT_s^i}\right\}\right) \\ &= 2\left(1 - \mathrm{P}\left\{d_i < \frac{\pi}{2i\sigma_{\hat{b}_i}T_s^i}\right\}\right) = 2\left(1 - \Phi\left(\frac{\pi}{2i\sigma_{\hat{b}_i}T_s^i}\right)\right), \end{aligned} \tag{45}$$

where $\Phi(\cdot)$ is the cumulative distribution function of the standard normally distributed random variable d_i (error-function), i.e., with zero mean and unity variance.

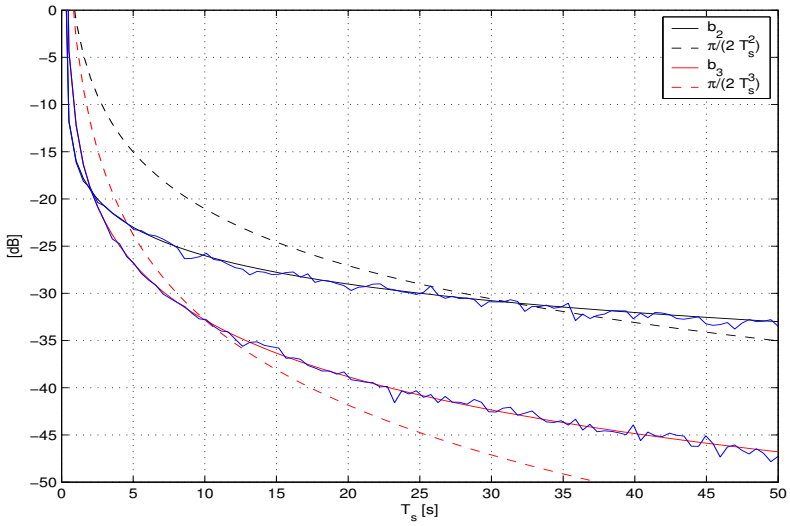

Figure 8 : *Mean values of the polynomial coefficients with corresponding thresholds versus synthetic aperture time.*

Figure 9 shows the corresponding probabilities for the quadratic and cubic coefficients. If, for instance, one is only willing to accept some geometric distortion one out of ten times (i.e., 10 %), e.g., one out of ten flight lines during an experiment, then the coherent processing time must be limited to about $T_s = 5$ s.

It was found by simulation that these conditions are rather conservative and that the thresholds can in many case be relaxed to

$$|b_2| \leq \frac{\pi}{2T_s^2} \qquad \text{and} \qquad |b_3| \leq \frac{\pi}{2T_s^3}, \tag{46}$$

for which the probabilities are also plotted in Fig. 9. For the same number of allowed oversteppings, i.e., 10 %, the maximum allowed synthetic aperture time is now about 15 s.

Although Fig. 9 gives an indication of how often the thresholds are exceeded, it does not show by how much, i.e., the actual impact on the point spread function. In other words, if the thresholds are only exceeded by a relatively small amount, the geometric distortions (such as wider mainlobe or non-symmetric sidelobes) are expected to be negligible. An indicator of such behavior can be seen in Fig. 8, where the mean values of $\hat{b}_2$ and $\hat{b}_3$ are shown to stay quite close to the thresholds for increasing T_s behind the intersection point. This observation is also confirmed by

the simulation in Fig. 7 (b), where only minor distortions (1 to 2 dB increase of peak sidelobe) can be recognized even for the relatively long T_s of 30 s. In particular, the point spread function appears perfectly symmetric although a significant cubic phase term was predicted in Fig. 8 (two bottom curves). A further reduction of these sidelobe contributions (distortions) due to the low-frequency phase noise may be achieved by using weighting functions (e.g., Hamming) during the convolution.

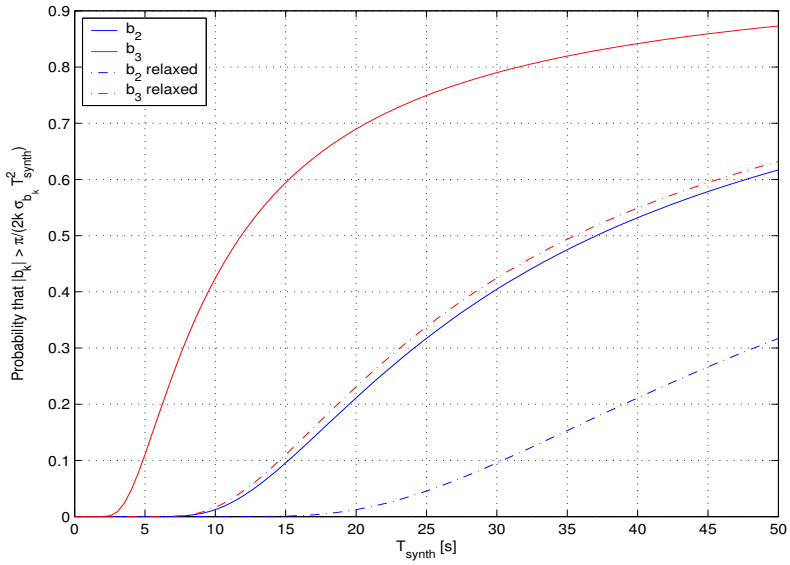

Figure 9 : *Probability that the polynomial coefficients are larger than the required threshold.*

As a consequence, a performance analysis based on simulations may be preferable in some cases compared to pure theoretical predictions via those metrics derived above. Simulations can, for instance, be used to find those values of T_s for which the 3 dB-width of the mainbeam increases by a given amount, or for which the peak sidelobe has been doubled, etc. Such simulations can be performed by simply using the given (measured or provided) spectral density function of any arbitrary oscillator as the sole input.

Beyond the possibility of predicting and avoiding the performance degradation of bistatic SAR resolution in the presence of particularly severe phase noise by simply using higher quality oscillators, there exists the opportunity to estimate and remove the low-frequency (slowly varying) phase error prior to imaging. The applicable techniques are identical to those used for 'auto-focussing', i.e., motion compensation based on the measured data alone [31, 32]. The suitability of some of these techniques will be explored in phase II of this project.

Another important problem not addressed so far is the impact of motion and/or vibration of the oscillator to its phase noise characteristics. It is well demonstrated that oscillator's nominal frequency reacts sensitively to motion and accelerations, which is usually provided as the parameter 'g-sensitivity' by the manufacturer. Oscillators with small f_0 suffer more from this deficiency because of their increased physical size compared to higher frequency oscillators. In contrast, lower frequency oscillators commonly possess a much better (lower) phase noise characteristic. Some preliminary measurements are introduced in section 6.3. However, extensive laboratory experiments are being executed during the writing of this report and will also be addressed in phase II.

2.3.3 Comparison to monostatic case

It is important to realize that the requirements on oscillator quality with respect to phase noise are much more stringent in bistatic than in monostatic SAR due to the use of two separate oscillators. In monostatic SAR the same oscillator is used to up- and down-convert the signal for each pulse. Although the oscillator frequency varies along azimuth-time (according to its power spectrum), the received signals can maximally decorrelate over the round-trip travel time (PRI) of each pulse. This can be seen by replacing the combined spectral density function $C_{\Xi\Xi}(\omega)$ in (37) with its monostatic counterpart. Consider the phase term difference in (32) for the monostatic case $\Xi(t) = \Xi_1(t-\tau) - \Xi_1(t)$ for which the covariance function can be calculated as

$$\begin{aligned} c_{\Xi\Xi}(t') &= \mathrm{E}\,\Xi(t+t')\Xi^*(t) \\ &= \mathrm{E}\,\left(\Xi_1(t+t'-\tau) - \Xi_1(t+t')\right)\left(\Xi_1(t-\tau) - \Xi_1(t)\right)^* \\ &= 2c_{\Xi_1\Xi_1}(t') - c_{\Xi_1\Xi_1}(t'+\tau) - c_{\Xi_1\Xi_1}(t'-\tau). \end{aligned} \tag{47}$$

Using the shift property of the Fourier-transform yields for the spectral density function

$$\begin{aligned} C_{\Xi\Xi}(\omega) &= 2C_{\Xi_1\Xi_1}(\omega) - C_{\Xi_1\Xi_1}(\omega)e^{j\omega\tau} - C_{\Xi_1\Xi_1}(\omega)e^{-j\omega\tau} \\ &= 2\big(1-\cos(\omega\tau)\big)C_{\Xi_1\Xi_1}(\omega) = 4\sin^2\left(\frac{\omega\tau}{2}\right)C_{\Xi_1\Xi_1}(\omega). \end{aligned} \tag{48}$$

Equation (47) reveals a kind of high-pass filtering to the spectral density function because low-frequency components are suppressed with a $\sin^2$-characteristic below frequencies of $1/\tau$. Integration of (48) over this frequency range yields

$$\sigma_\Xi^2 = 4\int_{-\infty}^{\infty} C_{\Xi\Xi}(f)\sin^2\left(\frac{f\tau}{2}\right)\,df \cong 8\int_{1/\tau}^{\infty} C_{\Xi\Xi}(f)\,df, \tag{49}$$

which corresponds to an monostatic IISLR of -28 dB for the Symmetricom, -40 dB for the low noise oscillator from Wenzel, and about -52 dB for the ultra-low phase noise oscillator form OSC.

3 Bistatic observation time

One parameter of major importance for bistatic SAR is the time period for which a scatterer on a particular location on the ground is observed simultaneously by both radars. In order to calculate this time, the individual time-dependent range vectors (1) for the transmitter and receiver are transformed into the antenna coordinate system by

$$\underline{R}_{i,\mathrm{a}}(t,\underline{r}) = \mathbf{L}_{\mathrm{as}}\,\underline{R}_{i,\mathrm{s}}(t,\underline{r}) = \mathbf{L}(\Phi_i(t),0,\Psi_i(t))\mathbf{L}(\pi,0,\Psi_v)\,\underline{R}_{i,\mathrm{s}}(t,\underline{r}) \tag{50}$$

for $i = 1, 2$, where Ψ_v denotes the constant course angle defined in appendix E.3. $\Phi_i(t)$ and $\Psi(t)$ are the azimuth and elevation (depression) angles (appendix E.4) which are in general adjusted over time, depending on the particular SAR mode used:

- Stripmap or squinted stripmap mode: $\Phi_i(t) = \Phi_{i,0}$ and $\Psi_i(t) = \Psi_{i,0}$, where $\Phi_{i,0}$ and $\Psi_{i,0}$ are the squint angle and depression angle to the center of the scene at time $t = 0$.
- Spotmode: $\Phi_i(t)$ and $\Psi_i(t)$ are updated from pulse to pulse so that the antenna is always pointing at center of the scene ($\underline{r} = 0$).

It is obvious that the bistatic observation time can almost be arbitrarily chosen in spotmode operations, as long as the scatterer is within the overlap region of both antenna footprints. For stripmap operations, however, where the beam pointing of the antenna is kept fixed over the measurement interval, the bistatic observation time is principally limited. Depending on the flight trajectories of both platforms, the maximum observation time may vary significantly for different areas on the ground. In order to assess whether a particular point on the ground is simultaneously 'seen' at a certain instant in time, the directional cosine u_i and sine v_i of both radars must be computed:

$$\begin{aligned} u_i(t,\underline{r}) &= \frac{\underline{u}_x'\underline{R}_{i,a}(t,\underline{r})}{||\underline{R}_{i,a}(t,\underline{r})||} = \sin\Psi_i(t,\underline{r})\cos\Phi_i(t,\underline{r}) \\ v_i(t,\underline{r}) &= \frac{\underline{u}_z'\underline{R}_{i,a}(t,\underline{r})}{||\underline{R}_{i,a}(t,\underline{r})||} = \sin\Phi_i(t,\underline{r}), \end{aligned} \tag{51}$$

where $\underline{u}_x = [1,0,0]'$ and $\underline{u}_z = [0,0,1]'$. The bistatic observation time T_{b} is then given as the integral

$$T_{\mathrm{b}}(\underline{r}) = \int_{-\infty}^{\infty} I_1(t,\underline{r}) \cdot I_2(t,\underline{r})\,dt, \tag{52}$$

where the indicator functions are defined as

$$I_i(t,\underline{r}) = \begin{cases} 1 & \text{if} \quad |u_i(t,\underline{r}) - u_{0,i}| \le u_{3\text{dB,i}}/2 \\ & \quad\;\; |v_i(t,\underline{r}) - v_{0,i}| \le v_{3\text{dB,i}}/2 \\ 0 & \quad\;\; \text{elsewhere.} \end{cases} \tag{53}$$

$u_{0,i}$ and $v_{0,i}$ are the directional cosine and sine corresponding to the azimuth and elevation angles $\Phi_{0,i}$ and $\Psi_{0,i}$ of both platforms to the scene center at time origin. The antenna beamwidth in either direction are herein denoted by the subscript '3dB'.

By inserting (1) into (51), it is possible to solve the inequality of (53) analytically. The derivation is exemplified below for the directional cosine where, for convenience, the transmitter/receiver subscript i is omitted:

$$u(t,\underline{r}) = \frac{\underline{u}_x' \mathbf{L}_{\text{as}} (\underline{R}_0 - \underline{r}) + \underline{u}_x' \mathbf{L}_{\text{as}} \underline{v}\, t}{\sqrt{||\underline{R}_0 - \underline{r}||^2 + 2(\underline{R}_0 - \underline{r})' \underline{v}\, t + ||\underline{v}||^2\, t^2}} \le \eta, \tag{54}$$

where $\eta = u_0 + u_{3\text{dB}}/2$, which can be re-written as

$$\begin{aligned} (a_0 + a_1\, t)^2 &\le \eta^2 \left(b_0 + b_1\, t + b_2\, t^2\right) \\ c_2\, t^2 + c_1\, t + c_0 &= 0, \end{aligned} \tag{55}$$

with

$$\begin{aligned} a_0 &= \underline{u}_x' \mathbf{L}_{\text{as}} (\underline{R}_0 - \underline{r}) \\ a_1 &= \underline{u}_x' \mathbf{L}_{\text{as}} \underline{v} \\ b_0 &= ||\underline{R}_0 - \underline{r}||^2 \\ b_1 &= 2(\underline{R}_0 - \underline{r})' \underline{v} \\ b_2 &= ||\underline{v}||^2, \end{aligned} \tag{56}$$

and $c_0 = a_0^2 - \eta^2 b_0$, $c_1 = 2a_0 a_1 - \eta^2 b_1$ and $c_2 = a_1^2 - \eta^2 b_2$. The solution of (55) is given as

$$t_{1,2} \le -\frac{c_1}{2c_2} \mp \sqrt{-\frac{c_0}{c_2} + \frac{c_1^2}{4c_2^2}} \qquad \text{for} \qquad c_2 \ne 0, \tag{57}$$

Depending on the sign of c_2, different cases for the solution must be distinguished. According to Fig. 10, there is either no real solution if the parabola does not cross the x-axis, or two real solutions in the specified gray regions.

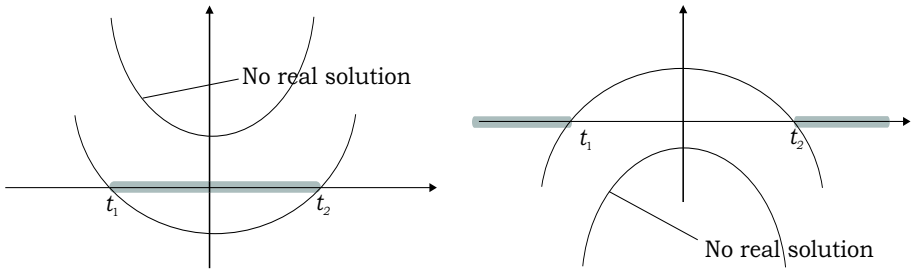

Figure 10 : *Regions of possible solutions for the bistatic observation time.*

Comparing the minima and maxima of the individual solutions for u and v for both transmitter and receiver yields the maximum observation time for each scatterer on the ground:

$$T_{\mathrm{b}}(\underline{r}) = \max\left(0, t_{\max}(\underline{r}) - t_{\min}(\underline{r})\right), \tag{58}$$

where

$$\begin{aligned} t_{\min} &= \max\left(t_1^{u_1}, t_1^{u_2}, t_1^{v_1}, t_1^{v_2}\right) \\ t_{\max} &= \min\left(t_2^{u_1}, t_2^{u_2}, t_2^{v_1}, t_2^{v_2}\right), \end{aligned} \tag{59}$$

and where '$\max(x, y, z)$' means the largest of each value x, y and z.

Figure 11 demonstrates the variation of bistatic observation time $T_b(\underline{r})$ given by (58) for each pixel on the ground for different bistatic angles between transmitter and receiver. In this case, the transmitter is chosen to be an aircraft with parameters listed in Table 4. The receiver is located on top of a stationary tower with parame-

Table 4: *Airborne transmitter parameters.*

Altitude	$H_1 = 5000$ m
Velocity	$\underline{v}_1 = 132\,\underline{u}_x$ m/s
Elevation angle to scene centre at $t = 0$	$\Phi_{0,1} = 10°$
Squint angle to scene centre at $t = 0$	$\Psi_{0,1} = 0°$
Antenna pattern	sinc
Azimuth beamwidth	$u_{3\mathrm{dB},1} = 4°$
Elevation beamwidth	$u_{3\mathrm{dB},1} = 2.5°$

ters listed in Table 5, where the receiver squint (azimuth) angle $\Psi_{0,2}$ is varied, see appendix F. $\Psi_{0,2} = 0°$ means the aircraft is flying behind the tower and both antennas are pointing in the same direction (i.e., a quasi-monostatic geometry). In contrast, $\Psi_{0,2} = 0°$ indicates that the aircraft is flying in front of the radar perpendicular to the receiver antenna pointing direction, resulting in a forward-scattering

Table 5: *Tower receiver parameters.*

Altitude	$H_2 = 20$ m
Velocity	$\underline{v}_2 = 0$ m/s
Elevation angle to scene centre at $t = 0$	$\Phi_{0,2} = 0.5^\circ$
Antenna pattern	sinc
Azimuth beamwidth	$u_{3\text{dB},2} = 45^\circ$
Elevation beamwidth	$u_{3\text{dB},2} = 10^\circ$

geometry. It is evident that the maximum observation time is relatively large ($T_s \approx$ 12 to 16 s) because of the shallow elevation angle of the transmitter, which results in large distances to the scene on the ground. A larger distance means an increased synthetic aperture time for a given azimuth beamwidth. Also recognizable are the different regions on the ground which are bistatically observable due to the change in receiver location and orientation. Of course, much more complex illumination shapes are usually possible when the receiver is also moving.

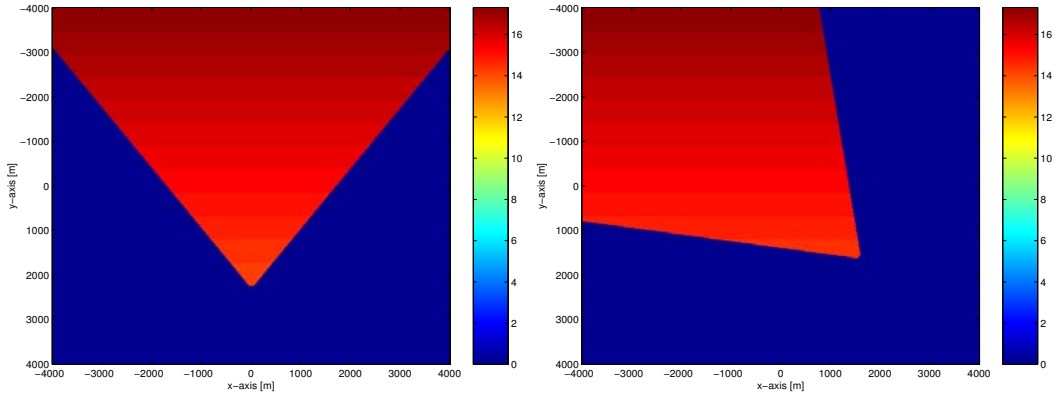

(a) Quasi-monostatic geometry, bistatic angle = $0°$.

(b) Bistatic angle = $45°$.

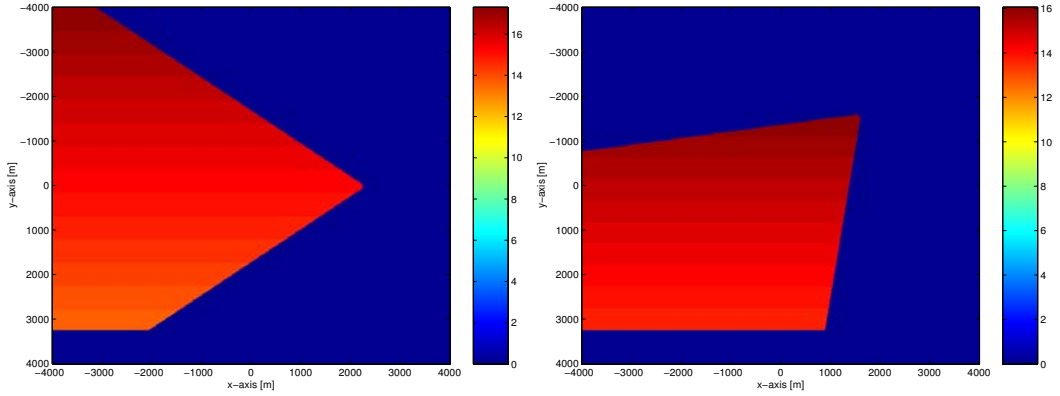

(c) Bistatic angle = $90°$.

(d) Bistatic angle = $135°$.

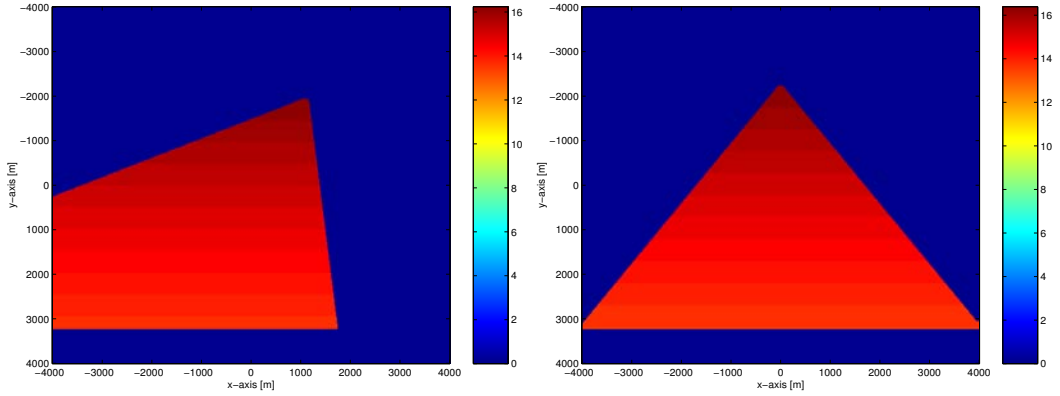

(e) Bistatic angle = $150°$.

(f) Forward-looking geometry, bistatic angle = $180°$.

Figure 11: *Bistatic observation time of ground range scatterer. Stationary receiver and airborne transmitter for varying bistatic angles $\Psi_{0,2}$.*

4 Bistatic SAR performance analysis

The aim of this section is to derive tractable mathematical tools to determine the bistatic SAR resolution for individual points on the ground for arbitrary transmitter and receiver flight geometries. The term resolution in this context means the ability to separate close targets in different areas on the ground. A similar approach was applied for a parasitic SAR system in [15].

These tools will allow performance comparisons of different flight geometries without the necessity of SAR processing, i.e., the complex and sometimes time-consuming computation of the point spread function, e.g., [17]. They could also be used in an opposite way during the flight planning phase of operations to determine the necessary flight geometry (and velocities) for a required minimum ground resolution in a particular region of interest.

It is important to note that the analysis herein is based on a fully three-dimensional scenario, i.e., it is not restricted to two-dimensional geometries as is sometimes done in the literature. Further, constant velocities for the radar platforms are only chosen for clarity of the derivation. Accelerations or non-constant altitudes can easily be included in the analysis.

4.1 Preliminaries: Doppler-bandwidth, Doppler-gradient and the k-space

In order to determine SAR resolution, it is crucial to understand the physical phenomena describing the composition of the synthetic aperture and therewith allowing the imaging of the desired reflectivity with high resolution. This is even more important as the general bistatic case is usually much more complex than the relatively simple monostatic case. For the monostatic case, for instance, it is common in the literature to use the Doppler-bandwidth (the maximum spread of Doppler frequency) of a scatterer on the ground to calculate the corresponding azimuth (cross-range or Doppler) resolution. In this subsection we want to show that the idea of bandwidth can only be applied to the monostatic non-squinted case. Instead of Doppler-bandwidth, the shape of the point spread function (and therewith the resolution) is determined instead by the magnitude of the Doppler-gradient vector, or, in even more general terms, by the the form and extent of the wavenumber vector or k-space. In fact, both are identical only for the very special case of side-looking monostatic SAR. An excellent introduction to this topic can be found in the overview article by Ender [33]. Although the term ‘Doppler resolution’ might be somewhat misleading, because it is commonly linked to Doppler bandwidth, we have adopted the term for notational convenience.

The starting point to determine the resolution of bistatic SAR is the three-dimensional geometry depicted in Fig. 3. The effective range vector from the transmitter (from hereon indicated by subscript 1) to the point $\underline{r}$ on the ground and back to the receiver (subscript 2) at time t is given as the sum

$$\underline{R}(t,\underline{r}) = \underline{R}_1(t,\underline{r}) + \underline{R}_2(t,\underline{r}) = \left(\underline{R}_{0,1} - \underline{r}\right) + \underline{v}_1 t + \left(\underline{R}_{0,2} - \underline{r}\right) + \underline{v}_2 t, \qquad (60)$$

where $\underline{R}_{0,i} = \underline{R}_i(0,\underline{0})$ are the ranges from the scene center to either platform at time zero. Determined by the distance between the transmitter and the receiver, the resulting phase history of the received signal yields

$$\phi(t,\underline{r}) = k\left(||\underline{R}_1(t,\underline{r})|| + ||\underline{R}_2(t,\underline{r})||\right), \qquad (61)$$

where $k = 2\pi/\lambda$ denotes the wavenumber. The Doppler frequency is given by the first derivative of (61) as

$$\begin{aligned}
\omega_D(t,\underline{r}) \equiv \dot{\phi}(t,\underline{r}) &= \frac{d\phi(t,\underline{r})}{dt} = \\
&\quad k\frac{\underline{v}_1'\left(\left(\underline{R}_{0,1} - \underline{r}\right) + \underline{v}_1 t\right)}{\sqrt{\left(\left(\underline{R}_{0,1} - \underline{r}\right) + \underline{v}_1 t\right)'\left(\left(\underline{R}_{0,1} - \underline{r}\right) + \underline{v}_1 t\right)}} \\
&\quad + k\frac{\underline{v}_2'\left(\left(\underline{R}_{0,2} - \underline{r}\right) + \underline{v}_2 t\right)}{\sqrt{\left(\left(\underline{R}_{0,2} - \underline{r}\right) + \underline{v}_2 t\right)'\left(\left(\underline{R}_{0,2} - \underline{r}\right) + \underline{v}_2 t\right)}} \\
&= k\left(\underline{v}_1'\underline{u}_{\underline{R}_1}(t,\underline{r}) + \underline{v}_2'\underline{u}_{\underline{R}_2}(t,\underline{r})\right), \qquad (62)
\end{aligned}$$

where $\underline{u}_{\underline{a}} = \underline{a}/||\underline{a}||$ is the unit vector in direction $\underline{a}$. For simplicity, the unit vector in direction $\underline{R}_i$ will be referred to as $\underline{u}_i$. Combining the scalar k and the unit direction vectors to the wavenumber vector $\underline{k}_i(t,\underline{r}) = k\underline{u}_i(t,\underline{r})$ with physical unit m^{-1}, the Doppler frequency yields

$$\omega_D(t,\underline{r}) = \underline{v}_1'\,\underline{k}_1(t,\underline{r}) + \underline{v}_2'\,\underline{k}_2(t,\underline{r}). \qquad (63)$$

Using (63), the slope of the Doppler frequency as the second derivative of the phase $s_D(t,\underline{r}) \equiv \ddot{\phi}(t,\underline{r})$ is given as

$$s_D(t,\underline{r}) = \frac{d\omega_D(t,\underline{r})}{dt} = \underline{v}_1'\,\dot{\underline{k}}_1(t,\underline{r}) + \underline{v}_2'\,\dot{\underline{k}}_2(t,\underline{r}), \qquad (64)$$

which can be further written as

$$s_D(t,\underline{r}) = k\left(\underline{v}_1'\dot{\underline{u}}_1(t,\underline{r}) + \underline{v}_2'\dot{\underline{u}}_2(t,\underline{r})\right)$$

$$
\begin{aligned}
&= k\underline{v}_1' \left(\frac{\underline{v}_1}{||\underline{R}_1(t,\underline{r})||} - \frac{\underline{R}_1(t,\underline{r})\underline{R}_1(t,\underline{r})'\underline{v}_1}{||\underline{R}_1(t,\underline{r})||^3} \right) \\
&\quad + k\underline{v}_2' \left(\frac{\underline{v}_2}{||\underline{R}_2(t,\underline{r})||} - \frac{\underline{R}_2(t,\underline{r})\underline{R}_2(t,\underline{r})'\underline{v}_2}{||\underline{R}_2(t,\underline{r})||^3} \right) \\
&= \frac{k\underline{v}_1'\mathbf{P}^{\perp}_{\underline{R}_1}(t,\underline{r})\underline{v}_1}{||\underline{R}_1(t,\underline{r})||} + \frac{k\underline{v}_2'\mathbf{P}^{\perp}_{\underline{R}_2}(t,\underline{r})\underline{v}_2}{||\underline{R}_2(t,\underline{r})||}, \qquad (65)
\end{aligned}
$$

where $\mathbf{P}^{\perp}_{\underline{a}}$ describes the projection operator (matrix) onto the complement of vector $\underline{a}$.

At the same time, the gradient of $\phi(t,\underline{r})$:

$$
\underline{\nabla}\phi(t,\underline{r}) = \left[\frac{\partial\phi}{\partial x}\underline{x},\ \frac{\partial\phi}{\partial y}\underline{y},\ \frac{\partial\phi}{\partial z}\underline{z} \right]',
$$

in (61), at point $\underline{r}$ can be calculated as

$$
\underline{\nabla}\phi(t,\underline{r}) = -\frac{k\underline{R}_1}{||\underline{R}_1(t,\underline{r})||} - \frac{k\underline{R}_2}{||\underline{R}_2(t,\underline{r})||} = -\underline{k}_1(t,\underline{r}) - \underline{k}_2(t,\underline{r}). \qquad (66)
$$

The gradient of the phase (distance) function determines the direction and the maximum rate of change of distance. Analogously, the gradient of $\dot{\phi}(t,\underline{r})$, which is identical to the gradient of the Doppler frequency, yields

$$
\underline{\nabla}\dot{\phi}(t,\underline{r}) = \frac{d\underline{\nabla}\phi(t,\underline{r})}{dt} = -\dot{\underline{k}}_1(t,\underline{r}) - \dot{\underline{k}}_2(t,\underline{r}) \equiv \underline{\nabla}\omega_D(t,\underline{r}), \qquad (67)
$$

which describes the direction and maximum rate of change of Doppler frequency for any point $\underline{r}$ on the ground. Its physical unit is Hz/m. From (65), the first derivative of the wavenumber vector vector can be identified as

$$
\dot{\underline{k}}_i(t,\underline{r}) = \frac{k}{\|\underline{R}_i(t,\underline{r})\|}\mathbf{P}^{\perp}_{\underline{R}_i}(t,\underline{r})\underline{v}_i. \qquad (68)
$$

Note that the Doppler gradient is simply given as the negative sum of the two individual wavenumber vectors, whereas the Doppler frequency represents the component of the wavenumber vectors projected onto the velocity vectors. The same applies to the Doppler frequency slopes and Doppler gradient slopes.

4.2 Doppler-resolution

From this k-space analysis, for instance [33], it is known that the resolution (defined as the width of the point spread function) in each possible direction is determined

by the reciprocal of the maximum extent/spread of the k-set in this particular direction. The idea of using the gradient to calculate this maximum extent, i.e., to examine the bistatic SAR resolution, was originally utilised in [34] and later also in [7, 35]. However, these authors only considered the wavenumber vectors at the time origin and neglected their change over time, i.e., they assumed the gradient to be constant over time. This is a rather crude approximation, which is valid only for near-monostatic (non-squinted) configurations.

Including the time dependency of the Doppler gradient (67), the maximum k-set spread in Doppler direction, denoted by S_D, can be calculated as the norm of the vector integral

$$S_D(\underline{r}) = \frac{1}{2\pi} \left\| \int_{t_{\min}}^{t_{\max}} \underline{\nabla}\omega_D(t, \underline{r})\, dt \right\|. \tag{69}$$

The integral must be computed over the maximum bistatic observation time for the considered ground point $\underline{r}$. The times $t_{\min}$ and $t_{\max}$ denote the first and last instant in time that this ground point is 'seen' from both radar antennas, i.e., lies simultaneously within both antenna patterns. For radar platforms traveling with constant velocities, the bistatic observation time was calculated analytically in Section 3.

Using (67), this becomes in closed form

$$\begin{aligned} S_D(\underline{r}) &= \frac{1}{2\pi} \left\| \int_{t_{\min}}^{t_{\max}} \dot{\underline{k}}_1(t, \underline{r}) + \dot{\underline{k}}_2(t, \underline{r})\, dt \right\| \\ &= \frac{1}{\lambda} \| \underline{u}_1(t_{\max}, \underline{r}) - \underline{u}_1(t_{\min}, \underline{r}) + \underline{u}_2(t_{\max}, \underline{r}) - \underline{u}_2(t_{\min}, \underline{r}) \|. \end{aligned} \tag{70}$$

Hence, the exact solution for the resolution in Doppler direction Δ_D in meter is given as the inverse of (70):

$$\Delta_D(\underline{r}) = S_D^{-1} = \frac{\lambda}{\| \underline{u}_1(t_{\max}, \underline{r}) - \underline{u}_1(t_{\min}, \underline{r}) + \underline{u}_2(t_{\max}, \underline{r}) - \underline{u}_2(t_{\min}, \underline{r}) \|}. \tag{71}$$

The physical interpretation of (71) is that the Doppler resolution is given as the inverse of the sum of the maximum aspect angle variation of both platforms.

In contrast, the maximum Doppler bandwidth B_D based on (63) is given as

$$B_D(\underline{r}) = \frac{k}{\|\underline{v}_1\|^2} \underline{u}'_{\underline{v}_1} \big(\underline{u}_1(t_{\max}, \underline{r}) - \underline{u}_1(t_{\min}, \underline{r}) \big) + \frac{k}{\|\underline{v}_2\|^2} \underline{u}'_{\underline{v}_2} \big(\underline{u}_2(t_{\max}, \underline{r}) - \underline{u}_2(t_{\min}, \underline{r}) \big), \tag{72}$$

which represents the sum of maximum aspect angle variation projected onto either flight direction. In the monostatic case, with $\underline{u}_1(t_{\max}, \underline{r}) - \underline{u}_1(t_{\min}, \underline{r}) \equiv$

$\underline{u}_2(t_{\max}, \underline{r}) - \underline{u}_2(t_{\min}, \underline{r})$, which we will call $\underline{a}$ for convenience, the Doppler bandwidth is

$$B_D(\underline{r}) = \frac{k}{\pi} \|\underline{v}\| \, \underline{u}'_{\underline{v}} \underline{a} = \frac{2\|\underline{v}\|}{\lambda} \|\underline{a}\| \, \underline{u}'_{\underline{v}} \underline{u}_{\underline{a}}. \tag{73}$$

Equation (73) reveals the well-known Doppler bandwidth, for which the resolution is calculated through $\Delta'_D = \|\underline{v}\|/|B_D|$.

From (71) it is evident that B_D and S_D are only identical if $\underline{u}'_{\underline{v}} \underline{u}_{\underline{a}} = 1$. These two vectors are only collinear for a special symmetric geometry, namely a strictly side-looking SAR.

4.2.1 Special cases

To gain deeper insight into the ramifications of (71), it is helpful to look at some special cases of bistatic geometry.

4.2.1.1 Monostatic with omnidirectional antenna pattern

In the monostatic case when the two direction vectors $\underline{u}_1$ and $\underline{u}_2$ are identical, i.e., $\underline{u} = \underline{u}_1 = \underline{u}_2$. An omnidirectional antenna diagram results in a theoretically unlimited observation time of the ground point $\underline{r}$, i.e., $t_{\min,\max} = \mp\infty$ with

$$\begin{aligned} \lim_{t \to \pm\infty} \underline{u}(t, \underline{r}) &= \lim_{t \to \pm\infty} \frac{(\underline{R}_{0,1} - \underline{r}) + \underline{v}t}{\sqrt{\|\underline{R}_{0,1} - \underline{r}\|^2 + 2\underline{v}'(\underline{R}_{0,1} - \underline{r})t + \|\underline{v}\|^2 t^2}} \\ &= \pm \frac{\underline{v}}{\|\underline{v}\|} = \pm \underline{u}_v. \end{aligned} \tag{74}$$

As expected, the unit direction vector converges to the unit velocity vector for infinite time. Hence, inserting (74) in (71) leads to

$$\Delta_D = \frac{\lambda}{2\|\underline{u}(\infty, \underline{r}) - \underline{u}(-\infty, \underline{r})\|} = \frac{\lambda}{2\|2\underline{u}_v\|} = \frac{\lambda}{4}, \tag{75}$$

the well known maximal Doppler resolution of a quarter-wavelength, independent of the scatterer location.

4.2.1.2 Monostatic stripmap with realistic antenna pattern

The maximum observation time for a monostatic geometry is given as the period of time between entering and leaving the mainbeam during the overflight. These times are

$$t_{\min,\max} = \mp \frac{\theta_{3\text{dB}}}{2} \frac{\|\underline{R}_0 - \underline{r}\|}{\|\underline{v}\|}, \tag{76}$$

which in turn yields

$$\underline{u}(t_{\max},\underline{r}) - \underline{u}(t_{\min},\underline{r}) = \frac{\theta_{3\mathrm{dB}}}{2}\frac{\underline{v}}{\|\underline{v}\|} \left(\frac{1}{\sqrt{1+\frac{(\underline{R}_0-\underline{r})'\underline{v}}{\|\underline{v}\|\,\|\underline{R}_0-\underline{r}\|}\theta_{3\mathrm{dB}}+\frac{\theta_{3\mathrm{dB}}^2}{4}}} + \frac{1}{\sqrt{1+\frac{(\underline{R}_0-\underline{r})'\underline{v}}{\|\underline{v}\|\,\|\underline{R}_0-\underline{r}\|}\theta_{3\mathrm{dB}}-\frac{\theta_{3\mathrm{dB}}^2}{4}}} \right). \tag{77}$$

For a non-squinted (or slightly squinted) geometry with $\underline{u}_{\underline{R}_0-\underline{r}} \perp \underline{v}$, the difference in (77) can be approximated as $\underline{u}(t_{\max},\underline{r}) - \underline{u}(t_{\min},\underline{r}) \approx \theta_{3\mathrm{dB}}\underline{v}/\|\underline{v}\|$, which results in the well known range-independent (azimuth) resolution

$$\Delta_D = \frac{\lambda}{\|2\underline{u}_v\,\theta_{3\mathrm{dB}}\|} = \frac{A}{2}, \tag{78}$$

where $A = \lambda/\theta_{3\mathrm{dB}}$ denotes the real aperture of the monostatic antenna.

4.2.1.3 Bistatic with omnidirectional antenna pattern

Analogous to (74), the individual direction vectors are $\underline{u}_i(\infty,\underline{r}) - \underline{u}_i(-\infty,\underline{r}) = 2\underline{u}_{v_i}$, which inserted into (71) leads to

$$\Delta_D = \frac{\lambda}{2\|\underline{u}_{v_1}+\underline{u}_{v_2}\|} = \frac{\lambda}{4\sqrt{1+\cos\alpha}}, \tag{79}$$

where α denotes the angle between the two velocity vectors. It is apparent that the bistatic Doppler resolution is always lower than that of the monostatic case, except when the two platform fly exactly parallel. In contrast, the resolution goes to infinity when the two platforms fly anti-parallel, i.e., $\cos\alpha = -1$, because the aspect angle variation/spread for each platform cancels out exactly.

4.2.1.4 Bistatic stripmap with realistic antenna pattern

Let us assume that the maximum bistatic observation time is exclusively determined by one of the platforms, e.g., by the transmitter:

$$t_{\min,\max} \equiv t_{\min,1,\max,1} = \mp\frac{\theta_1}{2}\frac{\|\underline{R}_{0,1}-\underline{r}\|}{\|\underline{v}_1\|}, \tag{80}$$

where for simplicity of notation the subscript '3dB' for the transmitter beamwidth has been omitted. This assumption is not restrictive. In contrast, it would always be fulfilled in cases of high-flying (maybe orbiting) illuminators and relatively low flying receivers with $\|\underline{R}_{0,1}-\underline{r}\| \gg \|\underline{R}_{0,2}-\underline{r}\|$. In order to keep the PRF reasonably small, i.e., to avoid range ambiguities while maintaining a sufficient swathwidth,

high altitude SARs need to be equipped with rather large antennas, which means $\theta_1 \ll \theta_2$. Analogous to (77), the direction vector difference for the transmitter is given as

$$\underline{u}_1(t_{\max,1}, \underline{r}) - \underline{u}_1(t_{\min,1}, \underline{r}) \approx \theta_1 \frac{\underline{v}_1}{\|\underline{v}_1\|}, \tag{81}$$

whereas that of the receiver is

$$\underline{u}_2(t_{\max,1}, \underline{r}) - \underline{u}_2(t_{\min,1}, \underline{r}) = \tag{82}$$
$$\frac{\theta_1}{2} \frac{\|\underline{R}_{0,1} - \underline{r}\|}{\|\underline{v}_1\|} \underline{v}_2 \left(\frac{2}{\sqrt{1 + \frac{\|\underline{R}_{0,1} - \underline{r}\|^2 \, \|\underline{v}_2\|^2}{\|\underline{R}_{0,2} - \underline{r}\|^2 \, \|\underline{v}_1\|^2} \frac{\theta_1^2}{4}}} \right) \approx \theta_1 \frac{\|\underline{R}_{0,1} - \underline{r}\|}{\|\underline{v}_1\|} \underline{v}_2,$$

where it has been assumed that both radars work in quasi-stripmap mode with $\underline{R}'_{0,i} \underline{v}_i \ll 1$. Inserting (81) and (82) into (70) yields

$$B_D = \frac{\theta_1}{\lambda \|\underline{v}_1\|} \sqrt{\frac{\|\underline{R}_{0,1} - \underline{r}\|^2}{\|\underline{R}_{0,2} - \underline{r}\|^2} \|\underline{v}_2\|^2 + 2 \frac{\|\underline{R}_{0,1} - \underline{r}\|}{\|\underline{R}_{0,2} - \underline{r}\|} \underline{v}'_1 \underline{v}_2 + \|\underline{v}_1\|^2}. \tag{83}$$

For two special flight geometries this term can be further simplified. If the two platforms fly exactly perpendicular to each other, i.e., $\underline{v}'_1 \underline{v}_2 = 0$, the Doppler resolution as the inverse of (83) becomes

$$\Delta_D^{\perp} = A_1 \left(\sqrt{1 + \frac{\|\underline{R}_{0,1} - \underline{r}\|^2 \, \|\underline{v}_2\|^2}{\|\underline{R}_{0,2} - \underline{r}\|^2 \, \|\underline{v}_1\|^2}} \right)^{-1}, \tag{84}$$

and in case they both fly parallel or anti-parallel, i.e., $\underline{v}'_1 \underline{v}_2 = \pm \|\underline{v}_1\| \, \|\underline{v}_2\|$ it becomes

$$\Delta_D^{\parallel} = \operatorname{sign} \left(1 \pm \frac{\|\underline{R}_{0,1} - \underline{r}\| \, \|\underline{v}_2\|}{\|\underline{R}_{0,2} - \underline{r}\| \, \|\underline{v}_1\|} \right) \frac{A_1}{1 \pm \frac{\|\underline{R}_{0,1} - \underline{r}\| \, \|\underline{v}_2\|}{\|\underline{R}_{0,2} - \underline{r}\| \, \|\underline{v}_1\|}}, \tag{85}$$

where $A_1 = \lambda / \theta_1$ denotes the real aperture of the transmitter. In (85) it is interesting to note that the Doppler resolution will be better than that of a monostatic SAR on the transmitter platform when the ratio between distances and the speeds of the two platforms are chosen appropriately, e.g., $\|\underline{R}_{0,1} - \underline{r}\| / \|\underline{v}_1\| > \|\underline{R}_{0,2} - \underline{r}\| / \|\underline{v}_2\|$. The physical reason behind this is that the combined aspect angle variation/spread of high flying illuminator and low-flying receiver can be larger compared to that of a high-flying monostatic system. In [36], this result was derived on a multi-page analysis via the width of the actual point spread function.

Fig. 12 shows the expected bistatic observation time and the corresponding Doppler resolution for the bistatic airborne scenario listed in Table 6. One can recognize that the bistatic observation time is non-symmetrically distributed along the 'bistatically illuminated' area. It is clear that the Doppler resolution will be worse for areas where the observation time is small, such at the edges.

Table 6: *Bistatic airborne-airborne configuration*

Parameter	Transmitter	Receiver
Altitude	$H_1 = 7000$ m	$H_2 = 15,000$ m
Velocity	$\underline{v}_1 = 130\,\underline{u}_x$ m/s	$\underline{v}_2 = 220$ m/s
Course angle	$\Psi_{ps,1} = 0°$	$\Psi_{ps,2} = 45°$
Elevation angle to scene centre at $t = 0$	$\Phi_{0,1} = 45°$	$\Phi_{0,2} = 35°$
Squint angles to scene centre at $t = 0$	$\Psi_{0,1} = 0°$	$\Psi_{0,2} = 90°$
Antenna pattern	sinc	sinc
Azimuth beamwidth	$u_{3\text{dB},1} = 3°$	$u_{3\text{dB},2} = 3°$
Elevation beamwidth	$v_{3\text{dB},1} = 20°$	$v_{3\text{dB},2} = 20°$
Wavelength	$\lambda = 0.0565$ m	
Pulse bandwidth	$B = 50$ MHz	
Sampling frequency	$f_s = 50$ MHz	
Pulse Length	$T = 5\mu$s	
PRF	680 Hz	

4.2.1.5 Bistatic stripmap with realistic antenna pattern and stationary receiver

From equations (83) to (85), it is evident that the Doppler resolution for a stationary receiver with $\underline{v}_2 = \underline{0}$ is identical to the real aperture of the transmitter, independent of the location on the ground:

$$\Delta_D^{\bar{\wedge}} = A_1, \tag{86}$$

where $\bar{\wedge}$ symbolises the moving transmitter and the stationary receiver. This value is exactly one-half of the maximum value for a conventional monostatic stripmap SAR. Of course, the bistatic Doppler resolution can always be enhanced by pointing the antenna beam on the same spot on the ground (spotmode) during the flight, and thereby increasing the bistatic observation time, and in turn, the extent of the k-space. In contrast, increasing the beamwidth of the stationary receiver antenna will not enhance the Doppler resolution because the k-space spread is exclusively determined by the moving transmitter. However, a larger receiver beamwidth will increase the imageable area on the ground.

The resolution for the airborne-tower scenario introduced in Tables 4 and 5 is determined by the transmitter azimuthal beamwidth $\Delta_D^{\bar{\wedge}} = \lambda / u_{3\text{dB},1} = 0.4516$ m. Since the Doppler resolution for a stationary receiver is constant inside the bistatically illuminated region, it is not explicitly plotted.

It is important to note that the Doppler gradient (67) is only varying slightly over

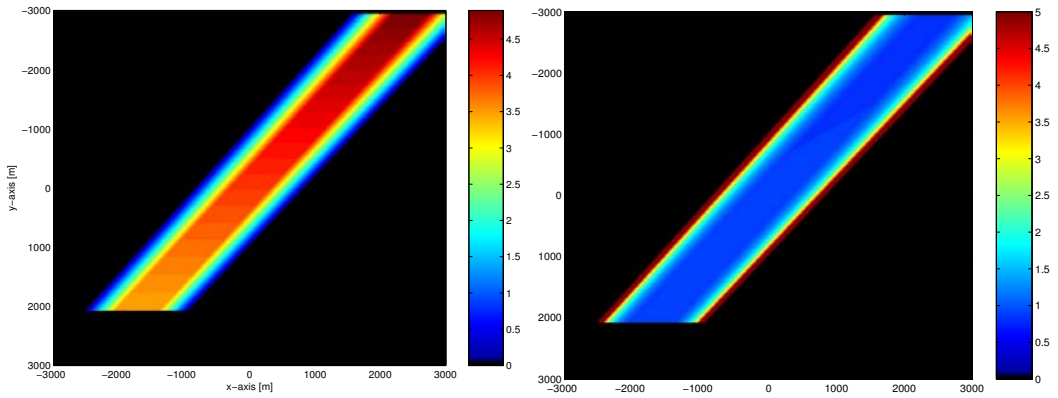

(a) Bistatic observation time in seconds. (b) Doppler resolution in meters.

Figure 12: *Bistatic observation time and ground Doppler resolution for the airborne transmitter and airborne receiver configuration listed in Table 6.*

time in many practical cases, such as side-looking or slightly squinted SAR modes. In such cases, $\underline{\dot{k}}$ can be treated as constant over time and can be taken out of the integral in (70), i.e.,

$$B_D \approx \frac{T_b}{\lambda} \left\| \underline{\dot{u}}_1(0,\underline{r}) + \underline{\dot{u}}_2(0,\underline{r}) \right\|, \tag{87}$$

where $T_b = t_{\max} - t_{\min}$ is the bistatic observation time. Replacing $\underline{\dot{u}}_i(0,\underline{r})$ with the the projections (68) at the time origin yields

$$\begin{aligned} B_D &\approx \frac{T_b}{\lambda} \left\| \frac{1}{\|\underline{R}_{0,1} - \underline{r}\|} \mathbf{P}^{\perp}_{\underline{R}_1}(0,\underline{r})\underline{v}_1 + \frac{1}{\|\underline{R}_{0,2} - \underline{r}\|} \mathbf{P}^{\perp}_{\underline{R}_2}(0,\underline{r})\underline{v}_2 \right\| \\ &= \frac{T_b}{\lambda} \left\| \frac{\left(\mathbf{I} - \underline{u}_1(0,\underline{r})\underline{u}_1'(0,\underline{r})\right)\underline{v}_1}{\|\underline{R}_{0,1} - \underline{r}\|} + \frac{\left(\mathbf{I} - \underline{u}_2(0,\underline{r})\underline{u}_2'(0,\underline{r})\right)\underline{v}_2}{\|\underline{R}_{0,2} - \underline{r}\|} \right\|, \end{aligned} \tag{88}$$

which is identical to the result originally introduced by Cardillo [34], and later in [37]. For only slightly squinted geometries where $\underline{u}_i'(0,\underline{r})\underline{u}_{\underline{v}_i} \approx 0$, it is easy to show that identical results as those for the previous special cases (shown above) can be achieved. However, (71) represents the exact solution for any SAR mode and geometry, and should, therefore, be preferred.

4.2.2 Ground plane

In most cases one is interested in the resolution on the ground plane, i.e., on the separability of two closely located points on Earth's surface. In order to accommodate this, the generally three-dimensional Doppler gradient vector can, for instance, be projected onto the flat ground plane. In other words, the maximum change of

Doppler on the ground is along the projection of the gradient onto the ground. Applying the constant projection matrix

$$\mathbf{P}^{\perp}_{\underline{z}_s} = (\mathbf{I} - \underline{z}_s \underline{z}_s') = \begin{pmatrix} 1 & 0 & 0 \\ 0 & 1 & 0 \\ 0 & 0 & 0 \end{pmatrix} \tag{89}$$

to the Doppler gradient in (67)

$$\underline{\nabla}^{(g)} \omega_D(t, \underline{r}) = \mathbf{P}^{\perp}_{\underline{z}_s} \, \underline{\nabla} \omega_D(t, \underline{r}) \tag{90}$$

and following the analysis form (69) to (71), yields the ground resolution of

$$\Delta_D^{(g)}(\underline{r}) = \frac{\lambda}{\left\| \mathbf{P}^{\perp}_{\underline{z}_s} \Big(\underline{u}_1(t_{\max}, \underline{r}) - \underline{u}_1(t_{\min}, \underline{r}) + \underline{u}_2(t_{\max}, \underline{r}) - \underline{u}_2(t_{\min}, \underline{r}) \Big) \right\|}. \tag{91}$$

4.3 Range-resolution

The idea of using the gradient to determine the bistatic resolution can also be applied in the fast-time direction. Although there is no perspicuous range direction in bistatic geometry, it is convenient to keep using this term. According to (1) and (3), the total travel time τ of the transmitted pulse to a scatterer on the ground (located at $\underline{r}$) and further to the receiver is given by

$$\tau(t, \underline{r}) = \frac{1}{c} \big(\, \|\underline{R}_1(t, \underline{r})\| + \|\underline{R}_2(t, \underline{r})\| \, \big), \tag{92}$$

where c denotes the speed of light. The gradient

$$\underline{\nabla} \tau(t, \underline{r}) = \frac{1}{c} \big(\underline{u}_1(t, \underline{r}) + \underline{u}_2(t, \underline{r}) \big) \tag{93}$$

represents the direction and size of the maximum change of travel time. Although the travel time is strictly speaking dependent on time (varying position of the radars), the change of the gradient over the entire aperture time is typically small, so that it can be neglected in all practical cases. Hence, it is sufficient to analyse the gradient only at the time origin, i.e., we define two nearby points to be resolved in range as long as they are separable at $t = 0$. For a monostatic system, for instance, this means that echoes of two closely spaced scatterers are located in different range cells along the entire synthetic aperture in the raw data matrix.

Since the receiver measures different arrival times proportional to the system bandwidth B, i.e., in a raster of spacing $\delta t = 1/B$, the range resolution can be written as

$$\Delta_R(\underline{r}) = \frac{1/B}{\|\underline{\nabla} \tau(0, \underline{r})\|} = \frac{c}{B \, \|\underline{u}_1(0, \underline{r}) + \underline{u}_2(0, \underline{r})\|}, \tag{94}$$

where $\underline{u}_i(0,\underline{r}) \equiv \underline{u}_{0,i} = (\underline{R}_{0,i} - \underline{r})/\|\underline{R}_{0,i} - \underline{r}\|$.

Equating the two directional unit vectors in (94) confirms the well known constant slant-range resolution of $\Delta_R(\underline{r}) = c/(2B)$ for a monostatic scenario. In the bistatic case (94) can be re-written as

$$\Delta_R(\underline{r}) = \frac{c}{\sqrt{2}B}\frac{1}{\sqrt{1+\cos\alpha(\underline{r})}} \tag{95}$$

where $\alpha(\underline{r})$ denotes the angle between the range vectors from the point $\underline{r}$ on the ground to the receiver and transmitter, respectively.

4.3.1 Ground plane

Analogously to (90), the gradient vector (93) must be projected onto the two-dimensional ground plane in order to evaluate the ground range resolution on the flat Earth's surface. Therefore, applying the projection (89) to the gradient vector yields the general form of the bistatic range resolution

$$\Delta_R^{(g)}(\underline{r}) = \frac{1/B}{\|\underline{\nabla}^{(g)}\tau(0,\underline{r})\|} = \frac{1/B}{\|\mathbf{P}^{\perp}_{\underline{z}_s}\underline{\nabla}\tau(0,\underline{r})\|} = \frac{c/B}{\|\mathbf{P}^{\perp}_{\underline{z}_s}\underline{u}_{0,1}(\underline{r}) + \mathbf{P}^{\perp}_{\underline{z}_s}\underline{u}_{0,2}(\underline{r})\|}. \tag{96}$$

Figure 13 shows the ground range resolution over varying bistatic angles for the airborne transmitter and tower receiver geometry used previously, see Tables 4 and 5. The loss in range resolution for less favourable geometries becomes evident, especially for the area around the line connecting the receiver and the transmitter. Here, the resolution decreases drastically from roughly 30 cm to 40 m. However, reasonable imaging (in the meter-range resolution) should be possible for pixels further away from this line, even for a forward-scattering geometry .

4.3.2 Equivalent bistatic nadir hole

From (96), it is evident that the 'bistatic nadir hole' is given at the location on the ground $\underline{r}$ at which the norm of the travel-time gradient vanishes. Around this location, the ground range resolution tends to infinity, i.e., meaningful imaging is impossible. Re-writing the projection matric in (89) as $\mathbf{P}^{\perp}_{\underline{z}_s} = \underline{x}_s\underline{x}'_s + \underline{y}_s\underline{y}'_s$, we get

$$\underline{\nabla}\tau^{(g)}(\underline{r}) = \frac{1}{c}\Big(\underline{x}'_s\underline{u}_{0,1}(\underline{r}) + \underline{x}'_s\underline{u}_{0,2}(\underline{r})\Big)\underline{x}_s + \frac{1}{c}\Big(\underline{y}'_s\underline{u}_{0,1}(\underline{r}) + \underline{y}'_s\underline{u}_{0,2}(\underline{r})\Big)\underline{y}_s. \tag{97}$$

In order for the norm of (97) to be zero, both components must satisfy

$$\begin{aligned} \underline{x}'_s\Big(\underline{u}_{0,1}(\underline{r}_0) + \underline{u}_{0,2}(\underline{r}_0)\Big) &= 0 \\ \underline{y}'_s\Big(\underline{u}_{0,1}(\underline{r}_0) + \underline{u}_{0,2}(\underline{r}_0)\Big) &= 0, \end{aligned} \tag{98}$$

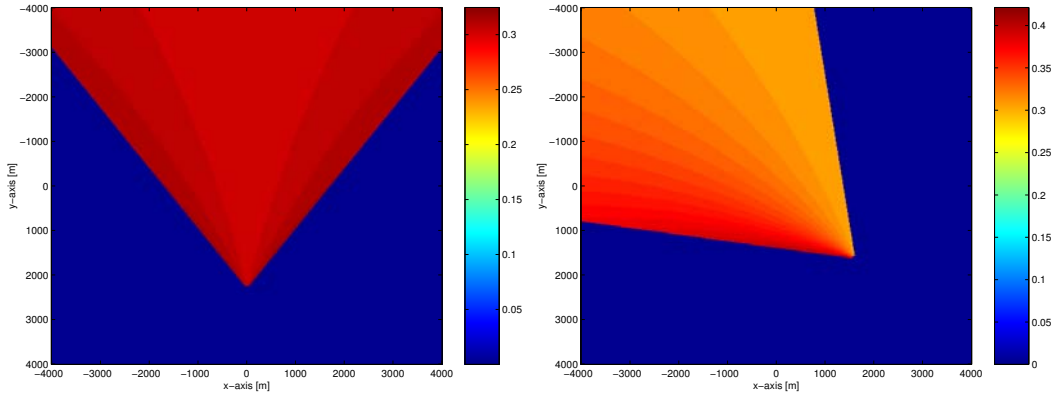

(a) Quasi-monostatic geometry, bistatic angle = 0 degrees.

(b) Bistatic angle = $45°$.

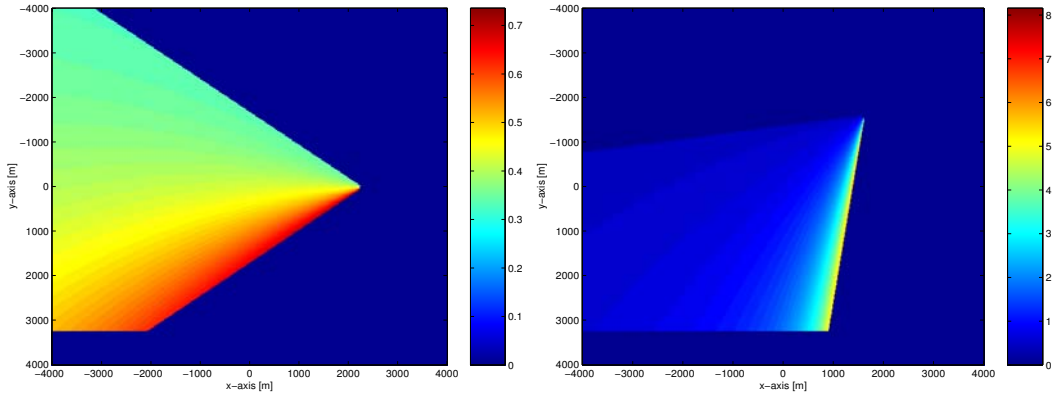

(c) Bistatic angle = $90°$.

(d) Bistatic angle = $135°$.

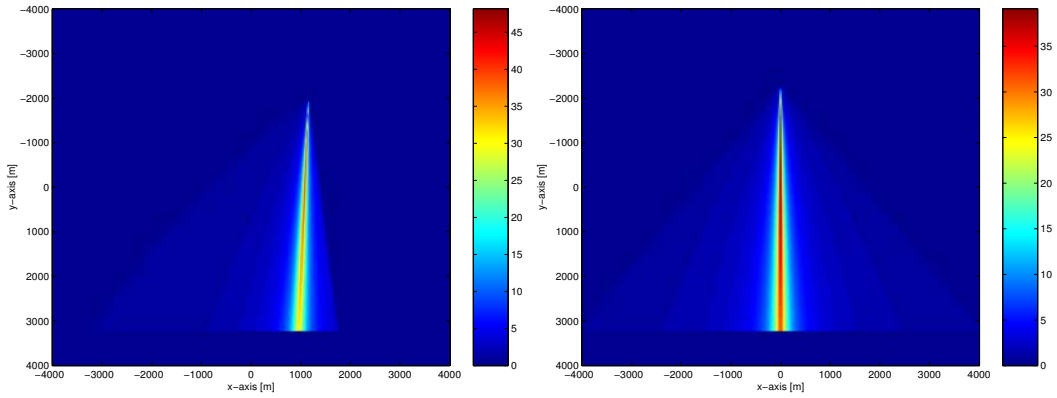

(e) Bistatic angle = $150°$.

(f) Forward-looking geometry, bistatic angle = $180°$.

Figure 13: *Ground range resolution in meters for a stationary receiver and an airborne transmitter with varying bistatic angles $\Phi_{0,2}$.*

i.e., must simultaneously vanish at $\underline{r}_0$. In other words, the vector given as the sum of the two unit vectors pointing from the location $\underline{r}_0$ to either radar must be perpendicular to the ground plane, i.e., $\underline{u}_{0,1}(\underline{r}_0) + \underline{u}_{0,2}(\underline{r}_0) \perp \underline{x}_s, \underline{y}_s$.

In monostatic SAR, where $\underline{u}_{0,1}(\underline{r}) = \underline{u}_{0,2}(\underline{r})$, this is true for $\underline{r}_0$ directly beneath the radar platform, which is typically not illuminated by the antenna pattern. In bistatic SAR, however, the equivalent nadir may shift into the viewable/imaged area depending on the bistatic geometry, e.g., $\|\underline{R}_{0,1} \gg \underline{R}_{0,2}\|$, as shown in Fig. 14.

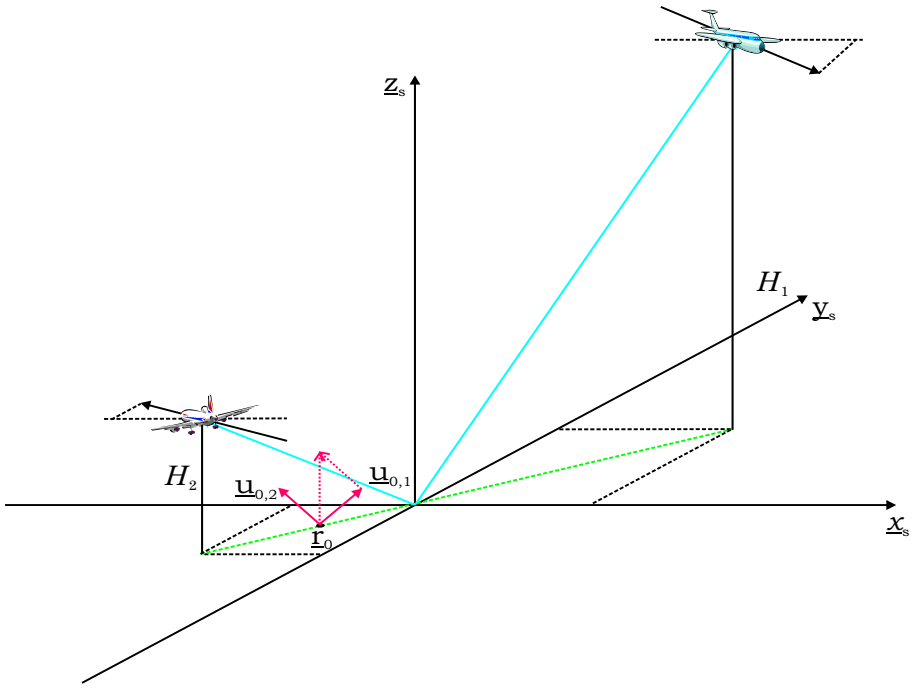

Figure 14 : *Illustration of the equivalent bistatic nadir hole at* $r = r_0$.

5 Bistatic SAR raw data simulation

To develop and test techniques and algorithms to process bistatic SAR data, it is essential to investigate and compare their fidelity and quality on simulated data, i.e., raw data sets obtained under ideal conditions. The developed and implemented point target simulator comprises all necessary components to be realistic: 3D-platform geometry and motion vectors, point target location and reflectivity, imaging geometry (such as distances between illuminator-target-receiver and coordinate transformations) as well as antenna pattern and variable pointing.

In a first step, an airborne bistatic SAR simulator with constant velocities and altitudes and a flat Earth assumption has been developed and coded in MATLAB. The simulated SAR configurations comprise the simple stripmap mode as well as more sophisticated modes where the antenna is continuously steered onto the scene center during the flight (spotmode, sliding stripmode, etc.). All required coordinate systems and angular transformations are defined in appendices D and E. The user inputs are the basic radar system parameters: wavelength λ, pulse bandwidth B, sampling frequency f_s, pulse Length T, and the pulse repetition frequency PRF, as well as the transmitter and receiver parameters at the time origin listed in Tables 4 and 5.

In order to determine the maximum raw data field size in the Doppler direction, the maximum observation time $T_{b,\max}$ is calculated via (59) for each pixel within a pre-specified area on the ground. The maximum field size in the range direction is determined by the longest and shortest distance to any pixel. Half a chirp-length $BT/2$ is added on either side of the raw data field to prevent focussing errors at the edges of the specified regions. The pre-specified region on the ground can now be sparsely filled with P scatterer points, where each point is characterised by its x_s, y_s-location and its backscatter amplitude (radar cross section (RCS)). As reference, the bistatic distance to the center of the scene at the time origin is calculated as $\|R_0\| = \|R_{0,1}\| + \|R_{0,2}\|$.

The actual raw data generation is now executed in a straightforward fashion, namely, via the superposition of each point target echo at each pulse transmission time (position). Instead of summing the reflected echoes in the time domain, it is computationally more efficiently performed in the Fourier-domain. Here the time delay, which requires interpolation, corresponds to a multiplication with a linear frequency ramp. To achieve this, the ideal transmit pulse in baseband, (2),

$$s(n_s) = \exp\left(j\pi \frac{B}{T}\left(\frac{n_s}{f_s}\right)^2\right) \qquad \text{for} \qquad n_s = -N_s/2, \ldots, N_s/2, \tag{99}$$

and $N_s = \mathrm{fix}(BT)$ is transformed into the frequency domain $S(m_s) = \mathcal{F}\big(s(n_s)\big)$.

For each pulse index n_p the range vectors $\underline{R}_i(n_p/\mathrm{PRF}, \underline{r})$ from either platform to the particular scatterer are computed via (1). Transforming these vectors into the antenna coordinate system with (E.8), i.e., by application of $\mathbf{L}_{ap}(\Phi_{0,i}, \Psi_{0,i})\mathbf{L}_{ps}(\Psi_{p,i})$ and using equations F.3, yields the required aspect and elevation angles to this scatterer. These angles are then used to calculate the antenna pattern weighting. The delay time $\tau(n_p, \underline{r})$ from transmitter to the scatterer located at $\underline{r}$ and to the receiver is given as

$$\tau(n_p, \underline{r}) = \frac{\|\underline{R}_1(n_p/\mathrm{PRF}, \underline{r})\| + \|\underline{R}_2(n_p/\mathrm{PRF}, \underline{r})\| - \|\underline{R}_0\|}{c} \tag{100}$$

where c denotes the speed of light. The phase multiplication

$$S(m_s) \cdot \exp\Big(- j2\pi f(m_s)\tau(n_p)\Big), \tag{101}$$

where $f(m_s)$ denotes a frequency bin in the RF domain, includes on one hand the range cell migration for longer synthetic aperture times, and on the other hand, also applies the Doppler induced phase history. Weighting with the antenna pattern, adding up the returns from all scatterers and applying the inverse Fourier-transform to the result, leads to the desired raw data signal for the particular pulse index. This procedure must be repeated for all pulses.

Figure 15 (a) shows the real part of simulated bistatic SAR raw data for a stationary receiver scenario. In order to keep the raw data field size reasonably small, a C-band transmitter was chosen; the system parameters in Table 7 are similar to those of the Environment Canada Convair-580 aircraft [38]. Since the illumination pattern is not symmetric on the ground for this perpendicular configuration, see Fig. 11, the slow time origin does not occur at the center of the x-axis. In the real part of the raw data, typical Fresnel-rings are visible representing 'height contours' of the two-dimensional chirp function. Further, the 'sinc'-antenna pattern weighting in the Doppler direction can be recognized in the the magnitude plot, Fig. 15 (b), as well as the range migration of the echo-pulse through various range cells.

Currently, a spaceborne version of a bistatic SAR simulator is under development. It is based on a fixed, Earth-centered, coordinate system and, in its final extension will use an orbit propagator software module to determine the satellite's state vectors at each pulse transmission time. The scatterers are placed onto the curved Earth surface and the Earth's rotation will be taken into account.

Table 7: *Simulation parameters.*

Parameter	Transmitter	Receiver
Altitude	$H_1 = 6900$ m	$H_2 = 20$ m
Velocity	$\underline{v}_1 = 132\,\underline{u}_x$ m/s	$\underline{v}_1 = 0$
Elevation angle to scene centre at $t = 0$	$\Phi_{0,1} = 45°$	$\Phi_{0,2} = 5°$
Squint angle to scene centre at $t = 0$	$\Psi_{0,1} = 0°$	$\Psi_{0,2} = 90°$
Antenna pattern	sinc	sinc
Azimuth beamwidth	$u_{3\text{dB},1} = 3°$	$u_{3\text{dB},2} = 30°$
Elevation beamwidth	$v_{3\text{dB},1} = 20°$	$v_{3\text{dB},2} = 20°$
Wavelength	$\lambda = 0.0565$ m	
Pulse bandwidth	$B = 50$ MHz	
Sampling frequency	$f_s = 50$ MHz	
Pulse Length	$T = 5\mu$s	
PRF	680 Hz	

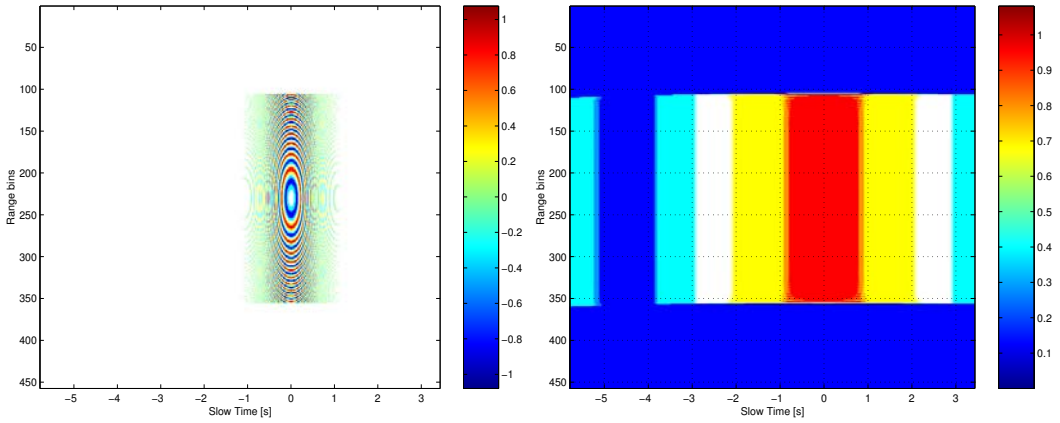

(a) Real part. (b) Magnitude.

Figure 15: *Real part and magnitude of simulated bistatic raw data for an airborne transmitter and stationary receiver configuration, $\Psi_{0,2} = 90°$.*

6 Bistatic clutter experiments

As part of the TTRDP (Trilateral Technical Research & Development Program) investigation of bistatic clutter, the MTI experiments team conducted a bistatic clutter characterization data collection campaign in the summer and fall of 2002. The first sets of experiments included the so-called Rooftop test, with RADARSAT-1 as transmitter and the AFRL (US Air Force Rome Laboratory) multi-channel C-Band radar as stationary receiver, see the left image in Fig. 16. The receiver antenna consists of five separate channels that allow simultaneous reception of different signals in parallel. One channel is designated for recording the direct path signal from the satellite during the overpass. The right image in Fig. 16 shows part of the planar antenna array as well as the additional direct path receiver horn pointing upwards. Since this horn antenna possesses a wide beam, it does not require an adaptive azimuth steering capability and it is sufficient to tilt it to a constant elevation angle according to the flight path of the transmitter, specifically the predicted orbit of RADARSAT-1. While channel one records the reflected signal from the ground that

(a) Rooftop-tower.

(b) C-band array and direct path receiver horn.

Figure 16: *Stationary bistatic receiver antenna at AFRL in Rome, NY.*

is received over the entire array aperture, channels three-to-five are measuring the echoes over different subapertures or subarrays. Channel two samples and records the direct path signal. The array is rectangular, 3.5 m in width and 1.2 m in height: each of its eight sub-arrays is 0.45 m wide.

6.1 RADARSAT-1 as illuminator

During a RADARSAT-1 bistatic clutter characterization measurement campaign on January, 28, 2002, several Gbyte of data were collected. A detailed data description and preliminary data analysis were reported in [39]. The basic system parameters for this trial are listed in Table 8, and the principle bistatic SAR geometry is depicted in Fig. 17 (not to scale). While the satellite is flying on an ascending polar

Table 8: *System parameters for the bistatic clutter trial of 28 January 2002.*

Wavelength	$\lambda = 0.565$ m
Pulse bandwidth	$B = 11.56$ MHz
Pulse Length	$T = 42\mu$s
PRF	1289 Hz
Sampling frequency	$f_s = 80$ MHz
Intermediate frequency	$f_{\mathrm{IF}} = 20$ MHz

orbit, i.e., nearly directly towards North, it is illuminating to the right. The stationary receiving antenna with its relatively narrow beamwidth $\theta_{3\mathrm{dB}} = 1^\circ$ is pointing south-west towards the town of Stockbridge.

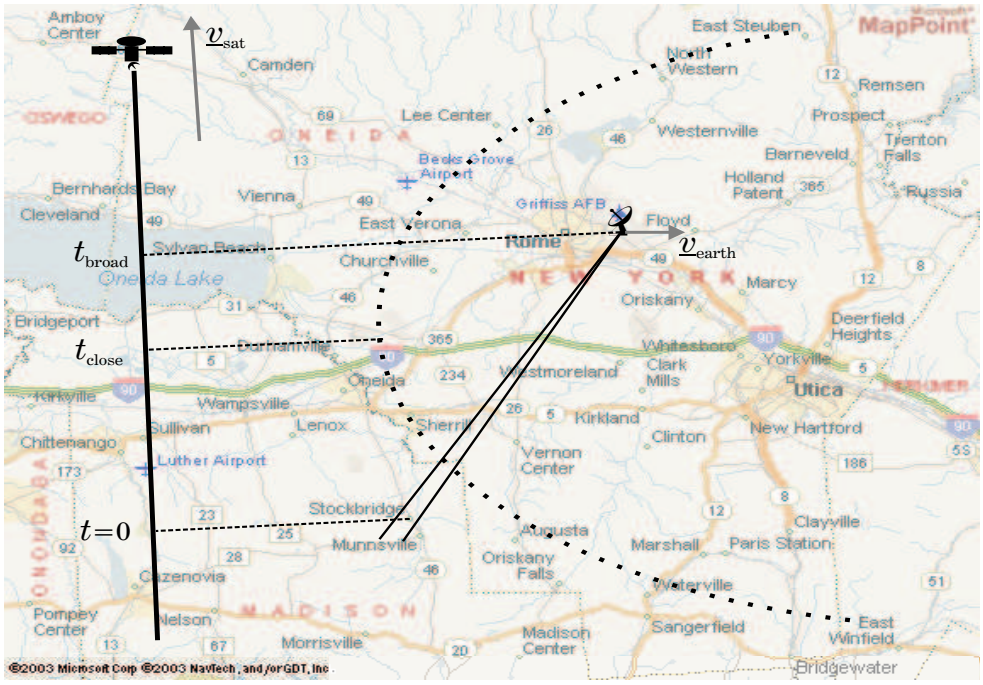

Figure 17 : *Bistatic geometry for the trial at Rome, NY on 28 Jan. 2002. The underlying map (≈ 60 km x 70 km) was generated by MapPoint ©2003 Microsoft Corp., ©2003 NavTech and GDT, Inc.*

Since the Earth is rotating eastwards[2], the point of closest approach between the antenna and the satellite t_c will not occur at broadside t_b. The time of closest approach is at the apex of the range parabola, as illustrated in Fig. 17, cf. [40]. The

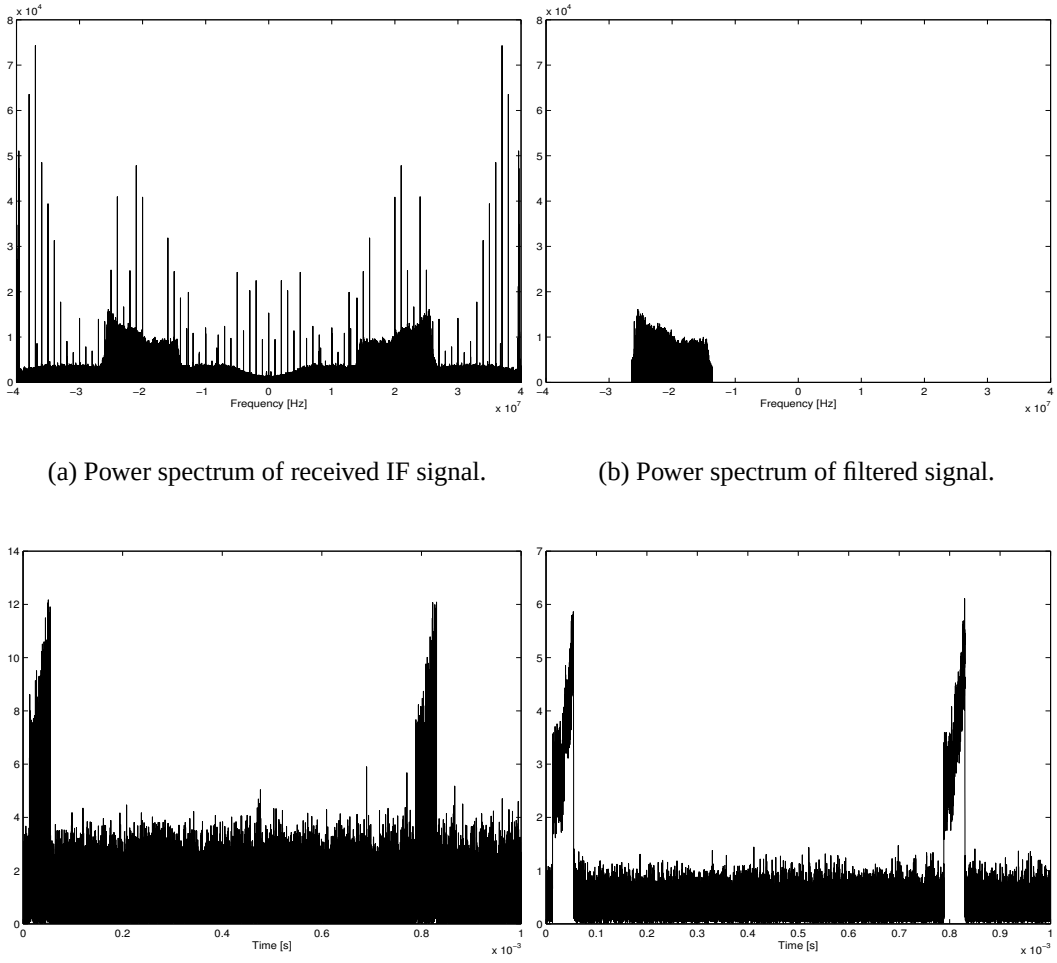

(a) Power spectrum of received IF signal.

(b) Power spectrum of filtered signal.

(c) Magnitude of received signal.

(d) Magnitude of filtered signal.

Figure 18: *SNR enhancement via spectral filtering in IF.*

recorded data stream consists of the sampled real-valued echo signals plus a superimposed 1 MHz calibration tone. Figure 18 (a) shows the spectrum of part of the signal after rejection of the calibration tone with an ideal notch filter. The roughly 12 MHz wide transmit pulses can clearly be recognized around the Intermediate Frequency (IF) of 20 MHz. Also visible are discrete interference spikes. While the low-frequency components are believed to be caused by the power supply, the high-frequency spikes are the unwanted higher order harmonics of the calibration tone.

[2]The velocity at the Rooftop receiver latitude is approximately 340 m/s.

In Fig. 18 (c), a small portion of the corresponding time signal is plotted showing two pulses which are one PRI apart. The low SNR, typical for space-based systems, is apparent, i.e., the background noise is relatively high. The spectral blanking of everything but the pulse bandwidth on the negative side of the spectrum, see Fig. 18 (b), results in a significantly increased SNR; the pulses are completely above the background noise floor in Fig. 18 (d).

After spectral shift and inverse Fourier transform of the one-sided spectrum in Fig. 18 (b), the IQ-demodulated signal in baseband is apparent, with Fig. 19 (a) showing a close-up of the magnitude and phase of one received pulse. The nominal transmit pulse length of $T = 42\mu$s and the Linear Frequency (LF) modulation (parabolic phase) are evident.

The data were then range compressed. This was performed by convolution with the conjugate complex of the expected theoretical signal

$$s(t) = \exp\left(j\pi\frac{B}{T}t^2\right)\ \mathrm{rect}\left(\frac{t}{T}\right), \tag{102}$$

using the nominal values for bandwidth B and pulse length T. The result for one particular pulse from the end of the data stream is plotted in blue in Fig. 19 (b). Although the resolution, i.e., the 3dB width of the impulse response, is close to

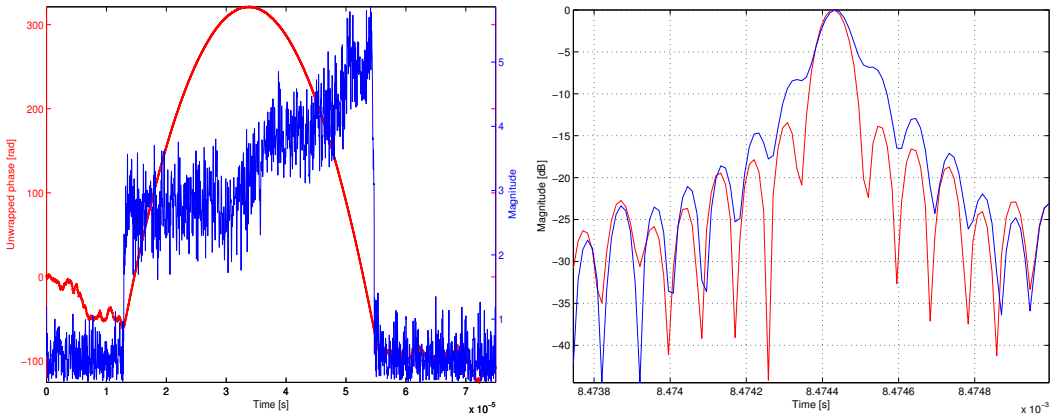

(a) Magnitude and phase of pulse.

(b) Compressed pulse, (blue) theoretical filter, (red) matched filter.

Figure 19: *Compressed pulse sidelobe reduction via matched filter.*

the expected value, the first sidelobes are very high. It is well known that much better performance can be achieved by using an exact matched filter, i.e., a measured replica of the transmitted pulse itself. However, since such a replica was not

available, one of the first pulses was extracted and used to compress all the subsequent pulses. The red curve in Fig. 19 (b) represents one compressed pulse several seconds (or several thousands pulses) later. The improvement in compression is apparent, particularly since the first sidelobes approach almost perfectly the theoretical value of -13 dB below the main peak. In addition, it is confirmed that the pulse properties are stable over this time frame, which is well known from other experimental SAR systems.

Figure 20 (a) shows the magnitudes and the Doppler frequencies (phase differences) of all range-compressed peaks of the direct path signal as they develop over time.

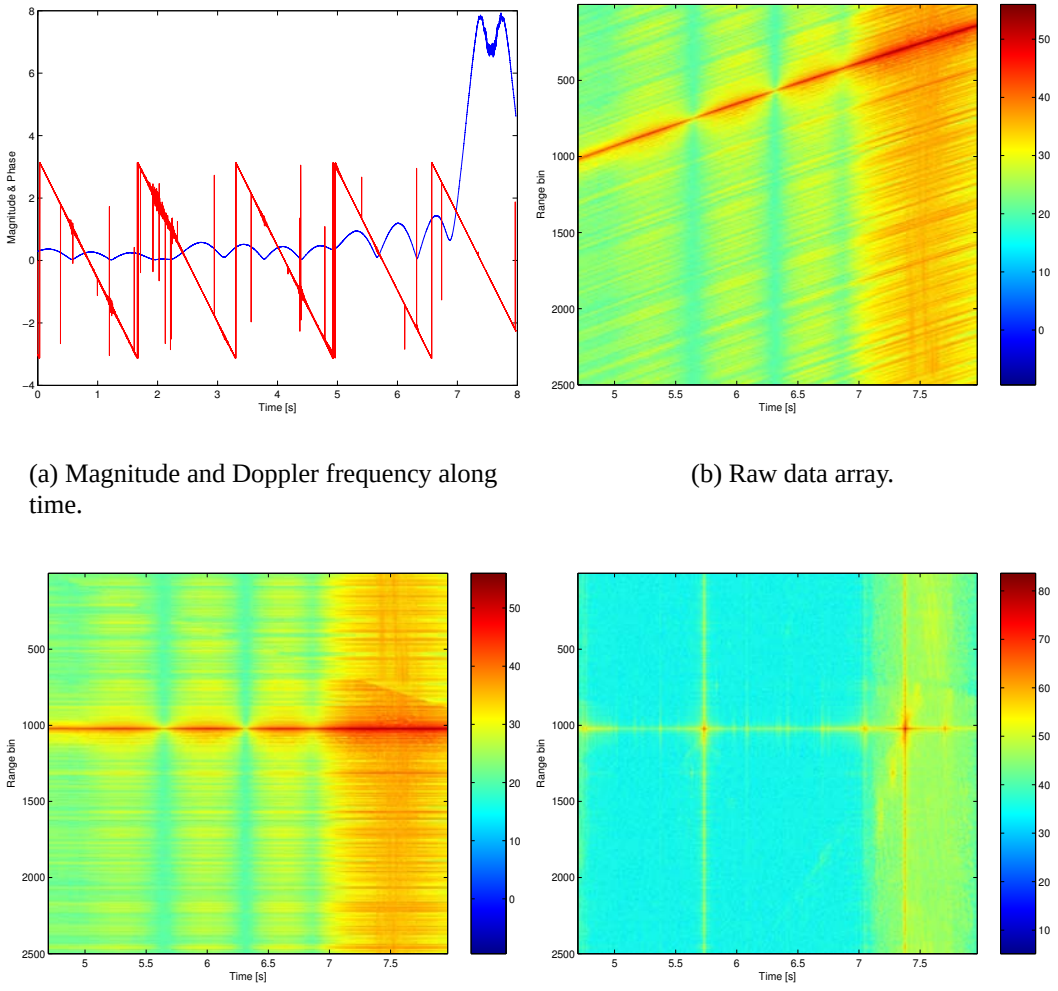

(a) Magnitude and Doppler frequency along time.

(b) Raw data array.

(c) Raw data array after range migration correction.

(d) Range and Doppler compressed raw data.

Figure 20: *Range migration correction and Doppler processing of direct path signal.*

The blue curve is the amplitude and clearly resembles RADARSAT-1's antenna pattern with its peak at around 7.5 s. Strictly speaking, it is the multiplication of the transmitter and receiver diagrams; However, in contrast to the narrow transmitter pattern, the receiver pattern is very wide and can be considered as almost constant over the plotted time interval. The dent in the centre of the mainbeam is caused by receiver saturation. However, the phase information is not effected which can be seen from the almost perfectly linear Doppler frequency (red curve) in this region. The Doppler frequency distribution is wrapped at the sampling limits of $\pm\mathrm{PRF}/2$. Large phase noise (spikes) occurs at areas with very small antenna pattern magnitudes. Re-ordering the continuous data stream by breaching it after each nominal PRI leads to the range-compressed raw data array in Fig. 20 (b). Due to the changing distance between the satellite and the receiver, a significant range walk can be observed for the direct path signal. The measured peak positions for each pulse can be used to correct for this walk, which is commonly called range migration correction, Fig. 20 (c).

In order to compress the range-migration corrected raw data in the Doppler direction, the corresponding Doppler parameter, i.e., the second order coefficient in (17), must be known, or can, for instance, be deduced from the phase history in Fig. 20 (a). It is either possible to estimate the slope of the Doppler frequency curve or to use the zero crossings to compute the desired Doppler chirp rate. Using the Doppler-time relation [41],

$$\omega_D(t) = 2kv_y + 2k\frac{v_a^2}{R_b}\left(t - t_b\right), \tag{103}$$

where v_y denotes the cross-track velocity of the Earth, and inserting the times $t_{r,l}$ at which the zero crossings occur, i.e., $2\pi f_D(t_{r,l}) = \pm\mathrm{PRF}/2$, we can solve the two equations for

$$\Delta t = t_r - t_l = \frac{\mathrm{PRF}\, R_b\lambda}{v_a^2}. \tag{104}$$

Using the time differences measured from Fig. 20 (a) the desired acceleration is estimated as $v_a^2/R_b = 44.567$ m/s^2. The point of closest approach t_c is characterized by the time at which the Doppler frequency vanishes, i.e., at the apex of the phase parabola. Setting $\omega_D(t_c) = 0$ in (103), the across track velocity can be estimated via $v_y = v_a^2/R_b(t_b - t_c)$. Since the direct path signal is under-sampled in the Doppler direction, multiple ambiguities arise; Analysing all phase maxima leads to two likely velocity estimates $\hat{v}_y = 299.376$ m/s and $\hat{v}_y = 372.233$ m/s, which are both roughly 40 m/s off the expected Earth rotation velocity of 340 m/s. This discrepancy is caused by two effects: First, the satellite is not in an exact polar orbit, but has a slight inclination angle so that the radial component perpendicular to the pass will differ somewhat; and secondly, a frequency offset between the two independent local oscillators will introduce a linear phase drift as shown in equation (15). The range migration corrected direct channel data can now be focused in

Doppler direction by correlation with the reference function (102) using the determined chirp rate. The result is plotted in Fig. 20 (d), where the sharply focussed 2D-sinc function is clearly visible together with one ambiguity. Since no weighting was applied, the sidelobes are rather high. The measured 3dB-mainbeam width is 15 m, which corresponds exactly to the theoretically predicted value in (86) (i.e., based upon RADARSAT-1's antenna aperture).

After having successfully compressed the direct channel signal, the same procedure was applied to the bistatic channel. Figure 21 shows the range compressed and range-migration corrected signals from channel one, i.e., the bistatic reflection from Stockbridge Hill (as measured over the entire antenna aperture). The compression and correction was done with the information gained from the direct path signal.

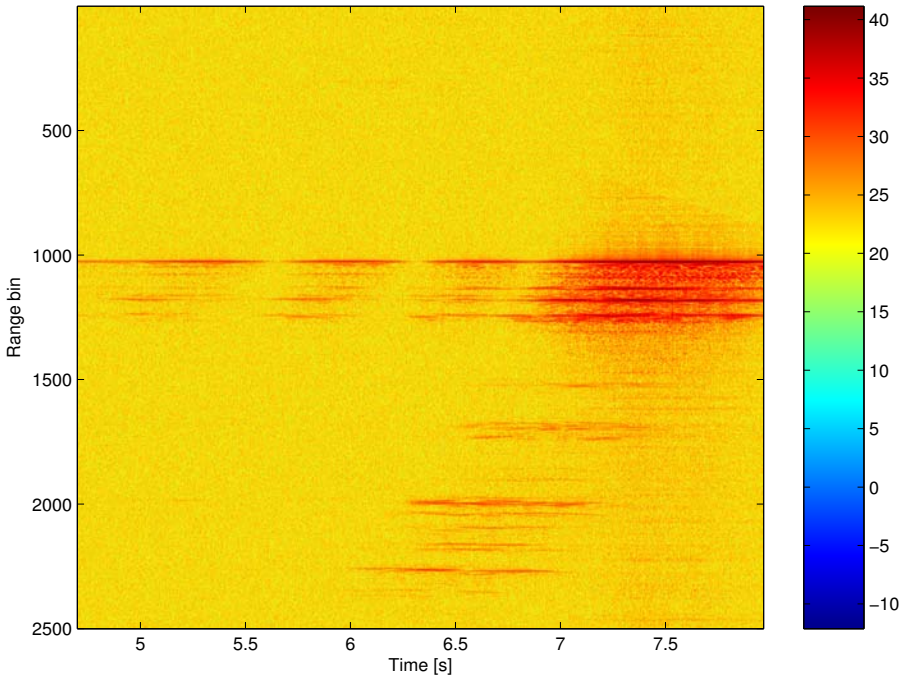

Figure 21 : *Range migration corrected bistatic raw data field.*

Since the Rooftop antenna is located in a dip (175 m elevation) it is actually steered upwards (with an elevation beamwidth of 2°) towards Stockbridge (see also Fig. 24 (b)) which is located at a higher altitude (400m). Due to this geometry, the bistatic channel also includes the direct path signal visible as the strongest reflection at range pixel 1020. No significant difference in range migration between near and far range occurs due to the relatively small synthetic aperture time of about one second. Hence, the applied correction values work for all ranges; the trajectories are straightened out everywhere within the 39 km swath (1500 pixels $\times c/B$). The

roughly 45° pointing angle of the receiver can clearly be seen. Convolution with the reference chirp in Doppler direction (102) with the previously determined chirp rate yields the final image Fig. 22.

Again, large sidelobes are visible because no weighting function was applied. Since the receiver beamwidth is relatively small (1°) the bistatic image (60 km x 60 km size) does not look like familiar monostatic images, but shows only a thin line. The lack of details is simply due to the limited ground resolution of about 15 m in Doppler and 30 m in range. A close-up look of size 2.2 km x 7.8 km in the vicinity of the receiver location is plotted in Fig. 23 (a). A few strong scatterers in a distance of several kilometers are evident, which most likely correspond to buildings near to AFRL.

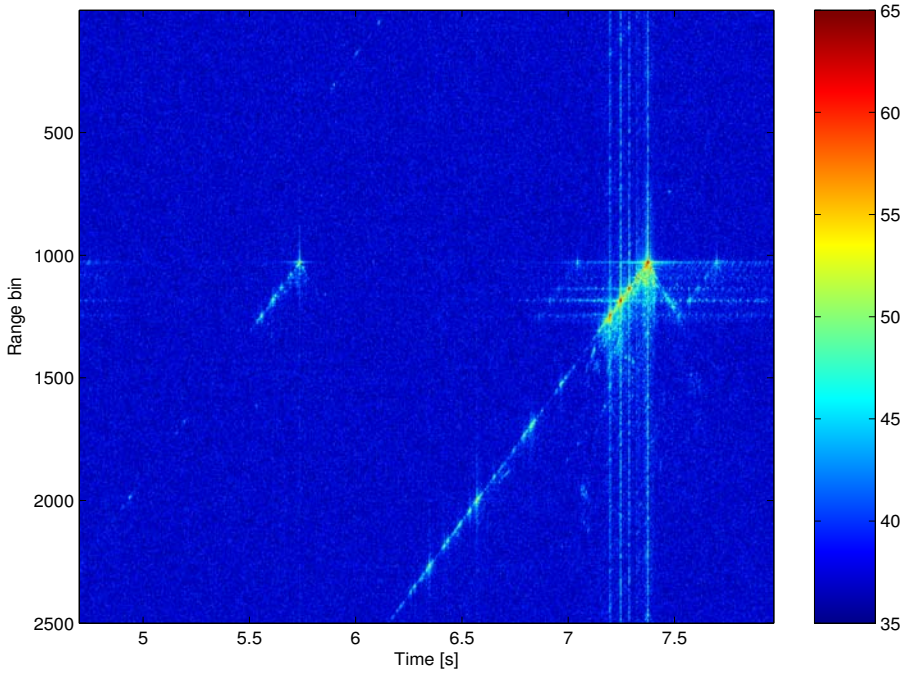

Figure 22 : *Range and Doppler compressed bistatic SAR data.*

Using only one sub-aperture of the entire antenna array, Fig. 23 (b) reduces the antenna beamwidth to about 8° and reveals more details while at the same time losing some gain. However, as expected, this will not increase the resolution of the system.

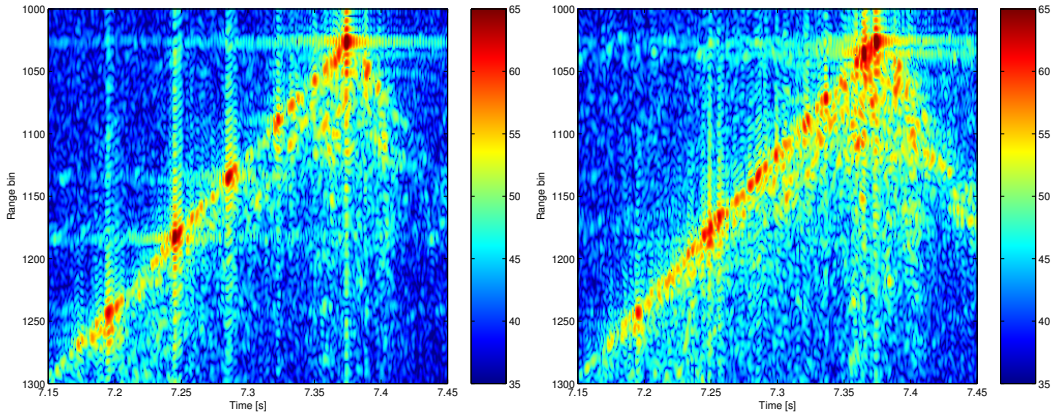

(a) Entire receiver array.

(b) Receiver subarray with wider beamwidth.

Figure 23: *Close-range around the receiver location.*

6.2 Convair 580 as illuminator

During a campaign on 1 November 2002 over the AFRL test site an airborne illuminator was used instead of RADARSAT-1. The radar system used was the Environment Canada CV 580 SAR. The radar, operating at C-band (5.30 GHz), was configured to use a transmitting antenna situated on the belly of the aircraft. Horizontally polarized radiation was transmitted, with most targets of interest situated at incidence angles of approximately 47°. The Radar system was run at a PRF of about 325 Hz. However, the PRF is automatically adjusted to match the aircraft velocity during the flight in order to maintain an equidistant ground sampling. At a $47°$ incidence angle, and an altitude of approximately 6.5 km, targets of interest were offset from the ground projection of the radar flight track by approximately 7 km. For the elevation beamwidth of $25°$ the swathwidth on the ground was approximately 6.56 km. Again, Stockbridge was chosen as the region of interest, roughly 28 km east of the Rooftop receiving antenna.

Also deployed during these trials was an active bistatic radar calibrator (ARC), Figure 24 (a), which was located on Stockbridge Hill in a distance of 30 km from the Rooftop. The two horn antennas are individually steerable into different directions; while the receiver horn 'looked' towards the aircraft, the transmitter horn was directed towards the receiver tower. The ARC-recirculation rate was set to 1.8 μs. Figure 24 (b) shows the surface plot of a Digital Elevation Model (DEM) for this area and the locations of the Rooftop antenna (centre cross), the ARC-reflector (cross at the lower-left of centre) and the flight line of the Convair (yellow arrow). The DEM illustrates that the receiver is located in a valley looking upwards to a

hilly region. The flight line was chosen to resemble the rooftop-RADARSAT-1 experiment, i.e., a quasi-forward looking bistatic geometry. These trials were jointly coordinated by DRDC Ottawa, Canada Centre for Remote Sensing (CCRS), and AFRL [42]. The rooftop receiver radar was working under the same conditions

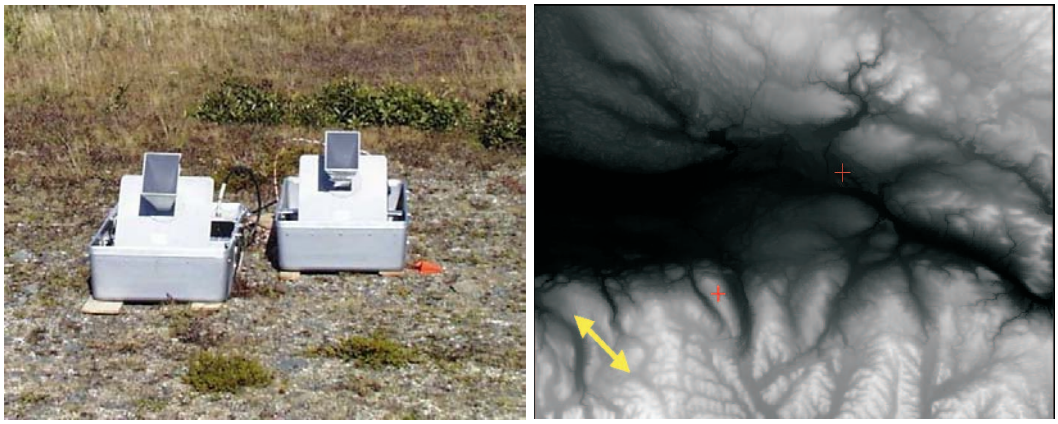

(a) Photograph.

(b) Surface plot of the DEM around AFRL, NY, (courtesy R. Hawkins et. al. [42]).

Figure 24: *Photograph and location of active radar calibrator (ARC) at the 1 Nov. 2002 airborne trial, crosses) receiver and ARC locations, arrow) flight path.*

and with identical system parameters as for the RADARSAT trials. The airborne transmitter, however, emits a non-linear frequency modulated pulse of $T = 7$ μs duration and a bandwidth of $B = 50$ MHz. However, since the low-pass filter in the final stage of the receiver hardware (before sampling) limits the signal bandwidth to 30 MHz, a resolution loss will occur compared to the monostatic case. For these parameters, Fig. 25 shows the predicted maximum synthetic aperture times and the ground range resolution, which indicate the poor range separability due to the forward scattering geometry. Again, one of the first measured pulses was extracted in order to compress all others in the range direction, Fig. 26 (a). The pulse length is $7\,\mu$s long as expected. The magnitude and unwrapped phases history of the resulting compressed peaks of the direct path is plotted in Fig. 26 (b). The magnitude is the result of the multiplication of the two different antenna diagrams of the transmitter and receiver. Due to the particular flight geometry the direct path signal is measured in sidelobe regions (both in azimuth and elevation) of the receiver and the transmitter. Therefore, the two-way antenna pattern is not symmetric and shows high sidelobes.

To re-order the continuous data stream into the range-time raw data array the varying PRF has to be taken into account. The range migration corrected raw data field

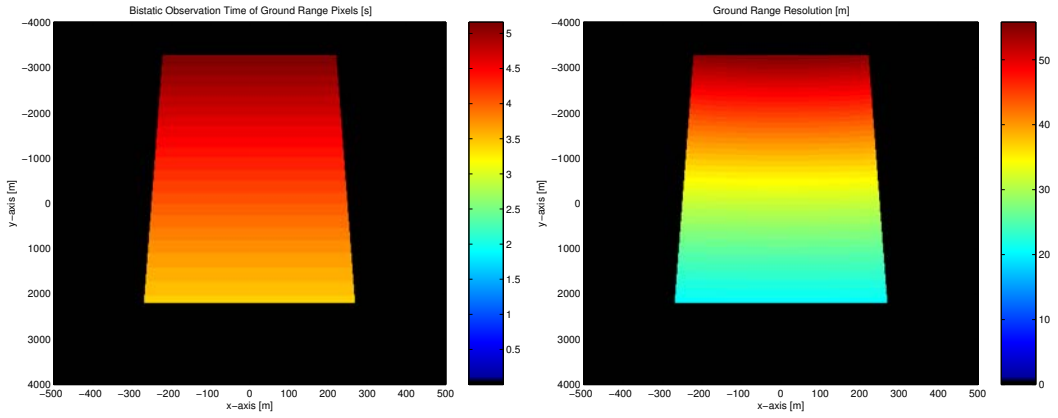

(a) Bistatic observation time.

(b) Ground range resolution.

Figure 25: *Predicted bistatic observation time and ground range resolution for the Convair-Rooftop trial on 1 Nov. 2002*

is shown in Fig. 28. A decibel scale was chosen in order to emphasize the much weaker ARC-returns. Due to the unfavourable flight geometry (sidelobe reception of direct path signal) any range migration correction using the direct path may not be reliable. Instead, it was found that it is much more precise to correct for range migration by using the ARC-returns in the reflection-free far range area about 3 km distant from the receiver, because the ARC-signal is measured within the main-beams of both radars. At the top of Fig. 28, the direct path signal contained in the bistatic reflections can also be seen. The relatively strong forward/sideward reflection from the Hill's slope appears up as a stripe around 2 km distant from the receiver. The bistatic reflections to the left of the center appear weaker than on the right side, which is in perfect agreement with the DEM structures in Fig. 24 (b). The noise-shaped reflection in-between are the reflections from the relatively flat area between the Rooftop and Stockbridge. Another stripe of much weaker reflections is seen around 4 km distance, probably stemming from a second, higher-located, ridge behind Stockbridge (as seen from the receiver). Multiple re-circulations from the ARC are also visible. With a re-circulation time of 1.8 μs and a sampling frequency of $f_s = 80$ MHz, the number of samples between the individual signals should be nominally 144; the measured value is 145 pixels. Each pixel corresponds to a distance of $\Delta r = c/f_s = 3.75$ m, i.e., the distance between two circulations is 543.75 m. Due to the nearly forward looking geometry, the entire illuminated ground swath of about 7 km is concentrated (compressed) in a roughly 500 m wide stripe in the 'slant' domain (raw data). In other words, the ground range resolution is drastically reduced, as expected from the theoretical results in Section 4.3, cf. also Fig. 13 (e-f) and Fig. 25 (b).

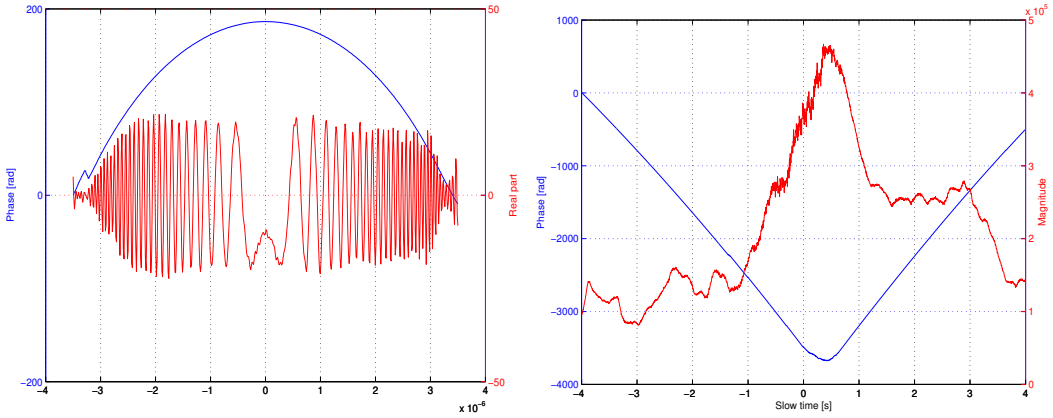

(a) Chirp signal; real part (red) and phase (blue).

(b) Direct path signal; magnitude (red) and phase (blue).

Figure 26: *Received chirp and direct path signals (magnitude and phase).*

In order to compress the range-migration corrected data in the Doppler direction, the Doppler chirp rate must be known. Unfortunately, the motion data for the Convair aircraft were not available. Therefore, an autofocus method was used, based on the phase information of the ARC in the far range. The magnitude and phase history of the ARC at 3 km range is plotted in Fig. 27 (a). While the magnitude is quasi constant over a large region, the Doppler phase follows a typical parabolic shape. However, the apex of the Doppler phase is shifted off the center of the magnitude pattern, which is a clear indicator for the presence of a linear phase term, e.g., [40].

The technique to estimate the linear and quadratic phase coefficient of the matched filter is adopted from the moving target parameter estimation scheme described in [40]. There, the two coefficients are influenced by the along-track (quadratic term) and across-track (linear term) velocity of a moving object. One proposed technique to estimate these two components are matched filter banks; the desired parameters $\underline{a} = [a_1, a_2]^T$ are varied throughout a bank of filters of form

$$s_{\text{ref}}(t, \underline{a}) = \exp\left(j(a_1 t + a_2 t^2)\right), \tag{105}$$

and the value at which the maximum output magnitude occurs represents the optimum estimate. Fig. 29 (a) shows the filter bank outputs for the chirp rate a_2 varied between 50 s^{-2} and 200 s^{-2}, where the linear term a_1 was set to zero. The maximum appears at a chirp rate of 121.4 Hz/s. The time at which this maximum occurs is $t_c = 2.24$ s, which represents the shifted (incorrect) position of the ARC in the SAR image. Again, this displacement is due the presence of the non-zero linear

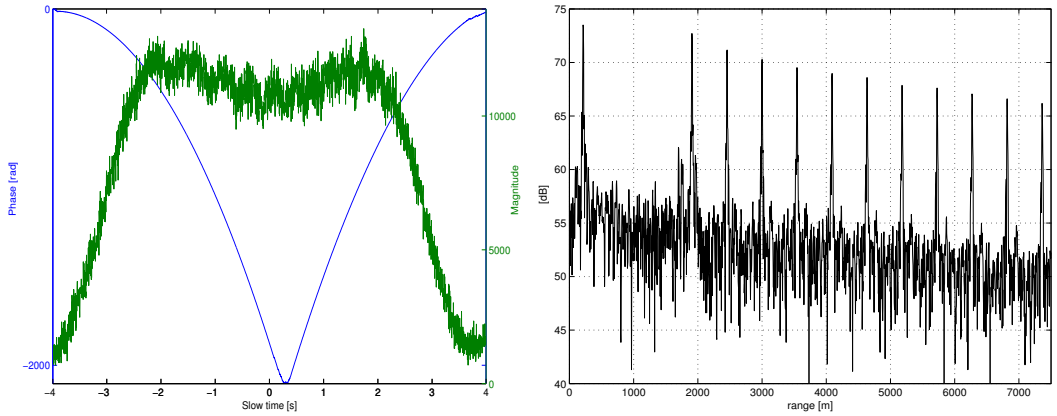

(a) Magnitude (green) and phase (blue).

(b) Magnitude of ARC-peaks.

Figure 27: *Magnitude and phase of ARC-signal at 3 km range and magnitudes of ARC-peaks along range.*

term a_1, which in terms of GMTI would correspond to non-zero radial or across-track velocity of the object. As known from the GMTI case, around the optimum chirp rate the matched filter responses shift away from t_c and broaden; the ridge is tilted and fans out at the edges [40]. These effects are also caused by the mismatch of a_1 in the matched filter and the data.

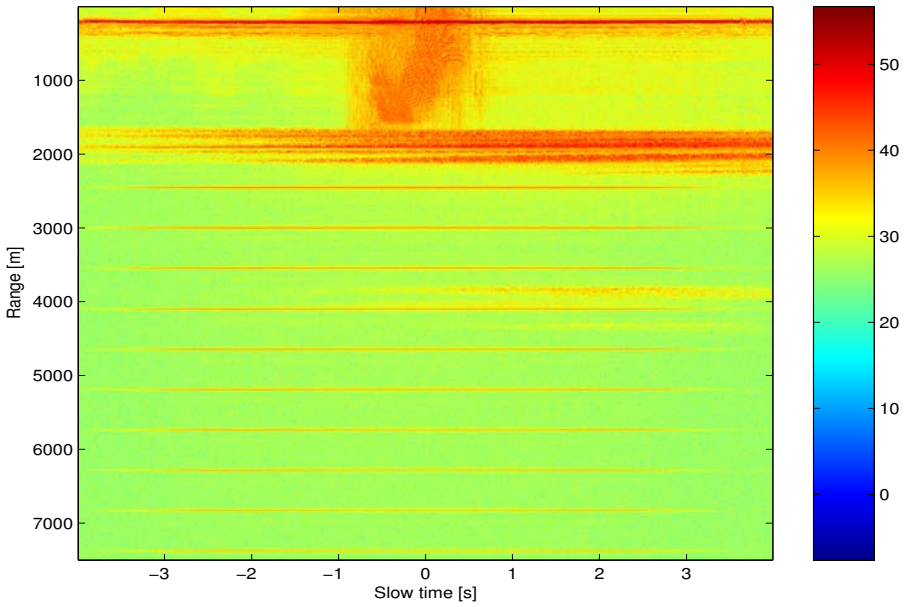

Figure 28 : *Range migration corrected raw data in logarithmic scale.*

Analogously, a matched filter bank for the linear term component a_1 can be used. In order to avoid ambiguous impulse responses, the length of the reference function should not exceed the length of the target trajectory. For a matched filter bank map where a_1 was varied from 0 to 1000 Hz, the maximum occurs at $a_{1,\mathrm{opt}} = 895$ Hz. Since the ARC was stationary, this frequency represents the difference of the local oscillators RF-frequencies $|f_1 - f_2| = 895$Hz.

Inserting this estimate into the reference function and repeating the a_2 matched filter bank results in Fig. 29 (b). The ambiguity is resolved, i.e., only one peak occurs; the ridge is now correctly shifted to the broadside time $t_b = -1.05$ s and the fan is straightened-out vertically. The impulse responses above the optimum value (about $a_2 = 117$ Hz/s) are not completely symmetric, which is caused by the presence of non-zero cubic phase terms [43]. This term is most likely caused by uncompensated aircraft motion errors. A matched filter bank for the cubic term (not shown here) resulted in $a_{3,\mathrm{opt}} = 1.16$ Hz/s^{-2}. Inserting the estimated phase

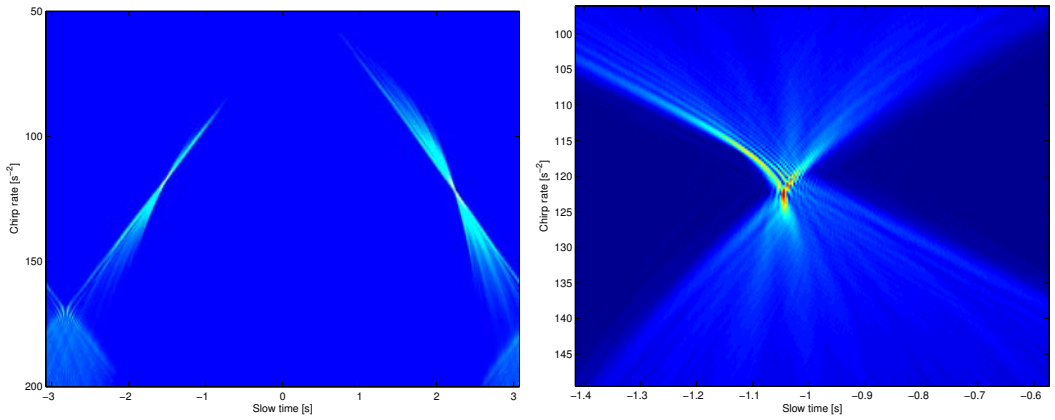

(a) Chirp rate. (b) Linear coefficient.

Figure 29: *Matched filter banks for the chirp rate and the linear phase coefficient based on the ARC-signal in Fig. 27 (b).*

coefficients into the reference function (105) and computing the convolution results in the bistatic SAR image shown in Fig. 30. All ARC-recirculations are correctly compressed and appear as a “line of dots” in the centre of the SAR image. The linearly decreasing magnitude (in dB scale) along range is confirmed in Fig. 27 (b).

Due to the very small ground range resolution details, such as streets, buildings fields etc. in the Stockbridge area are not recognizable However, by comparing Fig. 31 and the DEM in Fig. 24 (b), certain patterns in the slope structures (different ridges) in the DEM show up as reflections. Further, some compression gain is observable in the relatively flat region between the receiver and Stockbridge Hill.

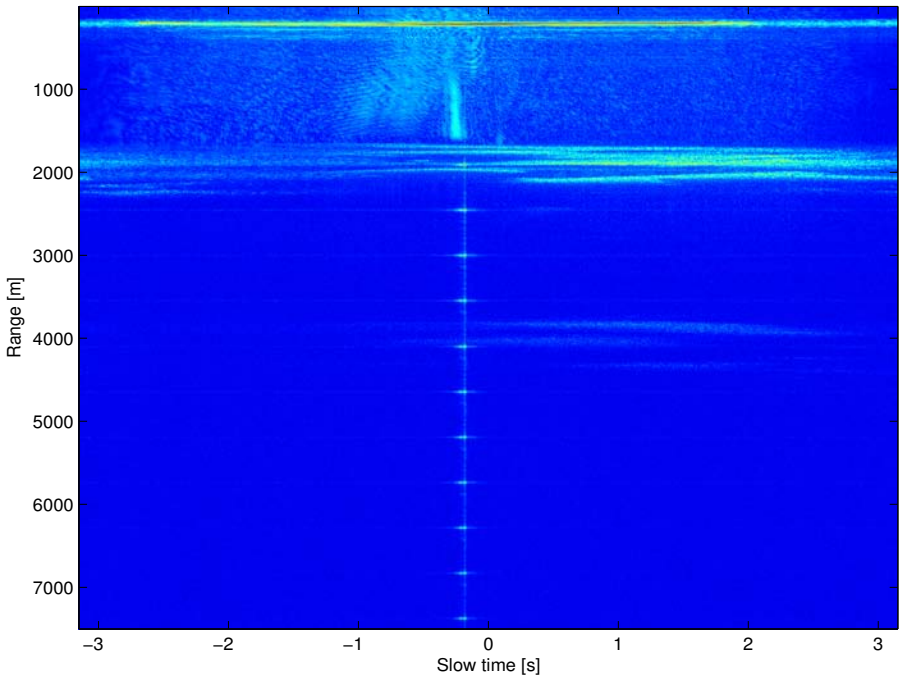

Figure 30 : *Bistatic SAR image for the 1 Nov. 2002 airborne trial.*

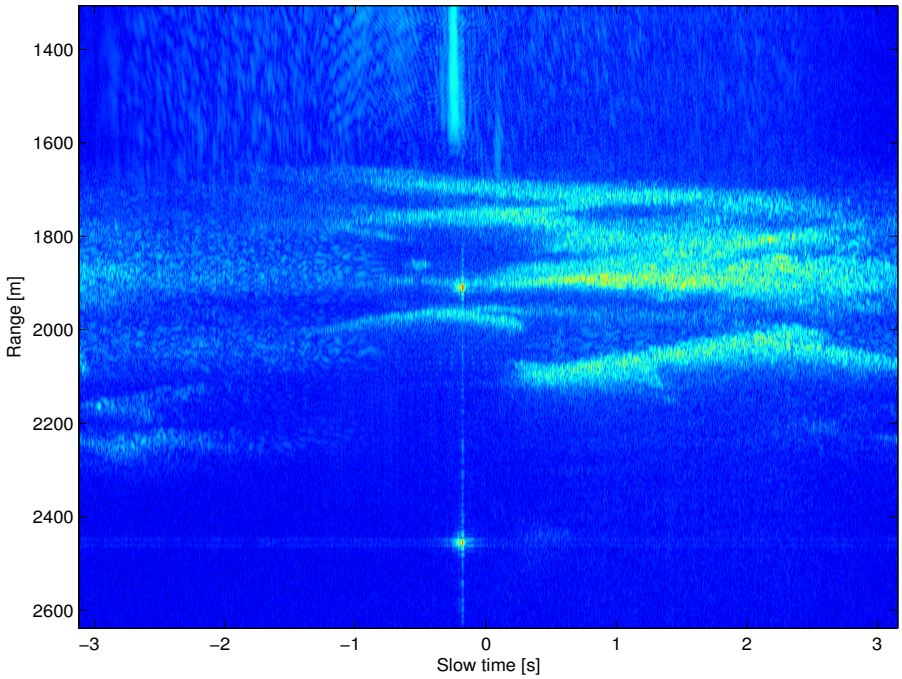

Figure 31 : *Bistatic SAR image for the 1 Nov. 2002 airborne trial around ARC location.*

6.3 Measured phase noise characteristics

This section investigates the phase noise characteristics measured during the bistatic clutter experiments at AFRL described in subsections 6.1 and 6.2. Since the direct path signal between the moving transmitter and the stationary receiver was observed, it is possible to explore the phase noise properties under practical conditions and to verify the theoretical results introduced in Section 2.3.

6.3.1 Rooftop-RADARSAT-1 experiment

Figure 32 (a) shows the direct-path signal phase along Doppler-direction (blue curve). This phase, confined to the area underneath the mainbeam ($T = 6.9$ s to 8 s), is given as the integral over the Doppler frequency plotted in Fig. 20 (a) (red). The green and the red curves show the residual phase after removing a second and third order polynomial fit from the Doppler phase. As expected, the satellite shows only small motion error induced phase deviations (e.g., a relatively small cubic term) over the synthetic aperture time of $T_s = 1.1$ seconds. The IISLR for the two curves are -15.3 dB and -19.3 dB according to Table 2, and hence, are getting close to the requirement of -20 dB. Figure 32 (b) confirms this finding by plotting the

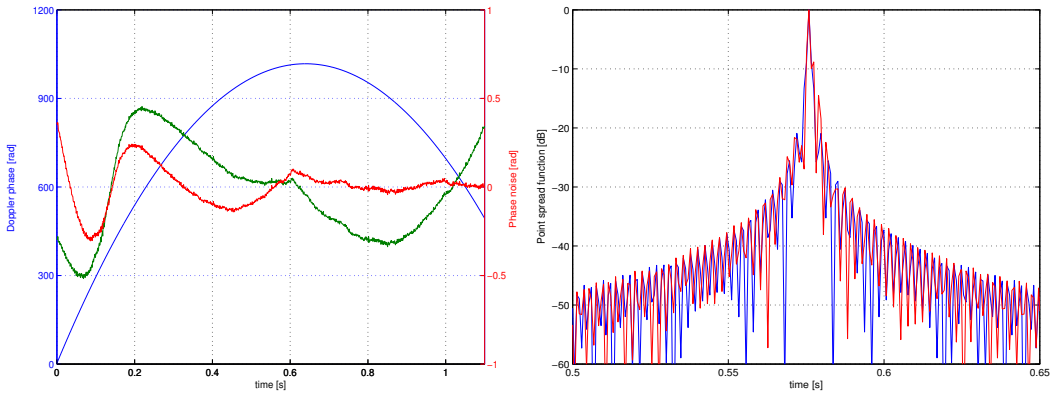

(a) Doppler phase (blue) and phase noise (red, green).

(b) PSF, ideal (blue), noisy (red).

Figure 32: *Measured phase noise of Rooftop-RADARSAT-1 experiment and impact on point spread function.*

point spread functions with and without the shown phase noise residual. The blue curve represents the undisturbed PSF for the estimated polynomial coefficients, i.e., the fitted Doppler rate. The red curve indicates the PSF when the residual noise (green) is added to the signal and then compressed with the undisturbed matched

filter. Only a slight one-sided increase of the peak sidelobe is observed due to the remaining cubic phase error but virtually no increase in ISLR.

6.3.2 Rooftop-Convair 580 experiment

For the airborne illuminator, the scenario is entirely different. Since no motion compensation on the data was performed due to non-availability of the INS/GPS aircraft data, motion induced phase errors (caused by deviations from a perfectly straight flight line and constant velocity) will be superimposed on the oscillator phase noise. Figure 33 (a) shows the residual phase noise in the direct path signal over eight seconds after removal of quadratic and cubic polynomial fits from the measured Doppler phase (blue curve) in Fig. 26 (b). A much larger standard deviation of 1.16 rad and 0.75 rad, respectively is seen (these values are too large to allow computation of the IISLR via (37)).

The drastic impact on the PSF, even for the third order phase noise residual, is visible in Fig. 33 (b). Alongside a significant increase of the peak sidelobes, a left-sided increase of the side lobes and an increased ISLR are recognized. While the one-sided sidelobe increase points to unresolved higher-order low-frequency phase noise terms, the two peak sidelobes occur as ghost targets, which might be caused by the sinusoidal, low-frequency structure in Fig. 32 (a), [24]. However, this

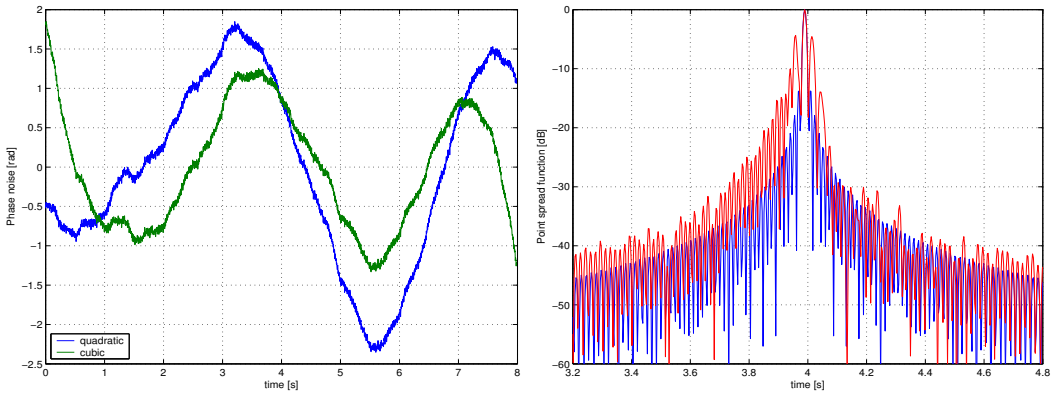

(a) Phase noise.

(b) PSF, ideal (blue), noisy (red).

Figure 33: *Measured phase noise of Rooftop-Convair 580 experiment and impact on point spread function.*

situation improves substantially for shorter coherent processing times. For instance, halving this time to $T_s = 4$ s leads to much smaller standard deviations, i.e., to IISLRs of -14.2 dB and -19.7 dB, respectively. Correspondingly, the PSF for four

seconds (third order polynomial fit) is almost undistinguishable from the blue curve in Fig. 33 (b) and is therefore not plotted.

Even though the motion error induced phase noise and the oscillator phase noise contributions are inseparable without proper INS data, Fig. 34 reveals some deeper insight. Here, the estimated power spectral density after removal of up to second order or third order polynomial fits is plotted within the unambiguous frequency band (PRF = 325 Hz). The Fourier transform reveals discrete phase noise at about 72 Hz, which are known to be caused by propeller shaft vibrations of the Convair 580. The other spikes at about 30 Hz, 120 Hz and 180 Hz are probably due to frame vibrations of the aircraft (due to under-sampling of the azimuthal bandwidth, some are most likely ambiguous frequencies folded back into the PRF-region). These vibrations cause the oscillator to shake, which in turn will perturb the oscillator frequency (phase) due to its 'g-sensitivity'. A detailed, experiment based, analysis of motion and vibration induced phase jitter and the resultant limitations on the coherent processing time will be performed during phase II of this TIF project.

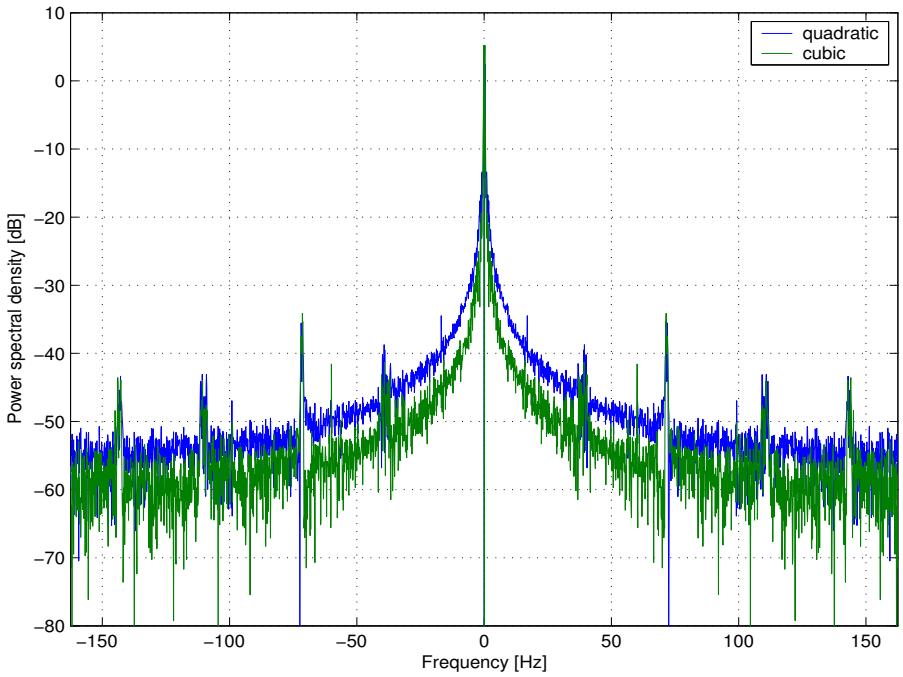

Figure 34 : *Power density spectrum of phase noise for Rooftop-Convair 580 experiment.*

In contrast, the estimated power spectral density for the RADARSAT-1-Rooftop experiment shows no such spikes, as expected.

7 Bistatic SAR processing

Finding fast and reliable processing algorithms for the geometrically more demanding bistatic configuration is a relatively open field of research at present. Some work on this field had been reported in the early papers by Soumekh [44, 45, 46] and others [47, 48]. However, to date, most bistatic SAR processors are based on the matched filter principle and are, in fact, solely time domain correlators [49, 50]. Time domain correlation or convolution is universally applicable to any bistatic configuration (including monostatic) and is relatively simple to implement. For these reasons we have adopted the matched filter processor that is described in this section. Future work will certainly include investigation of alternative processors.

The major drawback of the time domain technique is the enormous computational load involved that leads to intolerable processing times. Unlike monostatic SAR, the kernel function for bistatic cases is non-separable and, hence, the use of fast operators such as the Fast Fourier Transform (FFT) is prevented, [16]. Recently, Ender [51] explored the theoretical background of bistatic Doppler compression and has proposed numerical methods to separate the kernel. Some useful analytic expressions for bistatic geometry can also be found in [17]

Let us assume that the bistatic geometrical history is accurately known, for instance, by measurements from Global Positioning System (GPS), differential GPS, and Integrated Inertial System (INS) equipment on-board the platforms. Then, the range and Doppler history of any scatterer (location) on the bistatically observed ground is a-priori known. In other words, the range trajectory of a particular scatterer can be predicted within the two-dimensional raw data field, including the range walk and range migration, see Fig. 35. Note that the range-trajectory for a bistatic SAR is generally not a parabola as compared to the monostatic case. The shaded areas around the tracks represent the duration of the transmitted pulses. After range compression, which is done identically to the monostatic case, this shaded region is compressed down to a narrow line, where the width of the line is determined by the range-resolution of the system, see Section 4.3.

To fully identify the individual scatterer tracks in the raw-data array, a precise time keeping is required for the range gating. In other words, one must be able to assign the exact bistatic distance (near-range) to the time when the range gates are opened at the receiver. Since illuminator and receiver are spatially separated, this is equivalent to a non-trial synchronisation issue. Time synchronisation can actually be done directly, i.e., with an extra link between the transmitter and receiver, or indirectly using identical stable clocks. The first technique was applied during the bistatic clutter trials described in Chapter 6.

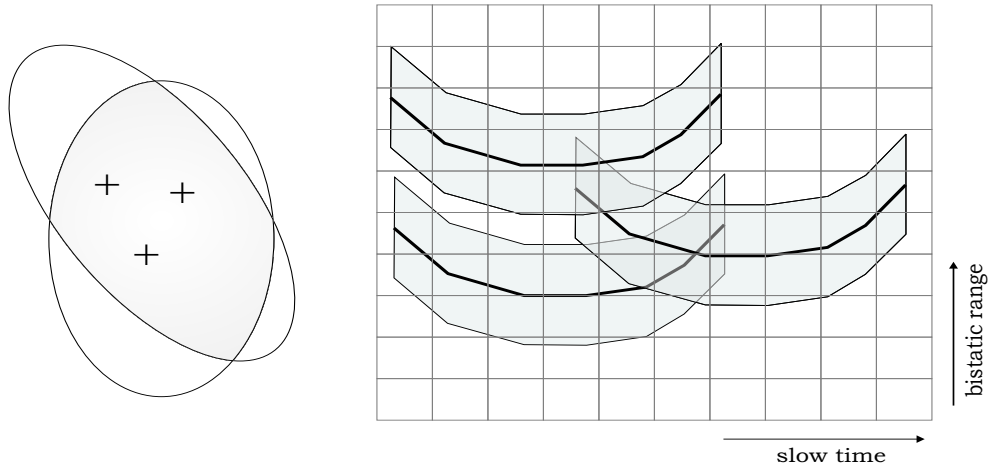

Figure 35 : *Illustration of a bistatic raw data field (right) showing three individual range trajectories for scatterer locations specified in the illuminated footprint on the ground (left).*

Indirect time synchronisation for range-gating based on the pulse-per-second (PPS) signal of the GPS offers greater flexibility to use in future systems as well as reduced hardware changes on the existing aircraft [21, 28]. As such it is intended for the experimental set-up in phase II of this project. However, the fewer modifications to the hardware have to be traded with less accuracy, i.e., a larger uncertainty in the range cell position; this error is expected to be less than ten ns.

By examining Fig. 35, the task of how to compress the energy for each image pixel becomes clear; one must re-collect the spread energy along the a priori known trajectories. This is done by convolving the measured data along the trajectory with the theoretical slow-time signal (matched filter) created by a potential scatterer at a particular location in the image. A slightly different way of executing this Doppler processing is referred to as Algorithm 1, as described in appendix G. Here, for each range-line (pulse return), a complete image is computed. The ensemble of images are then subsequently added coherently. The energy of the echoes of each pulse are distributed throughout the image according to the a priori known distance between image pixels and the platform positions. The introduced algorithm has been implemented and tested on the experimental bistatic clutter data from 28 January 2002, as described in Section 6.1.

Figure 36 shows the Doppler focussed image for a small area around Stockbridge Hill. Three sperate scattering centers along a quasi-straight line can be seen along with their ghost replicas. In order to understand this phenomenon, three equi-Doppler (red) and equi-range (yellow) lines are superimposed onto the image. Evidently the ghost images appear exactly at the intersections of these lines, confirming ambiguous echoes caused by the quasi forward looking geometry. Scatterers at

these locations (intersection points) would generate exactly identical slow time histories in range and Doppler, i.e., would exactly lay on top of each other in Fig. 35 and possess identical Doppler histories. Further details of this algorithm and its properties can be found in [52].

In contrast, the same kind of ghost images did not appear in Fig. 23 since a direct convolution with the estimated Doppler history (chirp signal) was applied, which will produce only one single match whenever the matched filter lines up exactly with the measure data. However, the technique used in Section 6 is only a crude approximation because the range migration correction was assumed constant over the entire image, but therefore is about one-hundred times faster.

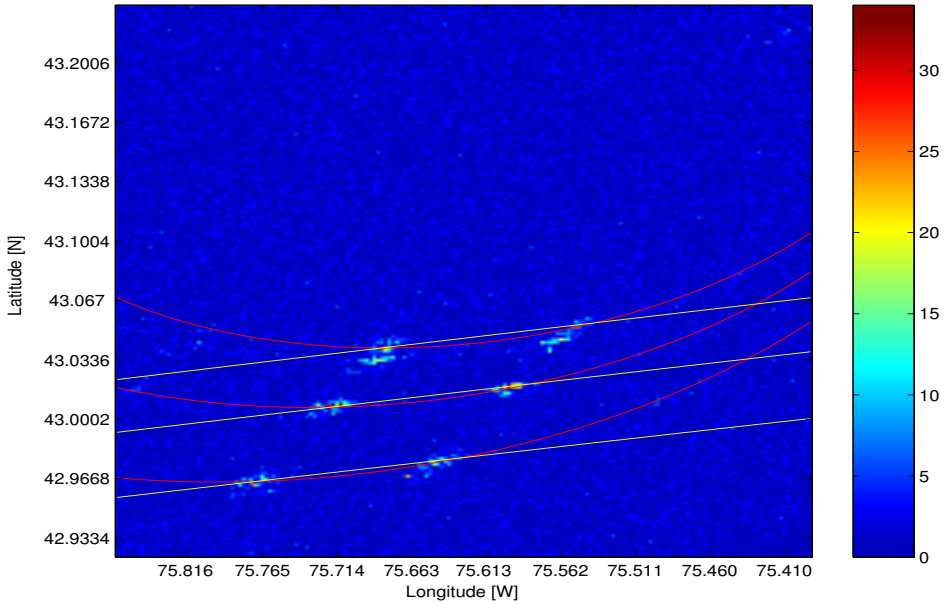

Figure 36 : *SAR image processed with algorithm one and overlayed equi-range and equi-Doppler lines for three strong scatterers.*

8 Summary and outlook

This report described the results of phase I of the TIF project on bistatic SAR. This phase lasted one year and was concerned with gaining a deeper knowledge of bistatic SAR and a thorough understanding of its properties based on theoretical analysis as well as analysis of existing experimental space-borne and airborne SAR data sets.

A complete theoretical framework for the bistatic SAR resolution on the ground was developed. Using this mathematical tool, the range and Doppler ground resolution can be predicted for any arbitrary bistatic flight geometry. By using the time-dependent range and Doppler gradients and the bistatic observation time, this can be achieved without actually calculating the point spread or impulse response function, which makes it computable in quasi real-time. In addition, due to their simplicity, this set of equations can be used for mission planing where the optimum flight lines must be determined in order to achieve a minimum required resolution for a given area of interest. Further, performance degradation in terms of reduced geometric and radiometric resolution of the point spread function caused by severe phase noise due to separate oscillators was investigated.

In order to verify these theoretical results a complete bistatic raw data simulator has been developed and implemented in MATLAB©. The simulator generates the raw data with high accuracy including the full three-dimensional geometry, the antenna diagrams, and the complex RCS for any number of point scatterers located on the ground. Hence, realistic effects such as range migration and magnitude weighting are automatically included. A more practical scene including features such as streets, fields etc., could be assembled from an ensemble of point scatterers. However, the computational complexity increases drastically in proportion to the number of scatterers. The simulator also allows antenna squinting, as is commonly done in special SAR modes such as SlideSAR and SpotSAR.

The simulated raw data are used to test the performance of bistatic SAR processing algorithms. In particular, a ‘brute force’, time domain SAR processor was introduced in Section 7. Although this type of processor is very time consuming, it is based on the matched filter approach and is, therefore, flexible and applicable to any complex geometry.

The last part of the report dealt with the analysis of experimental data collected at bistatic clutter trials at Rome, NY throughout 2002. These trials comprised a moving transmitter (either the RADARSAT-1 satellite or the Environment Canada Convair-580 aircraft) and a stationary receiver antenna located on the premises of AFRL. Since the main motivation for those trials was to collect and build-up data bases for bistatic clutter properties and bistatic GMTI a relatively narrow receiver

antenna beamwidth was sufficient. However, due to the relative motion between the two separate radars, these data sets are in principle also suitable for Doppler processing, i.e., bistatic compression/focussing in the 'cross-range' direction to enhance the resolution. Although no special measures were taken to ensure phase coherence between transmitter and receiver, i.e., the two stable local oscillators were running freely during the measurements, both data sets have successfully been focussed to the theoretically expected resolutions. This was mainly due to the relatively small synthetic aperture times of up to only a few seconds in both cases.

In Phase II of the project, deeper insight into the functionality of a bistatic SAR system and the physical properties of its SAR imagery will be gained by experimental measurements conducted by DRDC Ottawa's airborne SpotSAR radar system. Designing and constructing a secondary receiver which will be placed on top of a stationary platform (e.g., a tower or a high building) and locating the transmitter on the maneuvering aircraft, represents the simplest useful bistatic configuration and is of particular interest for evaluating the performance limits for scenarios without any receiver platform motions. Indirect time synchronisation for range-gating based on the pulse-per-second (PPS) signal of the global positioning system (GPS) is intended for the experimental set-up because of the reduced hardware changes on the existing aircraft. The received echoes from the illuminated ground spot would be recorded and stored for off-line processing. Flight trials with different bistatic geometries and varying imaged scenarios, such as different vegetation or imported man-made targets (cars etc.), are anticipated to be conducted during phase II of the project.

References

1. Willis, N. J. (1995). Bistatic Radar, 2 ed. Silver Spring, MD: Technology Service Corporation.

2. Willis, N. J. (2002). Bistatic Radars and Their Third Resurgence: Passive Coherent Location. IEEE Radar Conference Tutorial 2.1.

3. Retzer, G.. (1980). A Concept for Signal Processing in Bistatic Radar. In *IEEE Int. Radar Conference*, pp. 288–293.

4. Kirk Jr., J. C. (1985). Bistatic SAR Motion Compensation. In *IEEE International Radar Conference*, pp. 360–365. New York, USA.

5. Ferrazzoli, P., Guerriero, L., DelMonaco, C. I., and Solimini, D. (2003). A further inside into the potentials of bistatic SAR in monitoring the earth surface. In *Proc. of IGARSS'03*, Toulouse, France.

6. Moccia, A., Rufino, G., and De Luca, M. (2003). Oceanographic Application of Spaceborne Bistatic SAR. In *Proc. of IGARSS'03*, Toulouse, France.

7. Krieger, G., Fiedler, H., Hounam, D., and Moreira, A. (2003). Analysis of System Concepts for Bi- and Multistatic SAR Missions. In *Proc. of IGARSS'03*, Toulouse, France.

8. Krieger, G., Fiedler, H., Hounam, D., and Moreira, A. (2003). Bi- and Multi-Static SAR Missions: Potentials and Challenges. In Agency, Canadian Space, (Ed.), *Advanced SAR Workshop*, Saint-Hubert, Quebec, Canada.

9. Eineder, M. (2003). Oscillator Clock Drift Compensation in Bistatic Interferometric SAR. In *Proc. of IGARSS'03*, Toulouse, France.

10. Cerutti-Maori, D. and Ender, J. H. G. (2003). An Approach to Multistatic Spaceboren SAR/MTI Processing and Performance Analysis. In *Proc. of IGARSS'03*, Toulouse, France.

11. Whitewood, A. P., Müller, B.R., Griffiths, H. D., and Baker, C. J. (2003). Bistatic Synthetic Aperture Radar with Application to Moving Target Detection. In *International Conference on Radar*, pp. 529–534. Adelaide, Australia.

12. Pileih, C. and Beard, J. K. (2000). Bistatic GMTI experiment for airborne platforms. In *IEEE International Radar Conference*, pp. 42–46. Washington, D.C.

13. Cazzani, L., Colesanti, C., Leva, D., Nesti, G., Prati, C., Rocca, F., and Tarchi, D. (2000). A Ground-Based Parasitic SAR experiment. *IEEE Trans. Geoscience and Remote Sensing*, **GRS-38**(5), 2132–2141.

14. Retzer, G.. (1979). A Passive Detection System for a Wide Class of Illuminator Signals. In *Proc. IEEE Int. Conf. Acoust., Speech, Signal Processing*, pp. 620–623. Washington, D.C.

15. Homer, J., Mojarrabi, B., Palmer, J., Kubic, K., and Donskoi, E. (2003). Non-cooperative Bistatic SAR Imaging System: Spatial Resolution Analysis. In *Proc. of IGARSS'03*, Toulouse, France.

16. Ender, J. H. G. (2003). Signal Theoretical Aspects of Bistatic SAR. In *Proc. of IGARSS'03*, Toulouse, France.

17. Loffeld, O., Nies, H., Peters, V., and Knedlik, S. (2003). Models and Useful Relations for Bistatic SAR Processing. In *Proc. of IGARSS'03*, Toulouse, France.

18. Gierull, C. H. and Sikaneta, I. (2004). Ground Moving Target Parameter Estimation for Two-Channel SAR. In *Proc. of EUSAR*, pp. 799–802. Ulm, Germany.

19. Adams, J. W. and Schifani, T. M. (1987). Waveform Error Analysis for Bistatic Synthetic Aperture Radar Systems. In *Inter. Radar Conf.*, pp. 479–483. London, UK.

20. Massonnet, D. and Vadon, H. (1995). ERS-1 Internal Clock Drift Measured by Interferometry. *IEEE Trans. Geoscience and Remote Sensing*, **GRS-33**(2), 401–408.

21. Weiß, M. (2003). EBiRa: Experimental Bistatic Radar for air surveillance. In *Proc. of IGARSS'03*, Toulouse, France.

22. Rutman, J. and Walls, F. L. (1991). Characterization of Frequency Stability In Precision Frequency Sources. *Proc. of the IEEE*, **79**(6), 952–960.

23. Auterman, J. L. (1984). Phase Stability Requirements for a bistatic SAR. In *Proc. IEEE Int. Radar Conf.*, pp. 48–52. Atlanta, GA.

24. Carrara, W. G., Goodman, R. S., and Majewski, R. M. (1995). Spotlight Synthetic Aperture Radar, Artech House.

25. Allan, D. W. (1987). Time and Frequency (Time-Domain) Characterization, Estimation, and Prediction of Precision Clocks and Oscillators. *IEEE Trans. on Ultrasonics, Ferroelectrics, and Frequency Control*, **34**(6), 647–654.

26. Cutler, L. S. and Searle, C. L. (1966). Some Aspects of the Theory and Measurment of Frequency Fluctuations in Frequency Standards. *Proc. of IEEE*, **54**(2), 136–154.

27. Damini, A, Haslam, G., Balaji, B., and Goulding, M. (2004). A new X-band Experimental Airborne Radar for SAR and GMTI. In *Proc. of EUSAR*, pp. 639–642. Ulm, Germany.

28. Weiß, M. (2004). Time and Frequency Synchronisation Aspects for Bistatic SAR. In *Proc. of EUSAR*, Ulm, Germany.

29. Böhme, J. F. (1993). Stochastische Signale, Stuttgart: Teubner-Verlag.

30. Papoulis, A. (1991). Probability, Random Variables and Stochastic Processes, 3 ed. McGraw Hill Inc.

31. Ender, J. H. G. (1991). Analyse der Selbstfokussierung eines Radars mit synthetischer Apertur (SAR) unter Verwendung einer Gruppenantenne. Ph.D. thesis. Ruhr-Universit”at Bochum.

32. Snarski, C. A. (1994). A phase error estimation algorithm: theory, application, and examples. In *Proc. of the SPIE*, Vol. 2230, pp. 72–86. Orlando, FL.

33. Ender, J. H. G. (2001). The Meaning of K-Space for Classical and Advanced SAR-Techniques. In *Proc. of PSIP*, pp. 1–13. Marseilles.

34. Cardillo, C.P. (1990). On the Use of the Gradient to Determine Bistatic SAR Resolution. In *Proc. of Int. Symp. Antennas and Propagation, Vol II*, pp. 1032–1035. Dallas, TX.

35. Walterscheid, I., Brenner, A. R., and Ender, J. H. G. (2004). Geometry and Stystem Aspects for a Bistatic Airborne SAR-Experiment. In *Proc. of EUSAR*, pp. 567–570. Ulm, Germany.

36. Chiron, O. (1997). Analysis of bistatic synthetic aperture radar images. In KAG-15, (Ed.), *Participation in Space Based Radar Experiments (Final Report)*, The Technical Cooperation Program (TTCP).

37. I., Walterscheid, Brenner, A. R., and Ender, J. H. G. (2004). Results on bistatic synthetic aperture radar. *Electronics Letters*, **40**(19), 1224–1225.

38. Livingstone, C., Sikaneta, I., Gierull, C. H., Chiu, S., Beaudoin, A., Campbell, J., J., Beaudoin, Gong, S., and Knight, T. (2002). An Airborne SAR Experiment to Support RADARSAT-2 GMTI. *Canadian J. Remote Sensing*, **28**(6), 1–20.

39. Tunaley, J. and Çotuk, N. (2004). Analysis of Bistatic Radar Data Collected by AFRL on 28 Jan. 02. (Technical Report TR 2004-xxx). Defence R&D Canada – Ottawa. Canada.

40. Gierull, C. H. and Livingstone, C. (2004). SAR-GMTI Concept for RADARSAT-2. In Klemm, R., (Ed.), *The Applications of Space-Time Processing*, Stevenage, UK: IEE Press.

41. Gierull, C. H. and Sikaneta, I. (2003). Raw Data Based Two-Aperture SAR Ground Moving Target Indication. In *Proc. of IGARSS'03*, Toulouse, France.

42. Hawkins, R., Murnaghan, K. P., Wind, A., Nedelcu, S., and Choeurng, V. (2003). Monostatic SAR Summary from Rome NY Novenmber 1, 2002. (Technical Note CCRS-TN 2003-06). Canada Centre for Remote Sensing. Canada.

43. Sharma, J. (2004). The influence of target acceleration on parameter estimation and focusing in SAR imagery. Master's thesis. University of Calgary.

44. Soumekh, M. (1991). Bistatic Synthetic Aperture Radar Inversion with Application in Dynamic Object Imaging. *IEEE Trans. Signal Processing*, **39**(9), 2044–2055.

45. Soumekh, M. (1998). Wide-Bandwidth Continous-Wave Monostatic/Bistatic Synthetic Aperture Radar Imaging. In *Inter. Conference on Image Processing*, pp. 361–364. Chicago, IL.

46. Soumekh, M. (1998). Bistatic Synthetic Aperture Radar Imaging Using Wide-Bandwidth Continous-Wave Sources. In *SPIE Conference on Radar Processing Technology and Applications III*, Vol. 3462, pp. 99–109. San Diego.

47. Arikan, O. and Munson Jr., D. C. (1988). A Tomographic Formulation of Bistatic Synthetic Aperture Radar. In *Inter. Conf. on Advances in Communication and Control Systems*, pp. 289–302. Baton Rouge.

48. Ding, Y. and Munson Jr., D. C. (2002). A Fast Back-Projection Algorithm for Bistatic SAR Imaging. In *IEEE Inter. Conf. on Image Processing*, New York.

49. Cantalloube, H., Wendler, M., Giroux, V., Dubois-Fernandez, P., and Krieger, G. (2004). Challenges in SAR processing for airborne bistatic acquisition. In *Proc. of EUSAR*, pp. 577–580. Ulm, Germany.

50. Yates, G., Horne, M., Blake, A. P., Middleton, R., and Andre, D. B. (2004). Bistatic SAR image formation. In *Proc. of EUSAR*, pp. 581–584. Ulm, Germany.

51. Ender, J. H. G. (2004). A Step to Bistatic SAR Processing. In *Proc. of EUSAR*, pp. 359–363. Ulm, Germany.

52. Çotuk, N. and Gierull, C. H. (2004). Time Domain Bistatic SAR Processor. (Technical Report TM 2004-000). Defence R&D Canada - Ottawa.

53. Golub, G. H. and Van Loan, C. F. (1989). Matrix Computations, Baltimore: Johns Hopkins University Press.

54. Ender, J. H. G (1999). Konventionen über Koordinatensysteme etc. FGAN Internal Note.

Annex A
Mean and variance of the impulse response function in presence of white oscillator jitter

According to (32), the expectation and second moment function of the impulse response in the range direction are

$$\begin{aligned}
\mathrm{E}\, P(t) &= e^{-j\omega_1\tau}\frac{1}{T}\int_{-T/2}^{T/2} e^{j\pi\frac{B}{T}\left((t-t'-t_n-\tau)^2-t'^2\right)}\,\mathrm{E}\left\{e^{j\Xi_1(t-t'-\tau)}e^{-j\Xi_2(t-t')}\right\}\,dt' \\
\mathrm{E}\,|P(t)|^2 &= \frac{1}{T^2}\int_{-T/2}^{T/2}\int_{-T/2}^{T/2} e^{j\pi\frac{B}{T}\left((t-t'-t_n-\tau)^2-t'^2\right)}e^{j\pi\frac{B}{T}\left((t-\bar{t}-t_n-\tau)^2-\bar{t}^2\right)} \\
&\qquad \cdot\mathrm{E}\left\{e^{j(\Xi_1(t-t'-\tau)-\Xi_2(t-t')-\Xi_1(t-\bar{t}-\tau)+\Xi_2(t-\bar{t}))}\right\}\,dt'd\bar{t}. \qquad \text{(A.1)}
\end{aligned}$$

Let the vector $\underline{\Xi}$ be Gaussian distributed with expectation zero and covariance matrix $\mathbf{K}$, i.e.,

$$\underline{\Xi} = [\Xi_1(t_1), \Xi_2(t_2), \Xi_1(t_3), \Xi_2(t_4)]' \quad \sim \quad \mathcal{N}(\underline{0}, \mathbf{K}), \qquad \text{(A.2)}$$

where the covariance matrix is given as

$$\mathbf{K} = \begin{pmatrix} \sigma_1^2 & 0 & c_{\Xi_1\Xi_1}(t_1-t_3) & 0 \\ 0 & \sigma_2^2 & 0 & c_{\Xi_2\Xi_2}(t_2-t_4) \\ c_{\Xi_1\Xi_1}(t_1-t_3) & 0 & \sigma_1^2 & 0 \\ 0 & c_{\Xi_2\Xi_2}(t_2-t_4) & 0 & \sigma_2^2 \end{pmatrix}. \qquad \text{(A.3)}$$

In (A.3) the independence of Ξ_1 and Ξ_2 has been utilised as well as the property that the auto-covariance is an even function, i.e., $c_{\Xi\Xi}(t) = c_{\Xi\Xi}(-t)$. One way of calculating the expectations in (A.1) and (A.2) is through application of the characteristic function $\varphi(s)$ of Ξ. In fact, the terms can be expressed as

$$\varphi_{\Xi}(\underline{s}_0) = \mathrm{E}\, e^{j\underline{s}'\Xi}\big|_{\underline{s}=\underline{s}_0} = e^{-\frac{\underline{s}_0'\mathbf{K}\underline{s}_0}{2}}. \qquad \text{(A.4)}$$

For the mean in (A.1), the upper left 2×2 matrix of $\mathbf{K}$ and $\underline{s}_0 = [1,-1]'$ must be used; for the mean in (A.2), $\underline{s}_0 = [1,-1,-1,1]'$ and the entire $\mathbf{K}$ must be used. Inserting these values into (A.4) and replacing the time instances by

$$t_1 = t-t'-\tau, \qquad t_2 = t-t', \qquad t_3 = t-\bar{t}-\tau, \qquad t_4 = t-\bar{t},$$

yields

$$\mathbb{E}\,P(t) = e^{-\frac{\sigma_1^2+\sigma_2^2}{2}}\; e^{-j\omega_1\tau}\frac{1}{T}\int\limits_{-T/2}^{T/2} e^{j\pi\frac{B}{T}\left((t-t'-t_n-\tau)^2-t'^2\right)}\,dt', \tag{A.5}$$

and hence

$$|\mathbb{E}\,P(t)| = e^{-\frac{\sigma_1^2+\sigma_2^2}{2}}\;\operatorname{sinc}(\pi B(t-t_n-\tau)). \tag{A.6}$$

For the second moment function we get

$$\mathbb{E}\,|P(t)|^2 = e^{-(\sigma_1^2+\sigma_2^2)}\frac{1}{T^2}\int\limits_{-T/2}^{T/2}\int\limits_{-T/2}^{T/2} e^{j\pi\frac{B}{T}(t-t_n-\tau)(t'-\bar{t})}e^{c_{\Xi_1\Xi_1}(t'-\bar{t})+c_{\Xi_2\Xi_2}(t'-\bar{t})}\,dt'd\bar{t}. \tag{A.7}$$

Under the assumption of identical oscillators $c_{\Xi_1\Xi_1}(t) = c_{\Xi_2\Xi_2}(t) \equiv c_{\Xi\Xi}(t)$, (A.7) can be rewritten as

$$\begin{aligned}\mathbb{E}\,|P(t)|^2 \;&=\; e^{-2\sigma^2}\frac{1}{T^2}\int\limits_{-T/2}^{T/2}\int\limits_{-T/2}^{T/2} e^{j\pi\frac{B}{T}(t-t_n-\tau)(t'-\bar{t})}\left(e^{2c_{\Xi\Xi}(t'-\bar{t})}-1\right)\,dt'd\bar{t}\\ &\quad + e^{-2\sigma^2}\frac{1}{T^2}\int\limits_{-T/2}^{T/2}\int\limits_{-T/2}^{T/2} e^{j\pi\frac{B}{T}(t-t_n-\tau)(t'-\bar{t})}\,dt'd\bar{t}.\end{aligned} \tag{A.8}$$

Providing statistically white phase noise, i.e., $c_{\Xi\Xi}(t) = \sigma^2\delta(t)$, where $\delta(t)$ denotes the Dirac delta function , the first integrand on the right hand side of (A.8) becomes the line integral

$$\frac{e^{-2\sigma^2}}{T^2}\int\limits_{-T/2}^{T/2}\left(e^{2\sigma^2}-1\right)\sqrt{2}\,dt \tag{A.9}$$

so that

$$\mathbb{E}\,|P(t)|^2 = \frac{\sqrt{2}}{T}e^{-2\sigma^2}\left(e^{2\sigma^2}-1\right) + e^{-2\sigma^2}\operatorname{sinc}^2(\pi B(t-t_n-\tau)), \tag{A.10}$$

and hence, with (A.5),

$$\sigma_p^2(t) = \mathbb{E}\,|P(t)|^2 - |\mathbb{E}\,P(t)|^2 = \frac{\sqrt{2}}{T}\left(1-e^{-2\sigma^2}\right). \tag{A.11}$$

Annex B
Standard deviation of phase noise for a finite observation time

Let $\Xi(t)$ denote a wide sense stationary stochastic and ergodic phase noise process with variance

$$\sigma_\Xi^2 = \mathbb{E}\ \left(\Xi(t) - \mathbb{E}\,\Xi(t)\right)^2 = \mathbb{E}\,\Xi(t)^2 - \left(\mathbb{E}\,\Xi(t)\right)^2, \tag{B.1}$$

which describes the variation of the phase around its mean of zero for an infinite observation time. We are now interested in the variation of this phase process (variance) for finite observation times T. For a given realisation $\xi(t)$ of the stochastic process measured over time $T' \gg T$, we can estimate this variance as the average of the differences $\langle(\xi_T(t) - \bar{\xi}_T(t))^2\rangle$ within the observation interval T. Sliding the observation window along the time axis we can see how this (time-limited) variance estimate varies over time, see Fig. B.1.

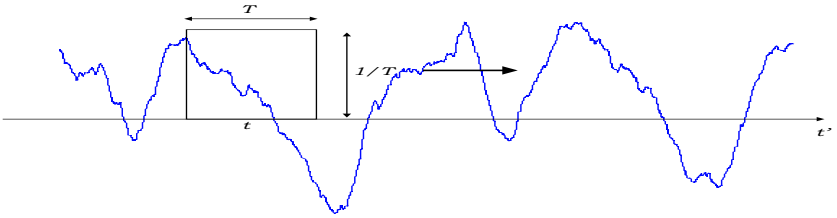

Figure B.1 : *Realisation of phase noise with sliding window to estimate the rms for finite observation time T.*

Mathematically, this can be expressed as the convolution of the phase $\xi(t)$ and the ideal low-pass filter $h(t) = 1/T\,\mathrm{rect}(t/T)$, i.e.,

$$\sigma_\xi^2(t,T) = \frac{1}{T}\xi(t)^2 * \mathrm{rect}\left(\frac{t}{T}\right) - \frac{1}{T^2}\left(\xi(t) * \mathrm{rect}\left(\frac{t}{T}\right)\right)^2, \tag{B.2}$$

where $*$ represents the convolution operator. The mean value of this variance function over the entire measurement time T' is

$$\sigma_\xi^2(T) = \frac{1}{T'}\int_{-T'/2}^{T'/2} \sigma_\xi^2(t,T)\,dt, \tag{B.3}$$

which may be used as a measure of the rms phase noise for limited observation time. Applying the Fourier-transform to (B.2) and inserting the result into (B.3),

including the inverse Fourier-transform, yields

$$\sigma_\xi^2(T) = \frac{1}{T'} \int_{-T'/2}^{T'/2} \int_{-\infty}^{\infty} \left(\Xi(\omega) * \Xi(\omega)\right) \operatorname{sinc}(\omega T/2) \exp(j\omega t)\, d\omega\, dt \tag{B.4}$$
$$-\frac{1}{T'} \int_{-T'/2}^{T'/2} \int_{-\infty}^{\infty} \left(\Xi(\omega) \operatorname{sinc}(\omega T/2)\right) * \left(\Xi(\omega) \operatorname{sinc}(\omega T/2)\right) \exp(j\omega t)\, d\omega\, dt,$$

where $\Xi(\omega)$ denotes the Fourier-transform of $\xi(t)$ (not to be confused with the stochastic process) and $T \operatorname{sinc}(\omega T/2)$ is the corresponding Fourier-transform of the rectangular window. Switching the integration order and using the Dirac-function approximation gives

$$\frac{1}{T'} \int_{-T'/2}^{T'/2} \exp(j\omega t)\, dt = \operatorname{sinc}(\omega T'/2) \cong \delta(\omega) \quad \text{for} \quad T' \gg 1 \tag{B.5}$$

and writing out the convolution integral leads to

$$\sigma_\xi^2(T) = \int_{-\infty}^{\infty} \int_{-\infty}^{\infty} \Xi(\omega - \nu)\Xi(\nu)\, d\nu \operatorname{sinc}(\omega T/2)\, \delta(\omega)\, d\omega \tag{B.6}$$
$$-\int_{-\infty}^{\infty} \int_{-\infty}^{\infty} \Xi(\omega - \nu) \operatorname{sinc}\left((\omega - \nu)T/2\right) \Xi(\nu) \operatorname{sinc}(\nu T/2)\; d\nu\, \delta(\omega)\, d\omega.$$

Exploiting the 'sifting property' of the Dirac-function and the fact that $\Xi(\omega) = \Xi(-\omega)^*$, we can write

$$\sigma_\xi^2(T) = \int_{-\infty}^{\infty} |\Xi(\omega)|^2 \left(1 - \operatorname{sinc}(\omega T/2)^2\right)\, d\omega. \tag{B.7}$$

In order to investigate the statistical properties of the estimator (B.7), e.g., the expectation value, we cannot simply replace the realisation $\xi(t)$ with the corresponding random process because the Fourier-transform of a stationary stochastic process (which has infinite energy) does not exist. However, substituting the finite Fourier transform in (B.4) by the discrete Fourier transform

$$\xi_n = \frac{1}{N} \sum_{k=0}^{N-1} \Xi_k \exp(j2\pi nk/N) \tag{B.8}$$

and following the time-continuous derivation above, leads to

$$\sigma_\xi^2(K) = \frac{1}{N}\sum_{k=0}^{N-1} |\Xi_k|^2 \left(1 - \operatorname{sinc}^2(\pi k K)\right) = \sum_{k=0}^{N-1} I_{\Xi\Xi}^N(k) \left(1 - \operatorname{sinc}^2(\pi k K)\right), \tag{B.9}$$

where $I_{\Xi\Xi}^N(k)$ denotes the periodogram of length N. It is well known that the expectation of the periodogram for sufficiently large N is identical to the power density spectrum of Ξ, i.e., $\mathbb{E}\, I_{\Xi\Xi}^N(k) = C_{\Xi\Xi}(k)$ [30]. Finally, in time continuous notation, the variance can be computed as

$$\sigma_\Xi^2 = \int_{-\infty}^{\infty} C_{\Xi\Xi}(\omega) \left(1 - \operatorname{sinc}^2(\omega T/2)\right) d\omega \cong 2 \int_{\frac{0.443}{T}}^{\infty} C_{\Xi\Xi}(\omega)\, d\omega, \tag{B.10}$$

where the sinc-function has been approximated by a rectangular window with a 3dB-width of $0.443/T$.

Alternatively, the same result can be calculated as the expectation of

$$\sigma^2 = \mathbb{E}\left\{ \frac{1}{T}\int_{-\infty}^{\infty} \left| \Xi(t) - \frac{1}{T}\int_{-\infty}^{\infty} \Xi(s)\, ds \right|^2 dt \right\}, \tag{B.11}$$

where both integrals of stochastic processes are defined as ‘mean square’ integrals.

Annex C
Least squares estimation of phase noise polynomial coefficients

In contrast to (33), let Ξ be a discrete stochastic Gaussian process, i.e., $\Xi_n \equiv \Xi(n\Delta t)$ for $n = 1, \ldots, N$, where ΔT represents the sampling period, e.g., the PRI, and $N\Delta t = T_s$ is the coherent processing time (i.e., synthetic aperture time). Writing this discrete stochastic time series as a random vector $\underline{\Xi} = [\Xi_1, \ldots, \Xi_N]'$, (40) can be expressed in vector notation as

$$\underline{\Xi} = \mathbf{A}\underline{b} + \underline{\Upsilon}, \tag{C.1}$$

where

$$\mathbf{A} = \begin{bmatrix} 1 & \Delta t & \Delta t^2 & \Delta t^3 \\ 1 & 2\Delta t & 4\Delta t^2 & 8\Delta t^3 \\ \vdots & \vdots & \vdots & \vdots \\ 1 & N\Delta t & N^2\Delta t^2 & N^3\Delta t^3 \end{bmatrix} \quad \text{and} \quad \underline{\Upsilon} = \begin{bmatrix} \Upsilon_1 \\ \vdots \\ \Upsilon_N \end{bmatrix} = \begin{bmatrix} \Upsilon(\Delta t) \\ \vdots \\ \Upsilon(N\Delta t) \end{bmatrix}. \tag{C.2}$$

An estimate of the parameter vector $\underline{b} = [b_0, \ldots, b_3]'$ can be found as solution of the Least Square (LS) minimisation problem $\min_{\underline{b}} |\underline{\Xi} - \mathbf{A}\underline{b}|^2$ [29]:

$$\hat{\underline{b}} = (\mathbf{A}'\mathbf{A})^{-1}\mathbf{A}'\underline{\Xi}. \tag{C.3}$$

Since $\underline{\Xi}$ is normal-distributed, vector $\hat{\underline{b}}$, is as a linear transformation of $\underline{\Xi}$, also normal-distributed with expectation zero and covariance matrix

$$\mathbf{K}_{\hat{\underline{b}}} = \mathrm{E}\,\hat{\underline{b}}\hat{\underline{b}}' = (\mathbf{A}'\mathbf{A})^{-1}\mathbf{A}'\mathrm{E}\,\underline{\Xi}\underline{\Xi}'\mathbf{A}\,(\mathbf{A}'\mathbf{A})^{-1} = \mathbf{P}^{\#}_{\mathbf{A}}\mathbf{K}_{\underline{\Xi}}\mathbf{P}^{\#'}_{\mathbf{A}}, \tag{C.4}$$

where $\mathbf{P}^{\#}_{\mathbf{A}} = (\mathbf{A}'\mathbf{A})^{-1}\mathbf{A}'$ and the covariance matrix of $\underline{\Xi}$ is

$$\begin{aligned} \mathbf{K}_{\underline{\Xi}} &= \mathrm{E}\,\underline{\Xi}\underline{\Xi}' = \mathrm{E}\begin{bmatrix} \Xi_1 \\ \vdots \\ \Xi_N \end{bmatrix}[\Xi_1 \cdots \Xi_N] \\ &= \begin{bmatrix} \sigma^2_{\underline{\Xi}} & c_{\underline{\Xi}\underline{\Xi}}(1) & c_{\underline{\Xi}\underline{\Xi}}(2) & \cdots & c_{\underline{\Xi}\underline{\Xi}}(N) \\ c_{\underline{\Xi}\underline{\Xi}}(1) & \sigma^2_{\underline{\Xi}} & c_{\underline{\Xi}\underline{\Xi}}(1) & \cdots & c_{\underline{\Xi}\underline{\Xi}}(N-1) \\ c_{\underline{\Xi}\underline{\Xi}}(2) & c_{\underline{\Xi}\underline{\Xi}}(1) & \sigma^2_{\underline{\Xi}} & \cdots & c_{\underline{\Xi}\underline{\Xi}}(N-2) \\ \vdots & \vdots & \vdots & \ddots & \vdots \\ c_{\underline{\Xi}\underline{\Xi}}(N) & c_{\underline{\Xi}\underline{\Xi}}(N-1) & c_{\underline{\Xi}\underline{\Xi}}(N-2) & \cdots & \sigma^2_{\underline{\Xi}} \end{bmatrix}. \end{aligned} \tag{C.5}$$

The factor of two in front of the auto-covariance function (due to the sum of two independent oscillators, see (37) has been dropped for clarity reasons; however, it is included in (41).

It can be recognized that, for instance, the first column of $\mathbf{K}_{\underline{\Xi}}$ in (C.5) represents the causal part of the phase noise's auto-covariance function at discrete times $n\Delta t$, compare (33).

The i^{th} element of the parameter vector estimate $\hat{b}_i = \underline{u}_i'\hat{\underline{b}}$ is also normal-distributed with zero mean and variance

$$\sigma^2_{\hat{b}_i} = \underline{u}_i'\mathbf{K}_{\hat{\underline{b}}}\underline{u}_i = \underline{u}_i\mathbf{P}^{\#}_{\mathbf{A}}\mathbf{K}_{\underline{\Xi}}\mathbf{P}^{\#'}_{\mathbf{A}}\underline{u}_i, \tag{C.6}$$

where the three-dimensional unit vector $\underline{u}_i$ has all elements zero except for a one at position $i = 1, 2 \text{ or } 3$.

Subtracting the estimated polynomial from the original phase noise vector leads to

$$\underline{\Upsilon} = \underline{\Xi} - \mathbf{A}\hat{\underline{b}} = \underline{\Xi} - \mathbf{A}\left(\mathbf{A}'\mathbf{A}\right)^{-1}\mathbf{A}'\underline{\Xi} = \mathbf{P}^{\perp}_{\mathbf{A}}\underline{\Xi}, \tag{C.7}$$

where $\mathbf{P}^{\perp}_{\mathbf{A}} = \mathbf{I} - \mathbf{A}\left(\mathbf{A}'\mathbf{A}\right)^{-1}\mathbf{A}'$ represents the projector onto the complementary subspace spanned by the columns of $\mathbf{A}$. Again, $\underline{\Upsilon}$ is as a linear transformation of a Gauss-vector, normal distributed with zero mean and covariance matrix

$$\mathbf{K}_{\underline{\Upsilon}} = \mathbb{E}\,\underline{\Upsilon}\underline{\Upsilon}' = \mathbf{P}^{\perp}_{\mathbf{A}}\mathbb{E}\,\underline{\Xi}\underline{\Xi}'\mathbf{P}^{\perp}_{\mathbf{A}} = \mathbf{P}^{\perp}_{\mathbf{A}}\mathbf{K}_{\underline{\Xi}}\mathbf{P}^{\perp}_{\mathbf{A}}. \tag{C.8}$$

The variance of the remaining high-frequency phase noise components $\sigma^2_{\underline{\Upsilon}}$ is contained in the diagonal of (C.8), i.e., can either be calculated as $\sigma^2_{\underline{\Upsilon}} = 1/N\,\mathrm{tr}\{\mathbf{K}_{\underline{\Upsilon}}\}$ ($\mathrm{tr}\{\cdot\}$ denotes the trace operator) or as

$$\sigma^2_{\underline{\Upsilon}} = \underline{u}_n'\mathbf{K}_{\underline{\Upsilon}}\underline{u}_n = \underline{u}_n'\mathbf{P}^{\perp}_{\mathbf{A}}\mathbf{K}_{\underline{\Xi}}\mathbf{P}^{\perp}_{\mathbf{A}}\underline{u}_n = \underline{a}_n'\mathbf{K}_{\underline{\Xi}}\underline{a}_n, \tag{C.9}$$

where $\underline{a}_n = \mathbf{P}^{\perp}_{\mathbf{A}}\underline{u}_n$ represents the n^{th} column of $\mathbf{P}^{\perp}_{\mathbf{A}}$ for $n = 1, \ldots, N$.

It is interesting to have a closer look at (C.9). The covariance matrix $\mathbf{K}_{\underline{\Xi}}$ in (C.5) belongs to a important class of Toeplitz matrices, the so-called circulant matrices, where each column is a 'down-shifted' version of its predecessor [53]. As such, any circulant matrix vector product constitutes a convolution of the first column of the matrix with the vector, which in fact can be performed via three discrete Fourier transforms, e.g.,

$$\mathbf{K}_{\underline{\Xi}} \cdot \underline{a}_n = \tilde{c}_{\Xi\Xi}(k) \star \tilde{\underline{a}}_n(k) = \mathcal{F}^{-1}\Big\{\mathcal{F}\{\tilde{c}_{\Xi\Xi}(k)\} \cdot \mathcal{F}\{\tilde{\underline{a}}_n(k)\}\Big\}. \tag{C.10}$$

The 'tilded' quantities

$$\tilde{c}_{\Xi\Xi} = [c_{\Xi\Xi}(1:N),\, c_{\Xi\Xi}(N-1:-1:2)]' \quad \text{and} \quad \tilde{\underline{a}}_n = [\underline{a}_n,\, \underline{0}]' \tag{C.11}$$

in (C.10) represent the entire (evenly-extended) auto-covariance function and the zero-padded vector $\underline{a}$, respectively [53].

Going back to the continuous time notation, the variance in (C.9) may therefore be written as

$$\begin{aligned}\sigma^2_{\underline{\Upsilon}} &= \underline{\tilde{a}}_n(t) \cdot \Big(c_{\Xi\Xi}(t) \star \underline{\tilde{a}}_n(t)\Big) = \int_{-\infty}^{\infty} \underline{\tilde{a}}_n(t) \int_{-\infty}^{\infty} C_{\Xi\Xi}(f)\tilde{A}(f)e^{j2\pi ft}\, df dt \\ &= \int_{-\infty}^{\infty} C_{\Xi\Xi}(f)\tilde{A}(f) \underbrace{\int_{-\infty}^{\infty} \underline{\tilde{a}}_n(t)e^{j2\pi ft}dt}_{\tilde{A}(-f)=\tilde{A}(f)^*}\, df = \int_{-\infty}^{\infty} C_{\Xi\Xi}(f)|\tilde{A}(f)|^2\, df, \end{aligned} \tag{C.12}$$

where $\tilde{A}(f) = \mathcal{F}\{\tilde{a}(t)\}$.

Analogously, the variance of each polynomial coefficient in (C.6) can be expressed as a filtered version of the spectral density function. Let the elements of the random vector

$$\underline{v}_i = \mathbf{P}^{\#'}_{\mathbf{A}}\, \underline{u}_i = \mathbf{A}\left(\mathbf{A}'\mathbf{A}\right)^{-1} \underline{u}_i \qquad \in \mathbb{C}^{N\times 1}, \tag{C.13}$$

represent the discrete random series corresponding to the time-continuous stochastic process $v_i(t)$. Then

$$\sigma^2_{\hat{b}_i} = \int_{-\infty}^{\infty} C_{\Xi\Xi}(f)\ |V_i(f)|^2\, df, \tag{C.14}$$

where $V_i(f)$ is the Fourier-transform of $v_i(t)$.

Annex D
Coordinate system conventions

For the required analysis and simulation of an airborne bistatic SAR system it is sufficient to concentrate on three coordinate systems and the necessary transformations between them. The conventions are identical to the ones defined by Ender [54].

D.1 Scene coordinate system

The stationary Cartesian scene system, subscript ‘s’, describes the orientation of the underlying terrain and serves as a ‘master’ coordinate system.

$\underline{x}_s$ from west to east (left to right)

$\underline{y}_s$ cross-product between $\underline{x}_s$ and $\underline{z}_s$

$\underline{z}_s$ positive upwards

The origin is chosen at the centre of the scene.

D.2 Platform coordinate system

The Cartesian platform system, subscript ‘p’, describes the orientation of the airplane.

$\underline{x}_p$ longitudinal axis or roll-axis

$\underline{y}_p$ lateral axis, positive to the right

$\underline{z}_p$ cross-product between $\underline{x}_p$ and $\underline{y}_p$, positive downwards

The origin is chosen at the centre of mass of the platform.

D.3 Antenna coordinate system

The Cartesian antenna system, subscript ‘a’, describes the orientation of the antenna mounted and steered on the platform.

$\underline{x}_a$ azimuthal axis

$\underline{y}_a$ antenna normal, positive to the right

$\underline{z}_a$ elevation axis, cross-product between $\underline{x}_a$ and $\underline{y}_a$, positive downwards

The origin is chosen at the phase centre of the antenna plane.

Annex E
Angular transformation conventions

E.1 Euler rotation angles

The so-called Euler angles are defined as follows: Initially the new coordinate system is identical to the original one. The following sequence of operations occurs:

1. Rotation around the z-axis through the azimuth angle Ψ. Counter clockwise when viewed from the arrow tip, i.e., from above. The two systems are still aligned in the z-direction.

2. Rotation around the y-axis (of the new system) through the elevation angle Θ. Counter clockwise when viewed from the arrow tip, i.e., from the left.

3. Rotation around the x-axis (of the new system) through the roll angle Φ. clockwise when viewed from the arrow tip, i.e., from in front.

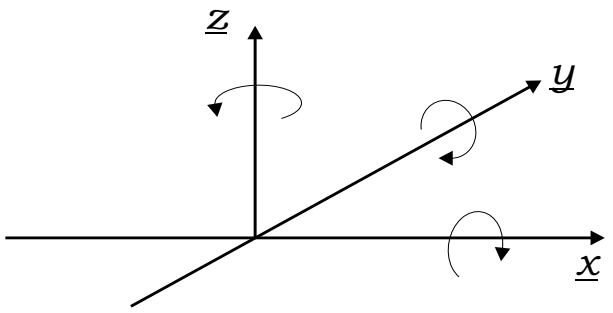

Figure E.1 : *Euler rotation angles.*

The sequence of rotations must be from one to three. The individual rotations can be described through matrices:

$$\begin{aligned}
\mathbf{L}_1(\Phi) &= \begin{pmatrix} 1 & 0 & 0 \\ 0 & \cos\Phi & \sin\Phi \\ 0 & -\sin\Phi & \cos\Phi \end{pmatrix} \\
\mathbf{L}_2(\Theta) &= \begin{pmatrix} \cos\Theta & 0 & -\sin\Theta \\ 0 & 1 & 0 \\ \sin\Phi & 0 & \cos\Theta \end{pmatrix} \\
\mathbf{L}_3(\Psi) &= \begin{pmatrix} \cos\Psi & \sin\Psi & 0 \\ -\sin\Psi & \cos\Psi & 0 \\ 0 & 0 & 1 \end{pmatrix}, \qquad \text{(E.1)}
\end{aligned}$$

and the composite transformation matrix is yielded by

$$\mathbf{L}(\Phi,\Theta,\Psi) = \mathbf{L}_1(\Phi)\mathbf{L}_2(\Theta)\mathbf{L}_3(\Psi) = \tag{E.2}$$
$$\begin{pmatrix} \cos\Theta\cos\Psi & \cos\Theta\sin\Psi & -\sin\Theta \\ \sin\Phi\sin\Theta\cos\Psi - \cos\Phi\sin\Psi & \sin\Phi\sin\Theta\sin\Psi + \cos\phi\cos\Psi & \sin\Phi\cos\Theta \\ \cos\Phi\sin\Theta\cos\Psi + \sin\Phi\sin\Theta & \cos\Phi\sin\Theta\sin\Psi - \sin\Phi\cos\Psi & \cos\Phi\cos\Theta \end{pmatrix}.$$

E.2 Angular transformation

The new coordinate system 'N' originates from the old one 'O' by rotation around $\Phi_{\mathrm{NO}}, \Theta_{\mathrm{NO}}, \Psi_{\mathrm{NO}}$ via

$$\mathbf{L}_{\mathrm{NO}} \equiv \mathbf{L}(\Phi_{\mathrm{NO}}, \Theta_{\mathrm{NO}}, \Psi_{\mathrm{NO}}) = \mathbf{L}_1(\Phi_{\mathrm{NO}})\mathbf{L}_2(\Theta_{\mathrm{NO}})\mathbf{L}_3(\Psi_{\mathrm{NO}}). \tag{E.3}$$

An arbitrary vector $\underline{a}_{\mathrm{O}}$ in the O-system can be transformed into the N-system by

$$\underline{a}_{\mathrm{N}} = \mathbf{L}_{\mathrm{NO}}\,\underline{a}_{\mathrm{O}}. \tag{E.4}$$

The inverse of $\mathbf{L}_{\mathrm{NO}}$ is identical to the transpose matrix, i.e., $\mathbf{L}_{\mathrm{NO}}^{-1} = \mathbf{L}'_{\mathrm{NO}}$. Let 'F' be a further coordinate system. It yields

$$\mathbf{L}_{\mathrm{FO}} = \mathbf{L}_{\mathrm{FN}}\mathbf{L}_{\mathrm{NO}}. \tag{E.5}$$

E.3 Scene into platform coordinate system

The angles Φ_{ps}, Θ_{ps}, Ψ_{ps} describe the orientation of the platform within the scene coordinate system, see Fig. E.2. For a normal flight attitude, the angle Θ_{ps} is chosen as zero and $\Phi_{\mathrm{ps}} = 180°$. Hence, the transformation matrix reduces to

$$\mathbf{L}_{\mathrm{ps}} \equiv \mathbf{L}(\pi, 0, \Psi_{\mathrm{ps}}) = \begin{pmatrix} \cos\Psi_{\mathrm{ps}} & \sin\Psi_{\mathrm{ps}} & 0 \\ \sin\Psi_{\mathrm{ps}} & -\cos\Psi_{\mathrm{ps}} & 0 \\ 0 & 0 & -1 \end{pmatrix}, \tag{E.6}$$

where Ψ_{ps} denotes the course angle. Positive Ψ_{ps} means course to the right of x_s.

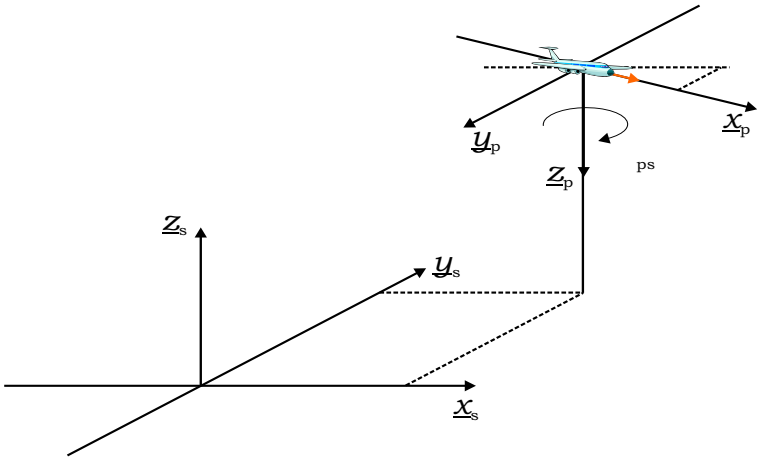

Figure E.2 : *Angular relation between scene and platform coordinate systems.*

E.4 Platform into antenna coordinate system

The angles Φ_{ap}, Θ_{ap}, Ψ_{ap} describe the orientation of the antenna within the platform coordinate system. The angle Θ_{ap} is always set to zero. Positive azimuth angle Ψ_{ap} rotates the antenna to the right backwards and positive depression angle Φ_{ap} inclines the antenna downwards, i.e., first rotating then tilting. The transformation matrix then yields:

$$\begin{aligned} \mathbf{L}_{ap} &\equiv \mathbf{L}(\Phi_{ap}, 0, \Psi_{ap}) = \\ &= \begin{pmatrix} \cos\Psi_{ap} & \sin\Psi_{ap} & 0 \\ -\cos\Phi_{ap}\sin\Psi_{ap} & \cos\Phi_{ap}\cos\Psi_{ap} & \sin\Phi_{ap} \\ \sin\Phi_{ap}\sin\Psi_{ap} & -\sin\Phi_{ap}\cos\Psi_{ap} & \cos\Phi_{ap} \end{pmatrix}, \end{aligned} \tag{E.7}$$

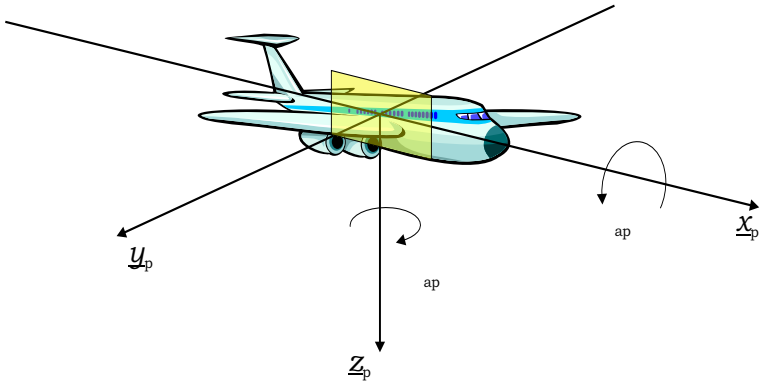

Figure E.3 : *Angular relation between platform and antenna coordinate systems.*

Consequently, the transformation between the scene and the antenna coordinate systems is given as the product

$$\mathbf{L}_{\mathrm{as}} \equiv \mathbf{L}_{\mathrm{ap}}(\Phi_{\mathrm{ap}}, \Psi_{\mathrm{ap}}) \cdot \mathbf{L}_{\mathrm{ps}}(\Psi_{\mathrm{ps}}). \tag{E.8}$$

Annex F
State vector of platforms at time origin

To determine the location of both platforms over the ground at time $t = 0$, it is often convenient to define a squint angle $\Psi_{0,i}$ and a corresponding elevation angle $\Phi_{0,i}$ for either radar antenna $i = 1, 2$ to the centre of the scene. The antenna normal vector for these pointing angles is determined by the quiescent pointing vector $\underline{y}_a = \underline{y}_p = -\underline{y}_s = -[0, 1, 0]^T$ via the transformation matrix from antenna into scene coordinates

$$\underline{u}_{\underline{R}_{0,i}} = \mathbf{L}'_{\text{as}}\underline{y}_a = (\mathbf{L}_{ap}(\Phi_{0,i}, \Psi_{0,i})\mathbf{L}_{ps}(0))' \underline{y}_a. \tag{F.1}$$

This vector expresses the unit vector from the scene center to the platform at the time origin. The length of the state vector can now be determined as the intersection point of $\underline{u}_{\underline{R}_{0,i}}$ with the x, y-plane elevated to a given altitude H_i:

$$\underline{R}_{0,i} = H_i \frac{\underline{z}'_s \underline{z}_s}{\underline{z}'_s \underline{u}_{\underline{R}_{0,i}}} \underline{u}_{\underline{R}_{0,i}} = \frac{H_i}{\underline{z}'_s \underline{u}_{\underline{R}_{0,i}}} \underline{u}_{\underline{R}_{0,i}}. \tag{F.2}$$

In order to illuminate the centre of the scene at $t = 0$ with exactly the peak of the antenna mainbeam, the antenna needs to be steered (squinted and tilted) by the directional cosine and sine:

$$\begin{aligned} u_{0,i} &= \underline{x}'_s \frac{\underline{R}_{0,i}}{\|\underline{R}_{0,i}\|} \\ v_{0,i} &= \underline{z}'_s \frac{\underline{R}_{0,i}}{\|\underline{R}_{0,i}\|}, \end{aligned} \tag{F.3}$$

compare (53).

Annex G
Bistatic SAR processing algorithm

Algorithm 1 Time Domain Processing (courtesy N. Çotuk)

for $l = 1$ to L **do**
{Loop over each satellite position}
  for $n = 1$ to N **do**
{Loop over image cell in x-direction}
    for $m = 1$ to M **do**
{Loop over image cell in y-direction}
      $R_{sc} = \sqrt{((x_s - x_c)^2 + (y_s - y_c)^2 + (z_s - z_c)^2}$
{Calculate satellite to cell range}
      $R_{ca} = \sqrt{((x_c - x_a)^2 + (y_c - y_a)^2 + (z_c - z_a)^2}$
{Calculate cell to antenna range}
      $R_b = R_{sc} + R_{ca}$
{Calculate bistatic range for this cell and satellite location}
      $R_{sa} = \sqrt{((x_s - x_a)^2 + (y_s - y_a)^2 + (z_s - z_a)^2}$
{Calculate direct range from antenna to satellite location}
      $R_{\text{diff}} = R_b - R_{sa}$
{Calculate range difference}
      $\theta = \exp\left(\frac{j2\pi}{\lambda} R_{\text{diff}}\right)$
{Complex phase of the expected return echo}
      $\text{index}_n = \text{round}\left[\frac{R_{\text{diff}}}{\Delta r}\right]$
{Complex phase of the expected return echo}
      $\text{index}_n = \text{round}\left[\frac{R_{\text{diff}}}{\Delta r}\right]$
{index to locate the range cell in range profile (Δr = range between each sample in range profile)}
      $E_{nm}^{\text{temp}} = \text{data}(l, \text{index}_n) \cdot \text{conj}(\theta)$
{Generate a set of n x m pixels for each satellite position by multiplying complex conjugate of calculated phase with the measured data}
    end for
{end m loop}
  end for
{end n loop}
  $E_{nm} = E_{nm} + E_{nm}^{\text{temp}}$
{Coherent summation of images}
end for
{end l loop}

DOCUMENT CONTROL DATA

(Security classification of title, body of abstract and indexing annotation must be entered when document is classified)

1. ORIGINATOR (the name and address of the organization preparing the document. Organizations for whom the document was prepared, e.g. Centre sponsoring a contractor's report, or tasking agency, are entered in section 8.)

Defence R&D Canada – Ottawa
Ottawa, ON, Canada K1A 0K2

2. SECURITY CLASSIFICATION (overall security classification of the document including special warning terms if applicable).

UNCLASSIFIED

3. TITLE (the complete document title as indicated on the title page. Its classification should be indicated by the appropriate abbreviation (S,C,R or U) in parentheses after the title).

Bistatic Synthetic Aperture Radar

4. AUTHORS (Last name, first name, middle initial. If military, show rank, e.g. Doe, Maj. John E.)

Gierull, Christoph H.

5. DATE OF PUBLICATION (month and year of publication of document)	6a. NO. OF PAGES (total containing information. Include Annexes, Appendices, etc).	6b. NO. OF REFS (total cited in document)
November 2004	107	54

7. DESCRIPTIVE NOTES (the category of the document, e.g. technical report, technical note or memorandum. If appropriate, enter the type of report, e.g. interim, progress, summary, annual or final. Give the inclusive dates when a specific reporting period is covered).

Technical Report

8. SPONSORING ACTIVITY (the name of the department project office or laboratory sponsoring the research and development. Include address).

Defence R&D Canada – Ottawa
Ottawa, ON, Canada K1A 0K2

9a. PROJECT OR GRANT NO. (if appropriate, the applicable research and development project or grant number under which the document was written. Specify whether project or grant).	9b. CONTRACT NO. (if appropriate, the applicable number under which the document was written).
13dt03	

10a. ORIGINATOR'S DOCUMENT NUMBER (the official document number by which the document is identified by the originating activity. This number must be unique.)	10b. OTHER DOCUMENT NOs. (Any other numbers which may be assigned this document either by the originator or by the sponsor.)
DRDC Ottawa TR 2004-190	

11. DOCUMENT AVAILABILITY (any limitations on further dissemination of the document, other than those imposed by security classification)

(X) Unlimited distribution
( ) Defence departments and defence contractors; further distribution only as approved
( ) Defence departments and Canadian defence contractors; further distribution only as approved
( ) Government departments and agencies; further distribution only as approved
( ) Defence departments; further distribution only as approved
( ) Other (please specify):

12. DOCUMENT ANNOUNCEMENT (any limitation to the bibliographic announcement of this document. This will normally correspond to the Document Availability (11). However, where further distribution beyond the audience specified in (11) is possible, a wider announcement audience may be selected).

13. ABSTRACT (a brief and factual summary of the document. It may also appear elsewhere in the body of the document itself. It is highly desirable that the abstract of classified documents be unclassified. Each paragraph of the abstract shall begin with an indication of the security classification of the information in the paragraph (unless the document itself is unclassified) represented as (S), (C), (R), or (U). It is not necessary to include here abstracts in both official languages unless the text is bilingual).

This technical report presents theoretical and experimental results of phase I of the Technology Investment Fund (TIF) project on low probability of intercept, that is bistatic SAR. In bistatic SAR, the transmitter and receiver are spatially separated and hence, the risks of detection and localization are significantly reduced, i.e., its vulnerability to jamming is reduced and its survivability significantly increased. Bistatic SAR images include information that is complementary to monostatic images due to the different scattering mechanisms involved. Such information could lead to the development of new techniques for automatic target recognition and classification.

The project investigates the feasibility of bistatic SAR and identifies performance limits through a trade-off analysis between radar parameters/geometry and achievable resolution. As the main result, conclusions are drawn regarding the bistatic observation time and the subsequent imaging performance under different bistatic configurations, as well as the performance degradation due to severe oscillator phase noise or jitter. The report also includes a description of a bistatic SAR simulator, an implemented version of a time domain bistatic SAR processor, and the analysis of existing experimental bistatic clutter data sets.

14. KEYWORDS, DESCRIPTORS or IDENTIFIERS (technically meaningful terms or short phrases that characterize a document and could be helpful in cataloguing the document. They should be selected so that no security classification is required. Identifiers, such as equipment model designation, trade name, military project code name, geographic location may also be included. If possible keywords should be selected from a published thesaurus. e.g. Thesaurus of Engineering and Scientific Terms (TEST) and that thesaurus-identified. If it not possible to select indexing terms which are Unclassified, the classification of each should be indicated as with the title).

Synthetic Aperture Radar (SAR)
Bistatic SAR
Performance Analysis

Defence R&D Canada

Canada's leader in Defence
and National Security
Science and Technology

R & D pour la défense Canada

Chef de file au Canada en matière
de science et de technologie pour
la défense et la sécurité nationale

www.drdc-rddc.gc.ca